HOKKAIDO UNIVERSITY

Title	Studies of photoinduced electron transfer and exciton dynamics in halide perovskite films and single particles
Author(s)	Bhagyashree Mahesha, Sachith
Degree Grantor	北海道大学
Degree Name	博士(環境科学)
Dissertation Number	甲第15137号
Issue Date	2022-09-26
DOI	https://doi.org/10.14943/doctoral.k15137
Doc URL	https://hdl.handle.net/2115/90557
Type	doctoral thesis
File Information	Bhagyashree_Mahesha_Sachith.pdf

Hokkaido University Collection of Scholarly and Academic Papers : HUSCAP

Doctoral Thesis

Studies of photoinduced electron transfer and exciton dynamics in halide perovskite films and single particles

(ハロゲン化物ペロブスカイト膜と単一粒子における光誘起電子移動と励起子ダイナミクスの研究)

Division of Environmental Materials Science

Graduate School of Environmental Science

Hokkaido University

Bhagyashree Mahesha Sachith

September 2022

Acknowledgment

I express my sincere gratitude to my supervisor Prof. Vasudevan Pillai Biju, for his constant encouragement, constructive criticism, meticulous supervision, and generous guidance, which helped me out of several constraints, complete the work embodied in this thesis, and inspired me to prepare this thesis. Also, I take this opportunity to acknowledge the constant support from Dr. Takuya Okamoto, Dr. Yuta Takano, Dr. Sushant Ghimire, and Dr. Palyam Subramanyam. I acknowledge the kind administrative support of Ms. Atsuko Fujii. Also, I express my sincere gratitude to my lab mates for their constant support and friendship.

I extend my sincere thanks to Prof. Naoto Tamai, Kwansei Gakuin University, and Prof. Hiroshi Imahori, Kyoto University, for their help with transient absorption measurements, and Prof. Hiroshi Miyasaka and Dr. Syoji Ito, Osaka University, for antibunching measurements, and Prof. Hiroaki Misawa and Dr. Shi Xu, Hokkaido University for FDTD simulations. I acknowledge the Hokkaido University Nanotechnology PLATFORM for the STEM, SEM, and FIB facilities. I am grateful to Prof. Mallu, P., Dr. Sandeep, S., Dr. Karthik, C. S., and Dr. Madhukar, B. S., J.S.S. Science, and Technology University for their support and encouragement during my stay in Japan.

Indeed, the words fail to express my feeling towards my parents Bhagyashree and Mahesha, M., and my family members, including Dr. Sharath, B. M., Dr. Ashwini, K. R., and Anusha, H. S., without their constant encouragement and support, my dream to complete this thesis would not have come true.

I am greatly thankful to my friends, mainly Hema, Dileep, Dr. Deepak, Pardhu, Dr. Jeladhara, Dr. Lata, Dr. Shahjahan, Dr. Bhagyalakshmi, Yoshida, Zhao, and Dong, for their support and encouragement during my studies at Hokkaido University. Thanks to everyone who directly or indirectly helped me during my stay at Hokkaido University.

Sachith B M

Abstract

Lead halide perovskites have become the most promising semiconductor materials for light-harvesting and light-emitting applications. These materials in the nanocrystalline forms, obtained by reliable colloidal synthesis approaches, show high photoluminescence quantum yield, high charge carrier mobilities, long photoluminescence lifetimes, and high photostability. However, their exciton, charge carrier properties, and interfacial electron transfer dynamics need optimization for next-generation perovskite devices. This thesis mainly focuses on the electron donor-acceptor systems involving perovskite nanocrystal films or single-particles, including the exciton, charge carrier, and electron-transfer dynamics. It is summarized in five chapters. In **chapter 1**, I discuss the general properties and significance of lead halide perovskites. First, I introduce their structure, chemical compositions, and stability factors. Subsequently, I explain various perovskite nanocrystal synthesis methods to control the shape and dimensionality. The preparation methods for self-assembled perovskite nanocrystal thin films and different characterization techniques are discussed in the second section of this chapter. In the third section, I present the bandgap and fundamental optical properties of perovskite nanomaterials as functions of their halogen compositions, size, and shape. Also, I describe the charge carrier properties and quantum confinement in perovskite nanocrystals and films. In the final section, I explain the applications of halide perovskites to solar cells, photodetectors, and light-emitting diodes, summarizing my research motivation and objectives. In **chapter 2**, I provided complete details about the materials, synthesis methods, samples, and instrumentation techniques in this thesis. Perovskite nanocrystals are synthesized using hot injection, ligand-assisted reprecipitation, and a modified spray technique. Next, I explain the theoretical bases, working principles, and instrumental setups of various spectroscopic (UV-vis absorption, steady-state and time-resolved fluorescence spectroscopy, and transient absorption spectroscopy) and microscopic (single-particle fluorescence microscopy, transmission electron microscopy, and scanning electron microscopy) techniques. In **chapter 3**, I summarize the extent of carrier diffusion, the degree of radiative loss, and the rate of diffusion-controlled interfacial electron transfer in heterojunction films of cesium or formamidinium lead bromide nanocrystals and C_{60} or TiO_2. Electron transfer and charge separation were confirmed by measuring the photoluminescence decays, intensities, and transient absorption spectra. By measuring the distance-dependent photoluminescence lifetimes and photocounts in samples containing halide perovskite-C_{60} or halide perovskite-

TiO_2 donor-acceptor junctions, I find long-range (>100 μm) carrier diffusion and distance-dependent (>800 μm) interfacial electron transfer. In **chapter 4**, I demonstrate the electron transfer dynamics at the single-particle level by analyzing the photoluminescence blinking of single perovskite nanocrystals with or without tetracyanoquinodimethane or tetracyanobenzene. The Gibbs free energy changes of electron transfer are estimated to be negative, using the donors and acceptors' redox potentials and the HOMO-LUMO gaps/bandgaps. The electron transfer rates are determined from time-resolved photoluminescence measurements. Further, the statistical analysis of >450 single perovskite nanocrystals and the ON-time and OFF-time probability distributions help understand the photoluminescence blinking to the electron transfer relationship. In **chapter 5**, I investigated exciton-plasmon interactions for perovskite nanocrystals on Au plasmonic nanogaps. I find a huge photoluminescence intensity enhancement for perovskite single nanoparticles directly synthesized in Au nanogaps. Here, the Au nanogaps are created by the controlled Au sputter-coating on glass substrates, followed by the spray-synthesis of perovskite nanocrystals on the Au-coated substrates. The radiative exciton recombination rate of perovskite nanocrystals in the Au substrate is dramatically increased by coupling with the localized surface plasmon, obvious from a drastic decrease in the photoluminescence lifetime and an increase in the photocounts. The increased radiative recombination rate is attributed to the chemical and electromagnetic coupling of the Au plasmon with perovskite nanocrystals. Finally, I summarize the thesis and provide the prospect of the work embodied in this thesis.

Abbreviations and symbols

AVC	Antisolvent vapor-assisted crystallization
k_3	Auger recombination rate constant
τ_{av}	Average photoluminescence lifetime
C_{60}	Buckminster fullerene
k_2	Bimolecular recombination rate constant
CBM	Conduction band minimum
CsBr	Caesium bromide
ca	Centered around
°C	Degree Celsius
DMF	*N, N*-dimethylformamide
EMCCD	Electron multiplying charge-coupled device
ETL	Electron transport layer
FA	Formamidinium
FABr	Formamidinium bromide
fs	Femtosecond
FWHM	Full width at half maximum
g	Gram
GPa	Gigapascal
h	Hour
d_{hkl}	Interplanar spacing
ITC	Inverse temperature crystallization
LUMO	Lowest unoccupied molecular orbital
LED	Light emitting diode

LARP	Ligand-assisted reprecipitation
k_1	Monomolecular recombination rate constant
MA	Methylammonium
MHz	Megahertz
min	Minute
μM	Micromolar
μm	Micrometer
mL	Milliliter
mmol	Millimole
NA	Numerical aperture
NIR	Near infrared
nm	Nanometer
ns	Nanosecond
OPA	Optical parametric amplifier
PET	Photoinduced electron transfer
PL	Photoluminescence
PLQY	Photoluminescence quantum yield
PCBM-C_{61}	[6,6]-phenyl C_{61} butyric acid methyl ester
PeLED	Perovskite-based light emitting diode
P(τ)	Probability distribution
PCE	Power-conversion efficiency
PNC	Perovskite nanocrystal
PSC	Perovskite solar cell
RegA	Regenerative amplifier

k_{et}	Rate constant of electron transfer
k_{nr}	Rate constant of nonradiative relaxation
k_r	Rate constant of radiative relaxation
s	Second
SEM	Scanning electron microscope
STL	Solution temperature lowering method
SHG	Second harmonic generation
SOC	Spin orbit coupling
T	Temperature
τ_c	Truncation time
TiO_2	Titanium dioxide
UV or uv	Ultraviolet
VBM	Valence band maximum
Vis	Visible
V	Voltage
W	Watt
λ	Wavelength
XRD	X-ray Diffraction

Table of contents

Chapter 1
Introduction

Abstract

Halide perovskites emerge into a class of semiconductor materials for high-efficiency photovoltaic and optoelectronic devices. Their excellent optoelectronic properties, such as high photoluminescence quantum yields, halide- and size-dependent bandgap tuning, high absorption coefficients, high charge carrier mobility, and defect tolerance, have greatly attracted the entire semiconductor community. Nevertheless, understanding and optimizing the interfacial electron transfer and long-range charge carrier diffusion are important for future perovskite optoelectronics and photovoltaics. In this chapter, I briefly introduce halide perovskites, including their structure, synthesis, characterization, optical and charge carrier properties, and applications. At first, I introduce their history, summarizing their structures, chemical compositions, and stability factors. Next, I explain various perovskite nanocrystal synthesis methods to control the shape and dimensionality with suitable examples. The preparation methods for self-assembled perovskite nanocrystal thin films and different characterization techniques are discussed in the third section of this chapter. Further, I explain their bandgaps with the Jablonski diagram and the fundamentals of absorption and fluorescence spectroscopy. The fourth section describes the general charge carrier properties, including the charge carrier recombination mechanisms and their diffusion in single crystals and films. I provide the details of charge carrier diffusion lengths, time distributions, and diffusion coefficients. Also, the charge carrier properties and quantum confinement in single particles and closely packed films are explained. In the fifth section, I introduce the applications of halide perovskites to solar cells, photodetectors, and light-emitting diodes (LEDs) with details about the device architecture, carrier diffusion, and interfacial charge transfer mechanisms. In the final section, I summarize my motivation for this research, then classify the specific objectives of this thesis.

1.1 General introduction to halide perovskites

In the 1990s, the scientific and engineering communities started investigating halide perovskites due to their attractive optical and electronic properties, but the exploration was limited to transistors and light-emitting devices. Later, it took around two decades to discover the potential of these materials for practical applications.[1,2] Perovskite structures are named after the Russian mineralogist Lev Perovski. Initially, the perovskite describes $CaTiO_3$ discovered in the Ural Mountains by the German scientist Gustav Rose in 1839. Today, any materials with an ABX_3 structure are identified as perovskites. Generally, the A-site cation occupies the voids between the BX_6 octahedra, as shown in Figure 1.1, where A is a monovalent inorganic or organic cation [e.g., Cs^+, $HC(NH_2)_2^+$ (FA^+), or $CH_3NH_3^+$ (MA^+)], B is a divalent cation (e.g., Pb^{2+}, Ge^{2+}, Sb^{2+}, Sn^{2+}, etc.), and X is a halide ion (Cl^-, Br^-, or I^-).[3] The stability of the perovskite structures, based on the ABX_3 chemical formula and the radii (r_i) of the ions (A, B, X), has been extensively analyzed using the Goldschmidt tolerance factor (t):[4]

$$t = (r_A + r_X)/[\sqrt{2}(r_B + r_X)] \quad (1.1)$$

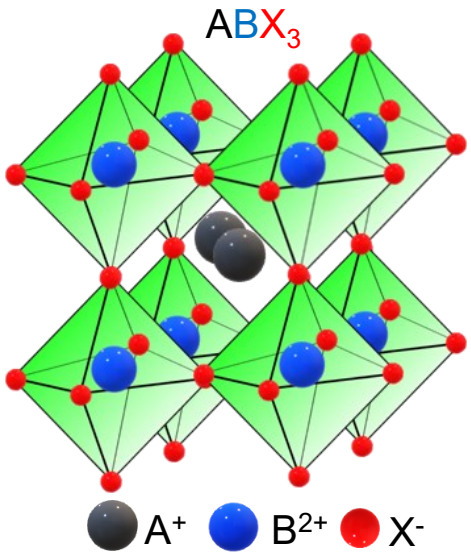

Figure 1.1. A halide perovskite unit cell.

where r_A, r_B, and r_X are the radii of A-cation, B-cation, and halogen ion, respectively. Generally, the tolerance factor should be 0.76−1.13 for stable three-dimensional (3D) perovskite structures.[5] Nevertheless, some other stable dimensionalities outside this range are reported. As a result, stable lead halide perovskites can be obtained using a limited number of A-cations

(Cs^+, MA^+, and FA^+). The octahedral structure stability can be further understood using an octahedral factor:[3]

$$\mu = r_B/r_X \quad (1.2)$$

The stability range is 0.44 to 0.900. Lead halide perovskites gained popularity due to their straightforward and cost-effective synthesis,[6-8] high photoluminescence quantum yields (PLQYs),[9,10] halogen- and size-tunable bandgap,[11,12] high photostability,[13] and versatile solution processability.[14,15] By building on pioneering advances in device engineering, researchers could significantly increase the power conversion efficiencies of perovskite photovoltaics and optoelectronics. Small stokes shifts,[16] high charge carrier mobility,[17] low Urbach energy,[18] long-range carrier diffusion,[19] and low trap density[20] of halide perovskites have led to lightning advances in photovoltaic and optoelectronic devices such as solar cells,[12,13,15,17,22] light-emitting diodes (LEDs),[23] lasers,[24] photodetectors,[25] transistors,[26] and single-photon devices.[27] Currently, the certified power conversion efficiency exceeds 25% for perovskite solar cells (PSCs),[28] and 22% for perovskite LEDs (PeLEDs).[29] In this regard, synthesizing high-quality and stable halide perovskites and characterizing their photophysical and optoelectronic properties are important for optimizing their devices.

1.2 Synthesis and characterization of halide perovskites

The halide perovskite synthetic methods are critical to obtaining a pure and perfect crystal structure that can be stabilized with desired ligand molecules or doped with inorganic salts. High-quality perovskite nanocrystal fabrication is achieved at low temperatures because of its ionically bonded crystal structure.[3] One can achieve a majority carrier type and concentration by treating with different molecules (ligands, or inorganic or organic salts).[29] However, the defect chemistry and physics for perovskites are still not understood precisely. Still, the energies from the vacancy-related defects are considered close to or within the bandgaps. Halide perovskites can be synthesized by several straightforward, scalable, and cost-effective methods.[4,5,8,9,30-33] Particularly, researchers have developed several techniques for controlling the size, shape, and quality of their optical properties. High-quality bulk perovskite crystals (micro to millimeter-scale) can be readily crystallized by the inverse temperature crystallization technique (ITC),[34] solution temperature lowering method (STL),[35] anti-solvent vapor-assisted crystallization (AVC),[36] or laser trapping induced crystallization method.[37] On the other hand, halide perovskite nanocrystals (PNCs) can be obtained by hot injection,[3,6] a

spray technique,[38] and the LARP method,[39] which are more convenient for fabricating thin-film devices. A scheme of the different synthetic methods for halide perovskite microcrystals, nanocrystals, quantum dots, and their films is given in Figure 1.2. The most common and traditional methods for synthesizing PNCs, and preparing their self-assembled films are discussed below.

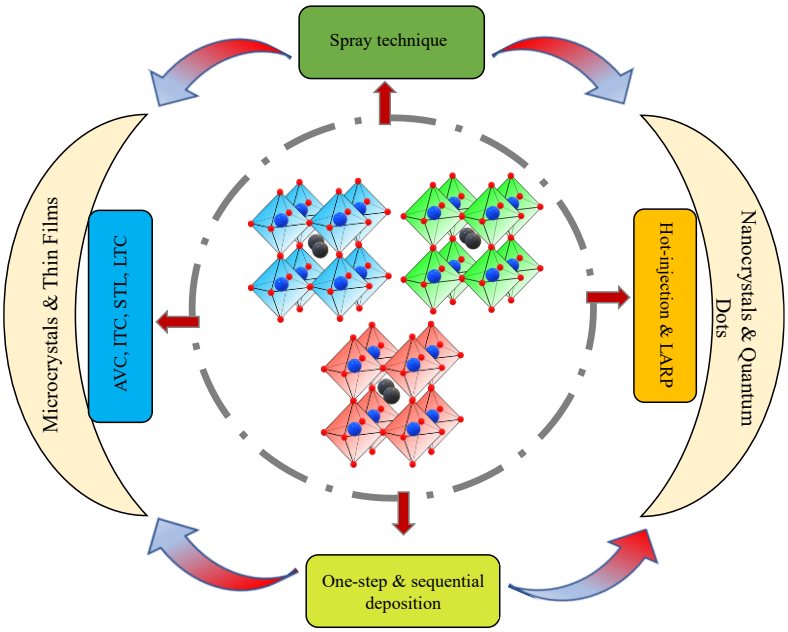

Figure 1.2. A scheme of halide perovskite synthetic methods.

1.2.1 Synthesis of nanocrystals

The optical and electronic properties of the halide perovskites are mainly dependent on the structure-dimensionality,[3,8,40] morphology,[41] and crystal phase.[3] For example, we can tune the optical properties of halide perovskites by achieving quantum confinement, i.e., by reducing the crystal size to the nanoscale. Halide perovskite quantum dots can be achieved readily by using long-chain amines or long-chain carboxylic acids and controlling the synthesis temperature.[42] Particularly, the octahedral unit plays an important role in controlling the binding energies and the emission wavelengths of halide perovskites.[8,42] Various synthetic approaches have been employed for obtaining defect tolerant crystals with narrow emission and tunable bandgaps. The hot injection and LARP techniques are the two well-known wet-chemical syntheses methods widely used for synthesizing high-quality PNCs. The synthesis of different dimensions (zero-dimensional, one-dimensional, two-dimensional, and three-

dimensional), and shapes using hot injection and LARP techniques are demonstrated in Figure 1.3A-C. In the hot injection method,[3,8,43] the ratio of precursors to surfactants, the injection temperature, the reaction time, and the precursors' concentration needs to be maintained precisely for controlling the size distribution and shape of PNCs. This traditional method is more convenient for separating the nucleation and growth stages and small nanocrystals with a uniform and narrow size distribution. When one injects the precursor mixture into the ligand mixture at 180-200 °C, the rapid depletion of the monomers concludes the nucleation stage.

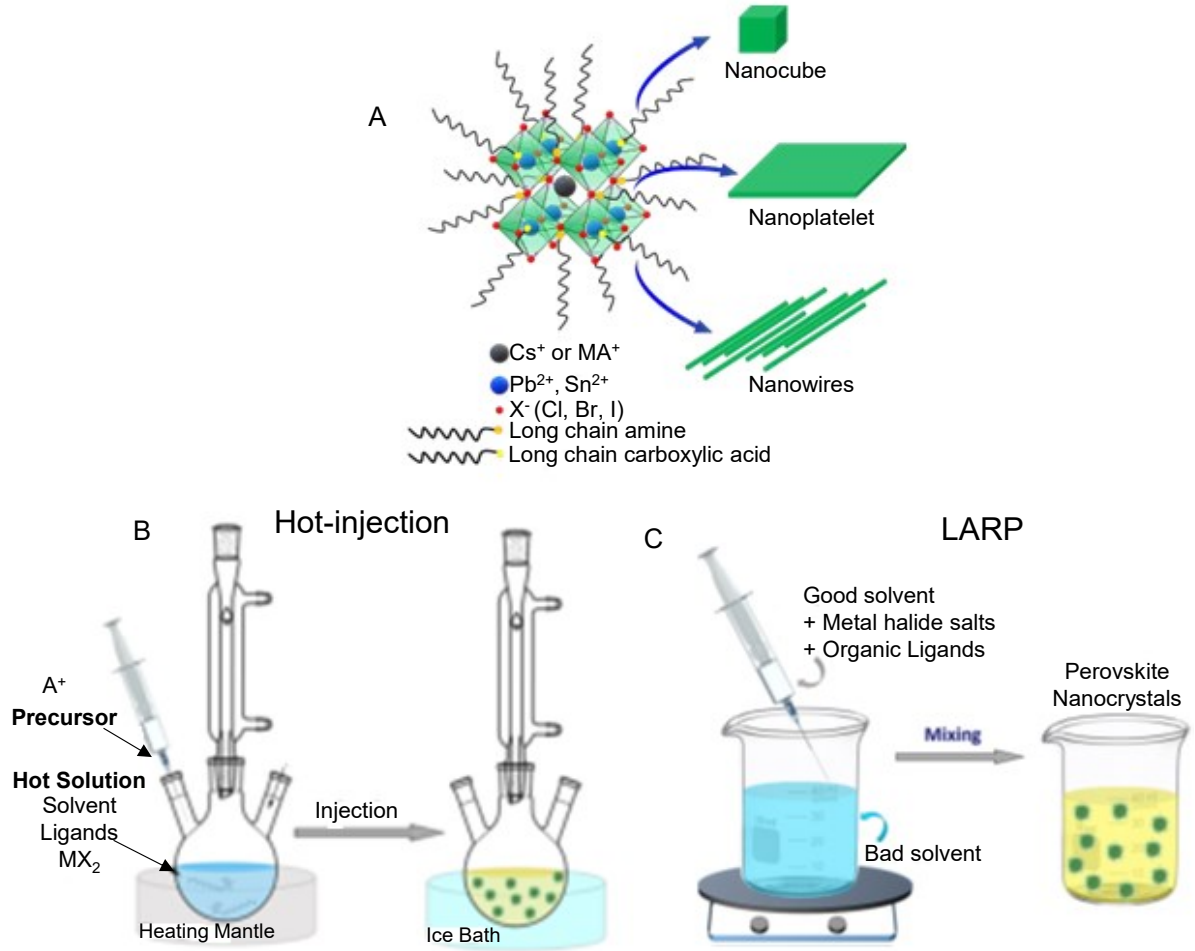

Figure 1.3. Synthesis schemes for (A) PNCs with different morphologies (B) hot-injection and (C) LARP methods. Reproduced from (A) Chouhan et al.[3] (B, C) Shamsi et al.[4]

The hot injection method was further extended by Protesescu et al. in 2015.[44] This was the first report of the colloidal synthesis of cesium $CsPbX_3$ (X = Cl, Br, and I) PNCs. They obtained $CsPbX_3$ PNCs by directly injecting the Cs-oleate into a mixture of PbX_2 salts, fatty acids, and alkyl amines dissolved in octadecene at a high temperature (140−200 °C). They discovered

that the PNC size could be controlled by varying the reaction temperature and the ratios of carboxylic acids and alkyl amines. The color tunability across the entire visible spectrum was also achieved by tuning the PNC size or by using different halide salts (Cl^-, Br^-, I^-). By simply varying the ratios of lead halide salts, they realized the mixed-halide PNCs. The growth kinetics of PNCs *via* the hot injection method was later investigated by Lignos et al.[45] Here, they used a droplet-based microfluidic platform to understand the $CsPbX_3$ PNCs growth and reported the fast reaction kinetics, where the nucleation and growth took place within the first 1-5 s of the reaction. In a subsequent study, a two-step growth mechanism was reported by Udayabhaskararao et al. in 2017.[46] By employing electron microscopy, they monitored the $CsPbX_3$ PNC growth, including a seed formation of Pb^o NCs followed by $CsPbX_3$ nucleation.

LARP method is the simplest and most cost-effective technique to synthesize colloidal PNCs.[3,8,47] At the equilibrium concentration of the precursors in a solvent, eventually attaining a nonequilibrium state of supersaturation help reprecipitate PNCs. The PNCs will be capped with long-chain acid or amine ligands, called ligand-assisted reprecipitation. Here, the supersaturated state can be achieved by evaporating the solvent, adding a poor solvent, or varying the temperature. In the LARP method, the nucleation and growth stages cannot be isolated in time, unlike in the hot injection method. This LARP method synthesis of PNCs was first demonstrated by Zhang et al. in 2015.[48] They simply dissolved the precursors ($PbBr_2$ and MABr) and ligands (alkyl amines and carboxylic acids) in DMF, and this clear precursor solution was injected into vigorously stirring toluene at room temperature and obtained colloidal $MAPbBr_3$ PNCs. Also, they investigated the role of alkylamines and carboxylic acids in controlling the size of PNCs by using various organic acids (oleic acid, butyric acid, octanoic acid) and amines (hexylamine, dodecyl amine, hexadecyl amine, octylamine). Surprisingly, they obtained PNCs without using the amines, but without a carboxylic acid, the reaction resulted in the aggregated PNCs. Over the years, different groups further optimized this approach to obtain PNCs with narrow size distributions.

Recently, Pushkarev et al.[49] developed a new spray technique for the fabrication of PNCs, which can be achieved at ambient conditions faster than other literature methods. They demonstrated a simple, scalable technique, where the precursor ink was sprayed onto a glass or ITO substrate resulting in high-quality $CsPbBr_3$ nanowires. Here, the clear precursor solution ($PbBr_2$ and CsBr in anhydrous dimethyl sulfoxide, DMSO) was taken in a vial with a spray cap, and the ink was spray cast onto the substrate. They found isolated droplets with a 0.5-2 mm diameter on the sprayed area. Interestingly, the crystallized PNCs showed the nanowire structure with excellent walls and end facets that are capable of lasing. This spraying technique

can be useful in the development of simple, stable, high-quality, and low-cost films for nanophotonic applications.

1.2.2 Preparation of thin films

Halide perovskite films are widely used as active layers in energy harvesting and light-emitting devices. The optical and electronic properties of the devices are mainly dependent on the surface chemistry and stability of the perovskite films.[50-52] For this purpose, the crystallization of perovskite thin films and their surfaces are widely investigated but are yet to be fully understood. These perovskite thin films can be fabricated in a single step or two steps deposition (Figure 1.4) of their precursor solutions using several methods such as spin coating,[53] hot-casting,[54] doctor-blade coating,[55] and spray coating.[56] For example, a single-step deposition of precursor salts (MAX, CsX, or FAX and PbX_2) dissolved in DMF, GBL, or DMSO on the substrate and drying and annealing give rise to brilliantly luminescent polycrystalline film.[57]

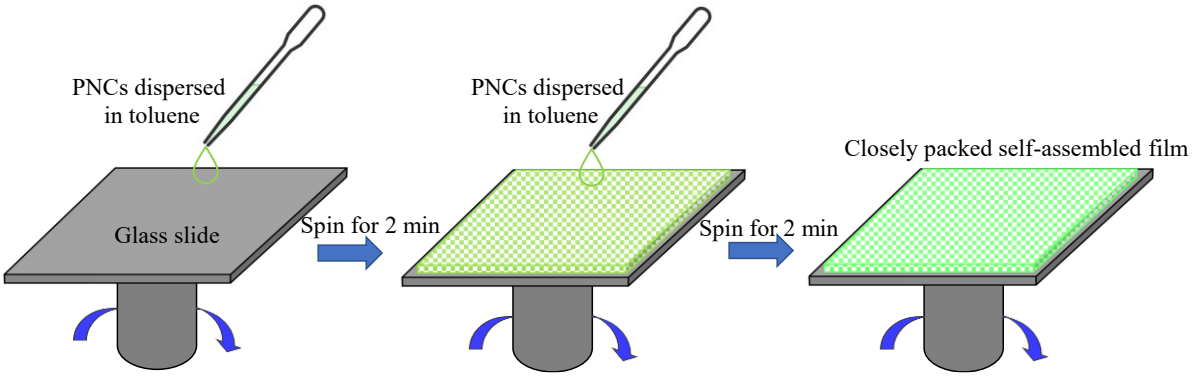

Figure 1.4. A scheme of layer-by-layer PNCs thin film fabrication by the spin-coating technique.

The nucleation and growth stages of the perovskites will be supported by the solvents' low vapor pressures and high boiling temperatures. Here, the film processing conditions play an important role in controlling the crystallization of perovskite thin films. In the case of sequential deposition, high-quality films can be prepared by depositing one of the precursor solutions on a substrate followed by coating another precursor solution, drying, and annealing.[58]

The most fascinating and challenging part of this perovskite thin-film preparation is fabricating halide perovskite nanostructures. Perhaps, the long-range charge carrier diffusion

is realized for PNC thin films where the closely packed PNCs could reduce the quantum confinement. In general, the dielectric screening is larger in PNC films, which dissociates excitons into free carriers and their migration.[59] Thus, preparing these closely packed nano-assemblies are more important to understanding the diffusion or migration of charge carriers. These ligand-assisted self-assembled films can be prepared by simple drop-casting or spin-coating techniques. For instance, PNCs dispersed in toluene are deposited on a substrate with lower rotations per minute (rpm, e.g., 100 rpm for 1 min) followed by a consecutive deposition with a higher rpm (1000 rpm for 3 min) and drying gives brilliantly luminescent nanocrystalline films.[60]

1.2.3 Characterization

Precise knowledge of the electronic structures, electronic/bandgap properties, and optical properties is mandatory to advance the science and technology of halide perovskites. Several modern electron microscopy and spectroscopy techniques have been employed to understand various properties of these materials, such as the chemical composition, surface chemistry, structural and morphological properties, optical properties, and electronic band structures. The routinely used transmission electron microscopy (TEM) and scanning electron microscopy (SEM) are more promising for investigating the structures and morphologies.[61,62] The size, shape, thickness, and stability of PNCs and their films can be explored using these microscopes. As shown in Figure 1.5A-D, the different shapes and sizes, such as nanorods, nanocubes, and nanosheets are detected using TEM. Also, the different dimensionalities like zero dimension, one-dimension, two-dimension, and three-dimension PNCs are revealed by TEM imaging. On the other hand, SEM could be more efficient in understanding the surface morphologies of perovskite films, including grain boundaries in nanocrystalline and polycrystalline films. Such grain boundaries and surface morphologies of halide perovskite thin films are widely studied using SEM, as shown in Figure 1.5 E, F. Similarly, SEM imaging is broadly extended to measure the thicknesses of thin films by cross-section analysis. Atomic force microscopy (AFM)[63] is another candidate to measure and visualize PNCs and their surfaces at high resolutions.

Researchers in the materials science field are fascinated by the excellent luminescence properties of halide perovskites. Understanding the absorption and emission properties of halide perovskites is essential to advance their practical applications. The optical properties of halide perovskites are extensively investigated using UV-vis absorption and steady-state

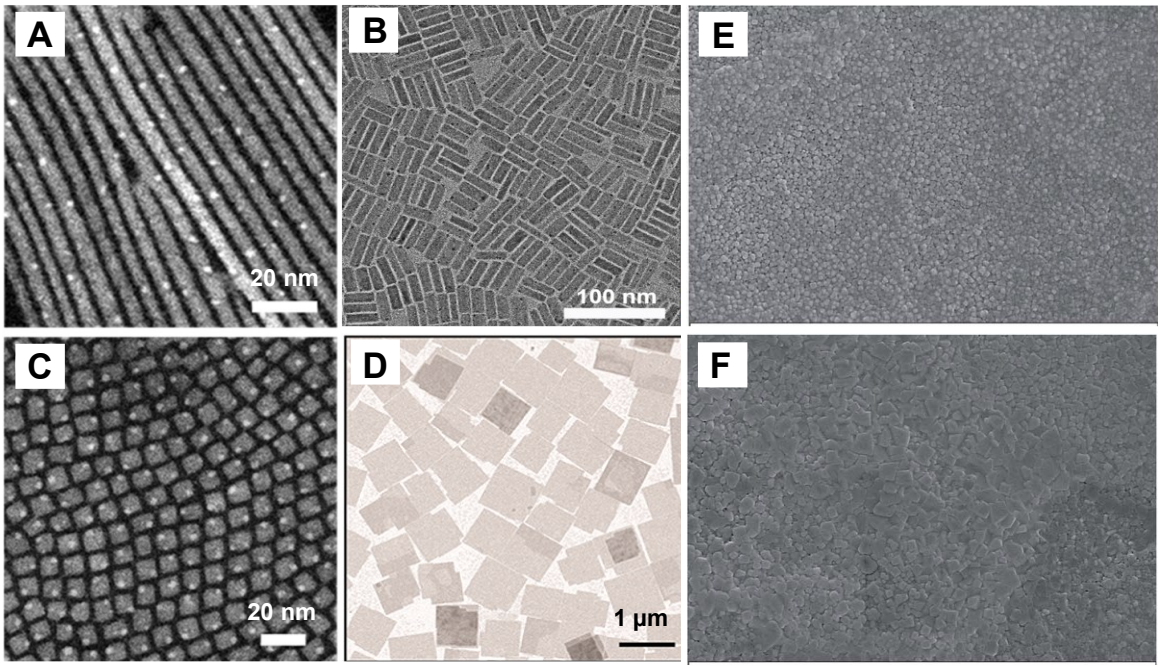

Figure 1.5. Characterization of halide perovskites. (A-D) TEM images showing different shapes and sizes of $CsPbBr_3$ PNCs. (E, F) SEM images of $MAPbI_{3-x}$ Cl_x mixed halide perovskite films. Reproduced from (A, C) Dang et al.,[64] (B) Wang et al.,[65] (D) Shamsi et al.[66] and (E, F) Heo et al.[67]

fluorescence spectroscopic methods. Since halide perovskites absorb light from the UV-vis region to the near-infrared (NIR) region by engineering the halide composition, one can perform the bandgap tuning experiments by simple halide mixing or halide exchange reactions[68,69] and monitor the change by UV-vis absorption and fluorescence analyses. For example, the blue emission and near UV absorption of $CsPbCl_3$ can be shifted to green by treating with Br^-, which further shifts to red by exchanging with I^-. This halide exchange-induced bandgap tuning of $CsPbX_3$ and the corresponding absorption and photoluminescence (PL) spectra are shown in Figure 1.6A. The uniform size distribution of PNCs could be recognized with excitonic absorption band edges. The aggregates of PNCs and bulk crystals result in light scattering in the absorption spectra. The halide perovskites absorption edges are blue-shifted relative to their emission maxima, providing a few to a few tens' nanometer stokes-shift.[70,71]

The atomic and molecular structures of the materials are widely studied using X-ray diffraction (XRD) analyses.[72] The halide perovskite crystal phases are realized by both powder XRD and single-crystal XRD techniques. Generally, halide perovskites are tetragonal at room temperature, and other crystal phases are observed at low and high temperatures.[73] For example,

the high-temperature synthesis can result in the cubic-phase perovskites, whereas the orthorhombic phase is achieved in low-temperature experiments. The different crystal phases of halide perovskites are broadly studied by XRD analyses. The XRD patterns of $CsPbX_3$ PNCs and mixed halide perovskites are represented in Figure 1.6B. The elemental composition of the

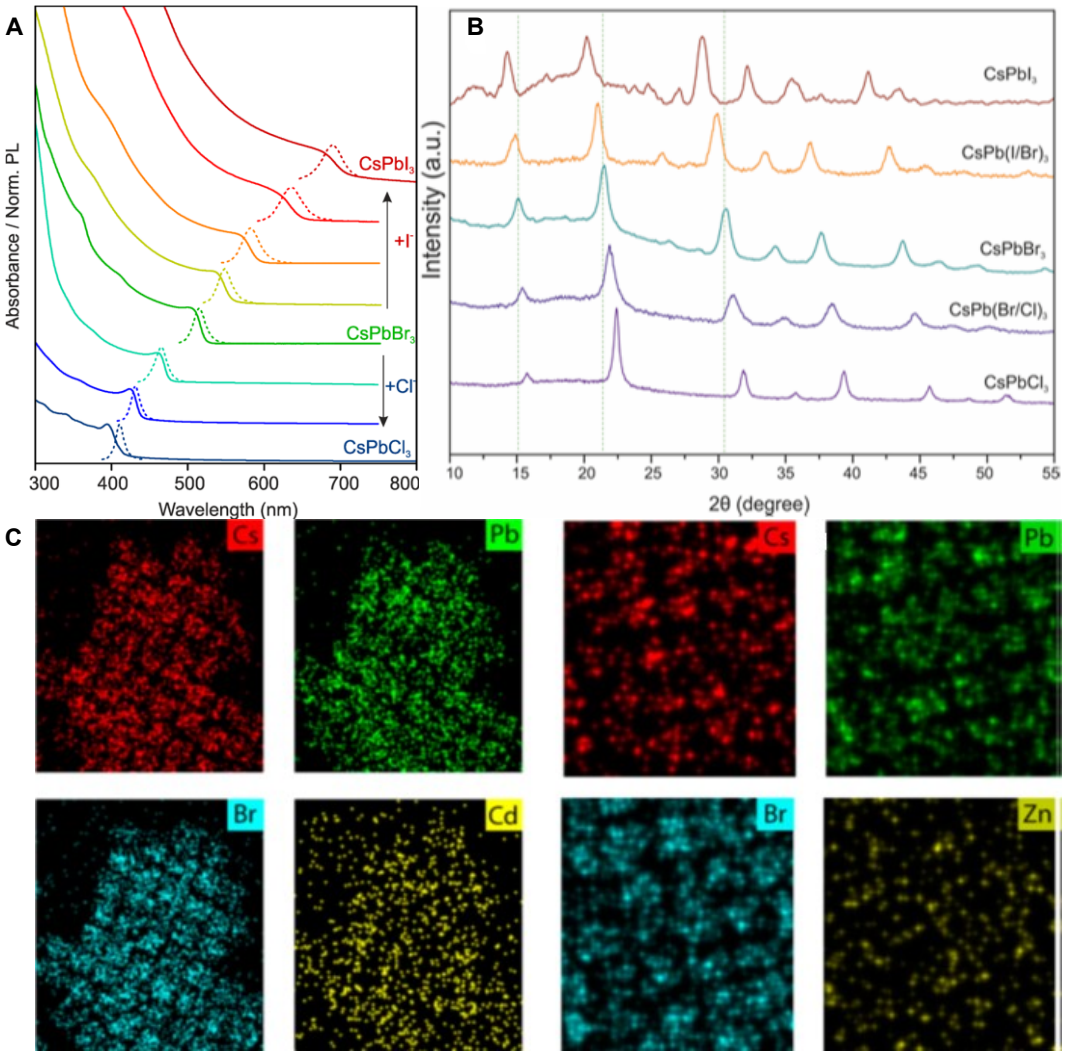

Figure 1.6. Characterization of halide perovskites. (A) Absorption and PL spectra of $CsPbX_3$ (X= Cl, Br, I) PNC solutions. (B) XRD patterns of $CsPbX_3$ and mixed halide perovskite powders. (C) Energy-dispersive X-ray spectroscopy (EDS) mapping of $CsPb_{1-x}Cd_xBr_3$ and $CsPb_{1-x}ZnxBr_3$ nanocrystals. Reproduced from (A, B) Protesescu et al.[74] and (C) Der Stam et al.[75]

halide perovskites are examined using EDS. For instance, as shown in Figure 1.6C, the elemental composition of $CsPbBr_3$ doped with other divalent ions like Zn^{2+}/Cd^{2+}/Sn^{2+} resulted in the lattice contraction. Here the smaller ionic radii of the newly doped divalent cations helped

in the lattice contraction, and EDS analyses confirm the doped ions. It is easy to disclose the elements' ratio in the crystal phase.[76] All the cations to anions ratios present in the halide perovskite structures could be recognized using EDS. Hence, this technique is more efficient in developing novel perovskites doped with desired elements. The other properties like electronic and photoexcited states of halide perovskites are explored by using advanced characterization techniques such as time-resolved PL spectroscopy, transient absorption (TA) spectroscopy, and single-photon counting techniques.

1.3 Properties of halide perovskites

1.3.1 Bandgaps

The band structures and the density of states substantially control the optical properties of halide perovskites. Hence it is necessary to explore their electronic structural disorders, dimensionality, and material composition to advance optoelectronic applications.[77-79] The main optoelectronic properties of halide perovskite, including the charge carrier mobility, excited-state lifetime, carrier recombination dynamics, and intrinsic carrier concentration, can be manipulated by controlling the structural framework. In halide perovskites, the conduction band minimum (CBM) is formed by hybridizing 6p-orbitals of Pb and s- and p-orbitals of halide. The valence band maximum (VBM) comprises 6p- and 6s-orbitals of Pb and s-and p-orbitals of halide. By varying the halide composition, one can easily tune the bandgap of these materials. For example, the change in the halide from Cl to Br and Br to I increases the contribution of the halide p-orbitals to the VBM. Dynamically, this contribution favors the orbital mixing between the Pb s-orbital and halide p-orbital to a considerable extent.[80] This increase in the contribution of halide p-orbitals lowers the optical band-gap energy in the order of Cl > Br > I. The band-edge states of lead halide perovskites are represented in 1.7A.

In general, the direct band-gap nature of halide perovskites is a deep-rooted concept, but the noncentrosymmetric lattice recently suggests Rashba or Dresselhaus band splitting in halide perovskites.[81] Quantum confinement in halide perovskites is generally tiny, and also, when the electron-hole exchange interaction becomes predominant, one obtains an exciton state like 0 or 1 J values, and this is mainly due to the Rashba effect, or inversion symmetry breaking. The strong momentum-dependent interaction by the heavy nucleus of the lead is causing this spin-orbital coupling, splitting the exciton states into singlet and triplet states.[82] According to the angular momentum projections of the Rashba effect, the band edge further degenerates into three triplet states, as shown in Figure 1.7B. The spin-orbital coupling in the

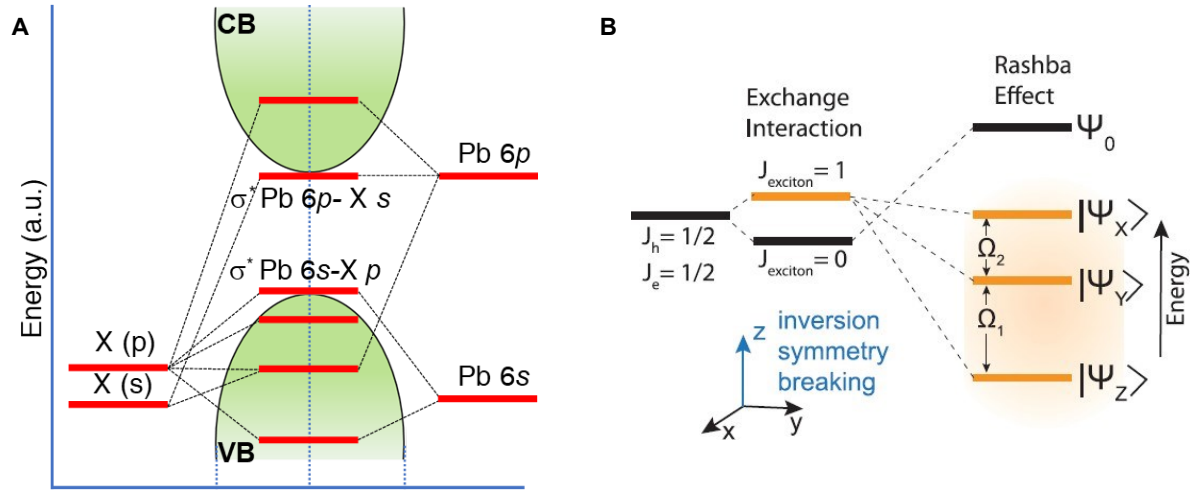

Figure 1.7. (A) Band-edge states of lead halide perovskites. (B) Spin-orbit coupling and the total angular momentum of the electron states. Reproduced from (A) Chouhan et al.[3] and (B) Utzat et al.[83]

lead halide perovskites is well-known for tuning the optical properties by manipulating the CBM. The constitution of both A-site and B-site cations and octahedral tilting play an important role in the electronic structure and optoelectronic properties.[84] The PbX_6 octahedra undergo tilting, depending on the corresponding A-site cation. For example, The Pb-X-Pb dihedral angle decreases from 180° to 163° or 153° by reducing the size of A-site cations from larger to smaller [$CH(NH_2)^{2+}$ (FA) >$CH_3NH_3^+$ (MA)> Cs^+], which results in the octahedral tilting. Figure 1.8 exhibits the octahedral structure of PbX_6 without and with tilting the dihedral

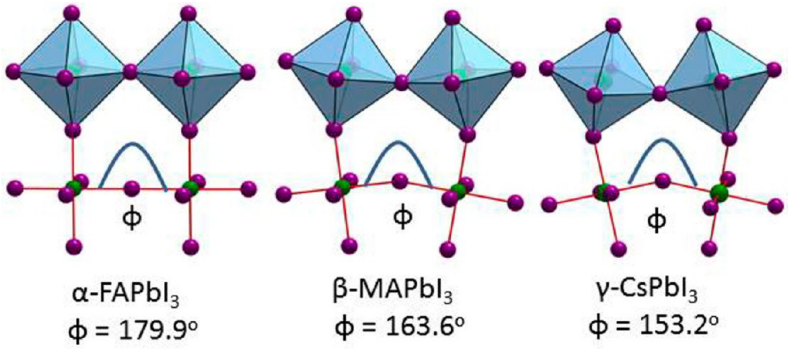

Figure 1.8. Structural deformations in halide perovskites induced by the A-site cation size. Reproduced from Manser et al.[91]

angle from 180° for FA^+ to 163.6° for MA^+ and 153.2° for Cs^+. The orbital overlap between Pb and X is lowered due to the octahedral tilting, which mainly weakens the spin-orbital coupling. Hence, the contribution of Pb orbitals to the band-edge is considerably decreased. However,

the octahedral tilting is not only size-dependent on the A-site cation but also changes the crystal phase. It is well established that changes in the temperature and pressure cause a series of phase transformations.[85] Consequently, the optical properties are modified. The strongly quantum confined PNC structures such as two-dimensional nanoplatelets or nanosheets are expected to have large lattice distortions compared to the three-dimensional nanocubes, which result in blue-shifted absorption and emission spectral maxima.[86]

1.3.2 Absorption and photoluminescence properties

The optical properties of halide perovskites are widely studied using UV-vis absorption and fluorescence spectroscopic methods. The band-gap tuning, quantum confinement, and electronic transition of PNCs can be understood using these fundamental methods, which provide details about the absorption/emission-concentration relations as a function of the wavelength.[87,88] Halide perovskites under UV light illumination undergo electronic transitions from the ground to the excited state, which consists of multiple vibrational and rotational transitions. The PL of halide perovskites can be tuned from the UV-vis to the NIR region by the quantum confinement effect and simple halide exchange reactions, as shown in Figure 1.9A-C.

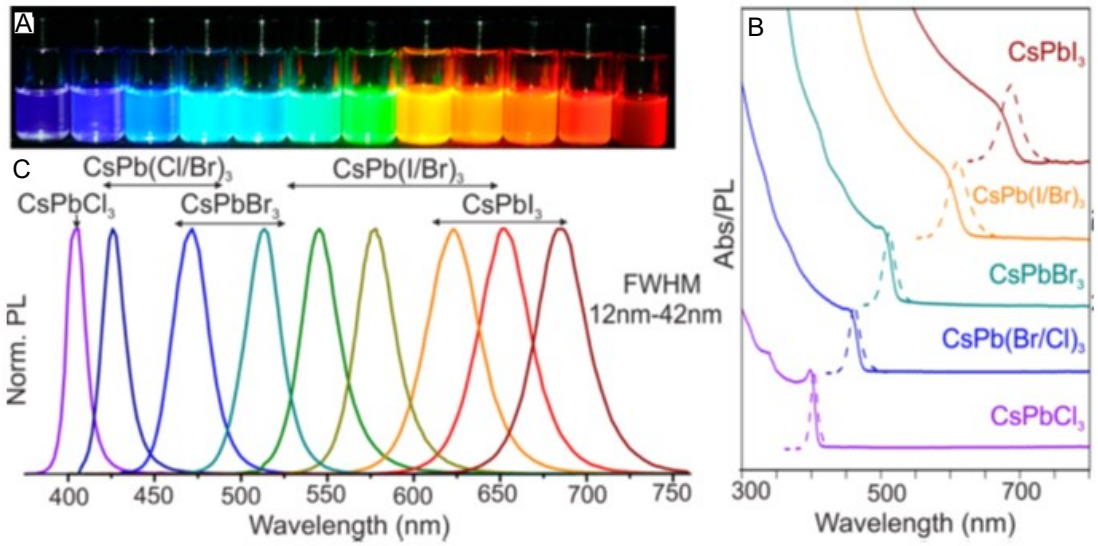

Figure 1.9. Halide- and size-dependent bandgap tuning in halide perovskites: (A) colloidal $CsPbX_3$ PNCs dispersed in toluene and taken under UV light. (B) PL spectra of mixed halide perovskites with FWHM 12-42 nm. (C) The corresponding UV-vis absorption and PL spectra. Reproduced from Protesescu et al.[44]

Classically, the Franck-Condon factor determines the electronic transition probability. According to the Franck-Condon principle, electronic transitions take place vertically in a potential well while maintaining the positions of the nuclei or the internuclear distance. Light absorption can be determined by a particular transition probability between the ground (S_0) and the excited electronic states (S_1). Electronic energy levels and vibrationally-coupled electronic transitions in simple molecules are models for understanding the absorption features of PNCs. The total energy of a molecule is given by

E = kinetic energy + potential energy

$$E = k + V; \tag{1.3}$$

$k = \frac{1}{2}mx^2$; x is the position operator

$$k = \frac{1}{2}mx^2 = \frac{p2}{2m} \tag{1.4}$$

$$\text{or } E = \frac{p^2}{2m} + V \tag{1.5}$$

The quantum mechanical form of this equation in one dimension is

$$E\psi = -\frac{\hbar^2}{2m}\frac{\partial^2\psi}{\partial x^2} + V\psi \tag{1.6}$$

The total energy is represented by the momentum operator $-i\hbar\frac{\partial}{\partial t}$

$$\therefore -i\hbar\frac{\partial}{\partial t}\psi = -\frac{\hbar^2}{2m}\frac{\partial^2\psi}{\partial x^2} + V\psi \tag{1.7}$$

For the particle in three dimensions,

$$-i\hbar\frac{\partial}{\partial t}\psi = -\frac{\hbar^2}{2m}\nabla^2\psi + V\psi \tag{1.8}$$

This particle in a box behaves like a wave. The corresponding de Broglie wavelength is

$$\lambda = \frac{h}{p} \tag{1.9}$$

The probability of finding the particle in the box is determined by the wave's amplitude, which is zero at the walls of the box. Therefore, the box length must be integral multiples of λ

$$\text{Or } L = \frac{n\lambda}{2};\ \lambda = \frac{h}{p} \tag{1.10}$$

$$\therefore E = \frac{h^2}{8m}\frac{n^2}{L^2} \tag{1.11}$$

Equation (1.11) defines the vibrational states in a potential well (Figure 1.10) or the electronic state of a molecule.

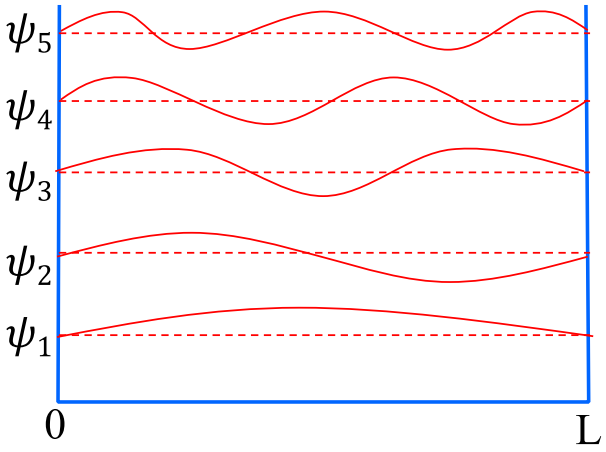

Figure 1.10. A scheme of vibrational states in a molecule.

Considering the molecule, a harmonic oscillator, the potential energy is

$$V = \int_0^x f dx = \int_0^x kx\, dx = \frac{1}{2}kx^2 \tag{1.12}$$

$\therefore$ Equation (1.6) becomes

$$E\psi = -\frac{\hbar^2}{2m}\nabla^2\psi + \frac{1}{2}kx^2\psi \tag{1.13}$$

The oscillator takes the values

$(V + \frac{1}{2})\ \hbar\sqrt{k/m}$ with the selection rule $\Delta V = \pm 1$

Therefore, an electronic excitation (for v to v' states) by the absorption of a photon is represented by the energy change

$$\Delta E = h\nu = (v + \frac{1}{2})\ \hbar\sqrt{k/m} - (v' + \frac{1}{2})\ \hbar\sqrt{k/m} \tag{1.14}$$

During such excitation by the absorption of a photon, the angular momentum or the spin is conserved. Therefore, the total angular momentum J changes by $\Delta \underset{J}{\rightarrow} = \pm 1$. Also, from the initial (i) state to the final.

$$| J_i + 1 | > |J_f| > |J_i - 1|$$

The selection rule for angular momentum change is $\Delta J = 0, \pm 1$

The rate of absorption of photons for the following transitions (Figure 1.11) between the two states E_1 and E_2 is

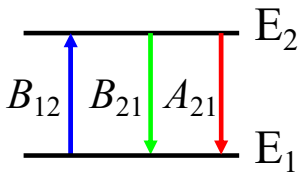

Figure 1.11 A scheme of electronic excitation and relaxation.

$$B_{12} = \frac{2303}{h\bar{\upsilon}N} \int \mathcal{E} d\bar{\upsilon} \tag{1.15}$$

Where N is the Avogadro number, $\mathcal{E}$ is the molar extinction coefficient, and $d\bar{\upsilon}$ is the transition bandwidth. The intensity of transition is defined in terms of the oscillator strength f,

$$f = \frac{m_e h c^2 \bar{\upsilon}}{\pi e^2} B_{12} \tag{1.16}$$

Where m_e is the reduced electron mass.

$$\therefore f = \frac{2303\, m_e c^2}{N \pi e^2} \int_{\bar{\upsilon}_1}^{\bar{\upsilon}_2} \mathcal{E} d\bar{\upsilon} \tag{1.17}$$

The intensity of lines, also called the molar absorption coefficient, is given by the overlap integral between the electronic and vibrational wave functions in the initial and final states. The overlap integral is called the Franck-Condon factor.

A simplified Jablonski diagram for an electronic excitation from the ground (S_0) to the excited (S_1) states is shown in Figure 1.12. The intensity of lines ($< \mu >$) for the excitation or transition in Figure 1.12 is given by the sum of the transition dipole moments of individual atoms.

$$< \mu > \; = \; < \psi_{S_1} | \hat{\mu} | \psi_{S_0} > \tag{1.18}$$

Where ψ_{S_1} and ψ_{S_0} are the total amplitudes of the active modes (wave functions) in the excited (S_1) and the ground (S_0) states, and $\hat{\mu}$ is the dipole moment operator. Considering the electronic (ψ_e) and nuclear (ψ_N) wave functions,

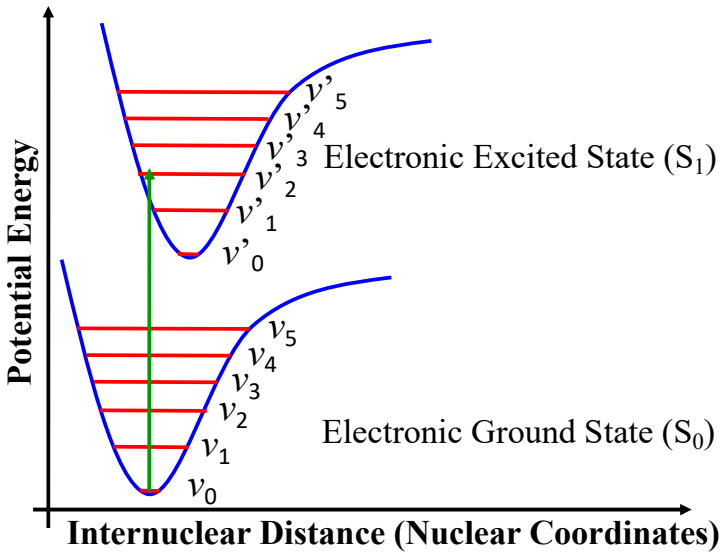

Figure 1.12. A simplified Jablonski diagram and an electronic excitation.

$$\psi_{S_1} = \psi_{es_1}\psi_{Ns_1} \tag{1.19}$$

$$\psi_{S_0} = \psi_{es_0}\psi_{Ns_0} \tag{1.20}$$

Also, the dipole moment operator is separated into the electronic and nuclear components.

$$\text{Or } \hat{\mu} = \hat{\mu}_e + \hat{\mu}_N \tag{1.21}$$

$$\therefore < \mu > \; = \; < \psi_{es_1}\psi_{Ns_1}|\hat{\mu}_e + \hat{\mu}_N|\psi_{es_0}\psi_{Ns_0} > \tag{1.22}$$

Here $\psi_{es_1}\,\psi_{Ns_1}$ and $\psi_{es_0}\psi_{Ns_0}$ are complex conjugates. Therefore, by separating the conjugates,

$$< \mu > \; = \; < \psi_{es_1}\psi_{Ns_1}|\hat{\mu}_e|\psi_{es_0}\psi_{Ns_0} > + < \psi_{es_1}\psi_{Ns_1}|\hat{\mu}_N|\psi_{es_0}\psi_{Ns_0} > \tag{1.23}$$

However, the nuclear dipole moment depends only on the nuclear wave function. Similarly, the electronic dipole moment depends only on the electronic wave function. Therefore, equation (1.23) becomes,

$$< \mu > = < \psi_{Ns_1}|\psi_{Ns_0} >< \psi_{es_1}|\hat{\mu}_e|\psi_{es_0} > +$$

$$< \psi_{es_1}\psi_{es_0} >< \psi_{es_1}|\hat{\mu}_N|\psi_{es_0} > \tag{1.24}$$

Also, the solutions to the Schrödinger equation for the ground and excited states form orthonormal sets.

$$\text{i.e., } < \psi_{es_1}|\psi_{es_0} > = 0 \tag{1.25}$$

$$\therefore < \mu > \; = \; < \psi_{Ns_1} | \psi_{Ns_0} > < \psi_{es_1} | \hat{\mu}_e | \psi_{es_0} > \qquad (1.26)$$

Here, $< \psi_{Ns_1} | \psi_{Ns_0} >$ is the vibrational overlap between the states in S_1 and S_0. It is called the Franck-Condon factor. The second term $< \psi_{es_1} | \hat{\mu}_e | \psi_{es_0} >$ is the intensity factor.

Nanoscale structures of the halide perovskites with many surface ligands show several vibrational transitions and inhomogeneities of vibrations. However, the rigid lattice structure, high state density, and halide perovskites' direct bandgap nature result in smooth absorption spectra with intense bands.

The optical properties of the halide perovskites can also be realized using fluorescence or PL spectroscopy. Before exciton relaxation (radiative or non-radiative) in a photoexcited halide perovskite, thermal relaxation takes place to the lowest vibrational level of the excited state. Conversely, lattice vibrations cause internal conversion in PNCs. It is well known that a photoexcited PNC relaxes from the lowest unoccupied molecular orbital (LUMO) or the conduction band minimum to the highest occupied molecular orbital (HOMO) or the valence band maximum within 10^{-10}~10^{-8} s, preserving the electron spin. Spin forbidden transitions in some materials or molecules follow intersystem crossing to release phosphorescence. The phosphorescence relaxation occurs in about 10^{-7}~10^{-4} s. Various relaxation processes of a photoexcited molecule can be represented in the Jablonski diagram in Figure 1.13.

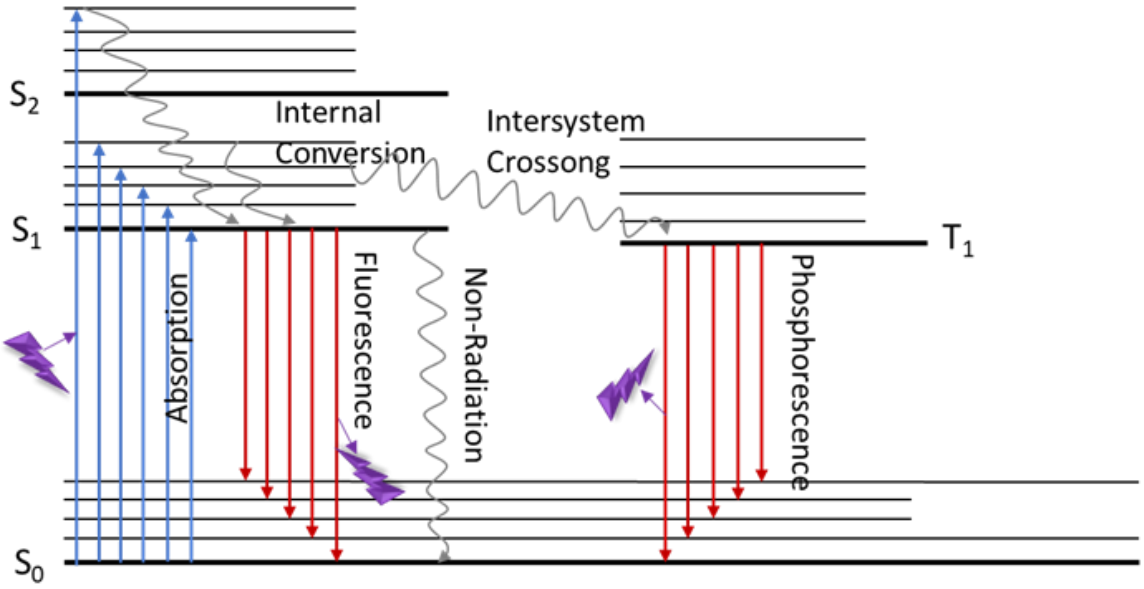

Figure 1.13. A simplified Jablonski diagram showing photoexcitation and relaxation processes for molecular systems.

The fluorescence quantum efficiency (ϕ_F) and lifetime (τ_F) are the main characteristics of fluorescence. Also, the electronic properties of PNCs can be understood from the shapes of the fluorescence and absorption spectra and Stokes shifts. The steady-state and time-resolved fluorescence methods are the two well-known techniques for measuring PL spectra, estimating ϕ_F, and τ_F values. ϕ_F is the ratio of the number of emitted photons to the number of absorbed photons. Like a photoexcited chromophore, a PNC relaxes to the lowest vibrational level of the excited state, followed by radiative or nonradiative relaxations. The nonradiative paths lower the ϕ_F value. Overall, vibrationally-coupled electronic relaxations and defect- or charge-assisted nonradiative relaxation lower the ϕ_F value.

Relative fluorescence spectral measurements of a reference and a sample solution help calculate the ϕ_F value using the following equation

$$\phi_F = \phi_R \times \frac{A_R}{A_S} \times \frac{\mathrm{IF_S}}{\mathrm{IF_R}} \times \left(\frac{\mu_S^2}{\mu_R^2}\right) \tag{1.27}$$

where, ϕ_R is the fluorescence quantum yield of the reference such as a laser dye, A_R and A_S are the absorbencies of the reference and the sample at the excitation wavelength selected for fluorescence spectral measurements, IF_R and IF_S are the integrated fluorescence intensities of the reference and the sample, and μ_R and μ_S are the refractive indices of the solvent in which the reference and the sample are dissolved. I estimated the ϕ_F values of PNC samples by this relative method using fluorescein as the reference.

The fluorescence quantum yield of a PNC is also related to the τ_f value, which is the mean lifetime of the excited state. The general relationship between the fluorescence intensity and the lifetime is

$$I = I_0\, e^{-t/\tau_F} \tag{1.28}$$

Where *I* is the intensity at time 't' and I_0 is the absolute fluorescence intensity. The absolute lifetime (τ_0), the value when there is no nonradiative process competing with radiative relaxation of a species is related to the measured lifetime (τ_F) and the ϕ_F values by

$$\phi_F = \frac{\tau_F}{\tau_0} \tag{1.29}$$

Also, the lifetime is the inverse of the relaxation rate. Therefore,

$$\tau_0 = \frac{1}{k_r} \tag{1.30}$$

$$\tau_F = \frac{1}{k_r + k_{nr}} \tag{1.31}$$

$$\therefore \phi_F = \frac{1}{k_r + k_{nr}} \div \frac{1}{k_r} = \frac{kr}{k_r + k_{nr}} \tag{1.32}$$

Where k_r and k_{nr} are the rates of radiative and nonradiative relaxations of an excited PNC. The Stokes shift (equation 1.33) in the absorption-emission spectra shows the difference in the 0-0 transitions.

$$\text{Stokes shift} = 10^7 \left(\frac{1}{\lambda_{ex}} - \frac{1}{\lambda_{em}}\right) \tag{1.33}$$

Stokes shift values are related to the energy dissipated by the excited state relaxation. A physical picture of Stokes shift is the difference in wavelengths between the absorption and fluorescence spectral maxima. The direct bandgap nature of halide perovskites results in small Stokes shift values.

1.3.3 Charge carrier properties

The precise knowledge of the charge carrier properties of halide perovskites is significantly important to advancing photovoltaic and optoelectronic applications. Halide perovskites are well known to exhibit long charge carrier lifetimes, high charge carrier mobility, and long-range carrier diffusion. The photoexcited excitons get converted into hot charge transfer states that dissociate into free charge carriers in about 1 ps or less by charge transport.[89,90] Numerous charge carrier lifetimes have been reported for halide perovskites. In particular, the electron quantum distribution, dielectric screening, exciton binding energy, exciton diffusion, etc., play a significant role in defining the lifetime (Figure 1.14A).

Closely packed PNC films induce large dielectric constants and low exciton binding energies. The electron mean-free path in halide perovskites is generally 10 to 30 nm, and electron delocalization and hole localization can occur. According to the high-resolution STEM/TEM images, the inter PNC distance in a film is about 1.6 nm, which is in the order of the ligand length (oleic acid/oleyl amine). The early excitons split into free carriers, and their migration lowers the recombination rates (Figure 1.14B). Thus, understanding the diffusion of

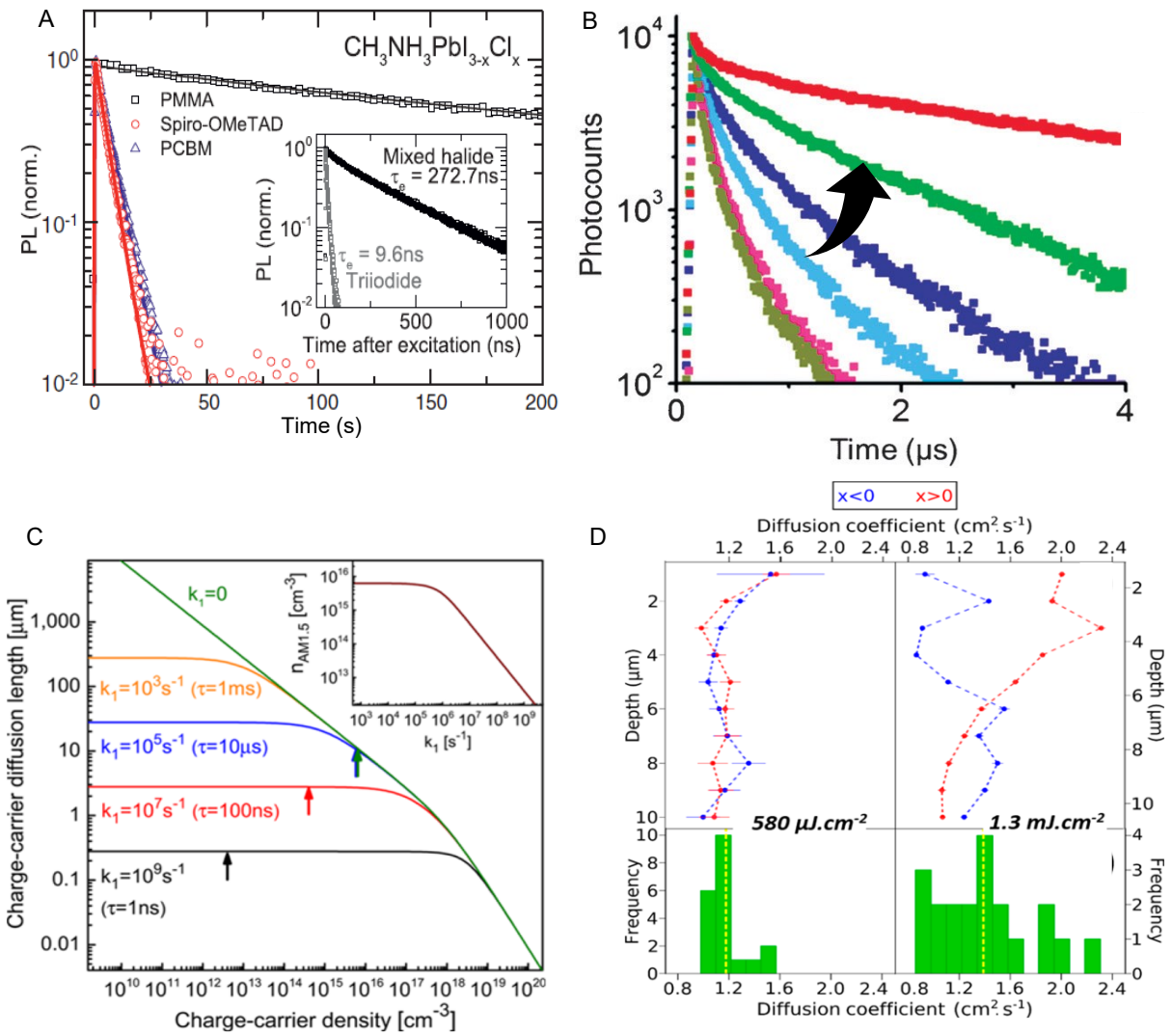

Figure 1.14. Time-resolved PL decays of (A) a mixed halide perovskite and (B) a $FAPbBr_3$ PNCs film. (C) Various carrier diffusion lengths for $CH_3NH_3PbI_3$. (D) Statistics of the depth-dependent diffusion coefficients in $MAPbBr_3$ single crystals. Reproduced from (A) Stranks et al.[92] (B) Nair et al.[76] (C) Manser et al.[91] (D) Stavrakas et al.[93]

charge carriers in close-packed PNC films is more important to lowering the recombination rates. Thermal energy (k_BT)[91] contributes considerably to the carrier diffusion in halide perovskites. By knowing the charge carrier lifetime (τ) and diffusion coefficient (D), we can calculate the diffusion length (L_D) using,

$$L_D = \tau D \tag{1.34}$$

According to Einstein relation, the field-free diffusion can be directly related to the carrier mobility (μ)

$$\mu = Dq/k_B T \quad (1.35)$$

where q is the electronic charge, k_B is Boltzmann's constant, and T is temperature.

We can estimate LD using eq by determining the charge carrier lifetime and diffusion coefficient or mobility. 1.34. Halide perovskite's time distribution can be explained by the time-dependent partial differential equation.

$$\partial n/\partial t = D\nabla^2 n - k_1 n - k_2 n^2 - k_3 n^3 \quad (1.36)$$

where, k_1, k_2, and k_3 are the recombination processes, ∇ is Laplace operator, n is the carrier population, and D is the diffusion coefficient. Different charge carrier diffusion and recombination rates can be understood using the above equations. Figure 1.14C demonstrates the calculated carrier diffusion length in $CH_3NH_3PbI_3$.

The charge carrier recombination in halide perovskites can be explained by a differential equation 1.37,

$$d_n/d_t = -k_3 n^3 - k_2 n^2 - k_1 n \quad (1.37)$$

where n is the concentration of total charge carriers.

For understanding the carrier diffusion pathways, it is necessary to estimate the diffusion coefficients. Defects in the crystals and local properties can significantly alter the diffusion coefficients. As shown in Figure 1.14D, a large dispersion of local diffusion coefficients ranging from 0.3 and 2 cm^2s^{-1} has been reported for single crystals, depending on the trap density and the crystal morphology. The monomolecular,[92] bimolecular,[93] and Auger recombination[94] rates depend mainly on carrier lifetimes, mobility, and diffusion lengths. Trap states influence the monomolecular recombination rate. However, the small exciton binding energies in thin films make fewer contributions to the excitonic recombination. It is well established that the exciton recombines with a trap in the bandgap. Therefore, the number of trap states in a perovskite crystal is directly attributed to the monomolecular recombination rates.

In the case of bimolecular recombination, the charge carriers are influenced by the halide and B-site cation compositions.[95] This process is dominant at moderate charge carrier density. Radiative recombination is the dominant relaxation pathway when the trap state concentration

is low. Moreover, the Auger-assisted recombination in perovskite dominates at high-intensity excitations and high charge carrier concentrations. In general, the free carriers in low-mobility systems favor Langevin recombination, which occurs when excitons are inside their joint Coulombic radius. This recombination mechanism is completely different from the bimolecular recombination rate in halide perovskites. Therefore, the non-Langevin bimolecular recombination in halide perovskites indicates high carrier mobility, which lies between 1 to 10 $cm^2 V^{-1} s^{-1}$.[3,8,93]

1.3.4 Photoluminescence blinking

The stochastic PL fluctuations in halide are commonly referred to as PL blinking.[97] The photoexcited state properties of single PNCs have been widely investigated in terms of PL blinking. This PL blinking is one of the most critical issues for efficiently capturing generated carriers. The bright state in the PNC blinking is the ON state, and the dark state is the OFF state (Figure 1.15A). At first, two types of blinking mechanisms were reported by Galland et al.[98] for chalcogenide quantum dots. Later, similar mechanisms were assigned to perovskite nanocrystals. The two mechanisms, A- and B-type blinking, help understand the PL blinking response in PNCs: i) the charging-discharging model (type-A)[99] and ii) activation-deactivation of nonradiative recombination centers (type-B)[100] to explain the ON/OFF events. The charged state can initiate a nonradiative Auger recombination process in type-A blinking *via* the flow of exciton energy to a third carrier (either an electron or a hole). In type-B blinking, shallow surface traps in PNCs, also called multiple recombination centers, undergo random activation and deactivation, causing a constantly changing nonradiative recombination rate and the band-edge carrier blinking. These PL blinking mechanisms are represented in Figure 1.15B, C.

1.3.5 Photoluminescence enhancement

It is well established that the optical and charge carrier properties of halide perovskites enhance by coupling with the surface plasmon. The surface plasmonic property is predominantly observed in noble metallic NPs such as Au, Ag, Pt, Al, and Cu. By coupling PNCs with plasmonic NPs and elucidating exciton-plasmon interactions, perovskite-based plasmonic and photonic applications can be developed. For example, Fangying et al.[103] used Au nanooctahedrons with a broadband localized surface plasmon resonance (LSPR) peak in a perovskite solar cell device and reported an increased power conversion efficiency from 16.95 to 19.05%. Shi et al.[104] constructed coaxial core/shell PNCs embedded on an Au NP film as a LED with a 155% spontaneous emission rate. Hsieh et al.[105] achieved an ultralow lasing

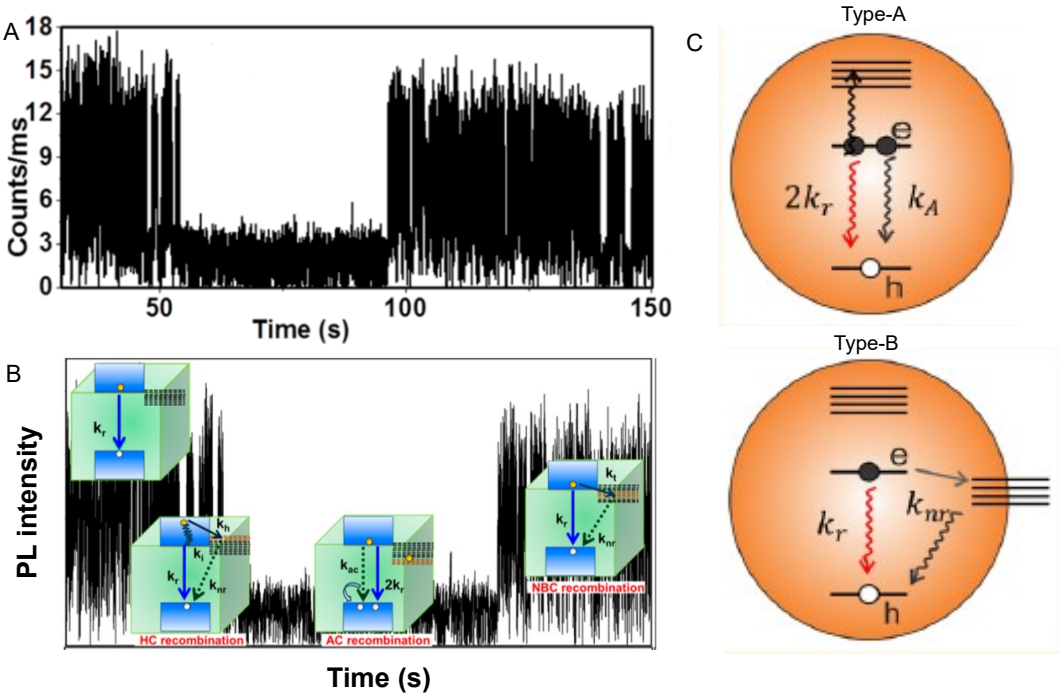

Figure 1.15. (A) A PL intensity trajectory of single $CsPbBr_3$ PNC with different (B) recombination mechanisms. (C) A scheme describing the type-A and type-B blinking mechanisms. Reproduced from (A, B) Ahmed et al.[96] and (C) Mulvaney et al.[117]

threshold (1.9 W cm^{-2}) at 120 K in the Ag nanocube/$CsPbBr_3$ PNC/Al_2O_3/Au system by the plasmonic gap-induced localized Purcell enhancement.

As shown in Figure 1.16A, finite-difference time-domain (FDTD) simulation is widely

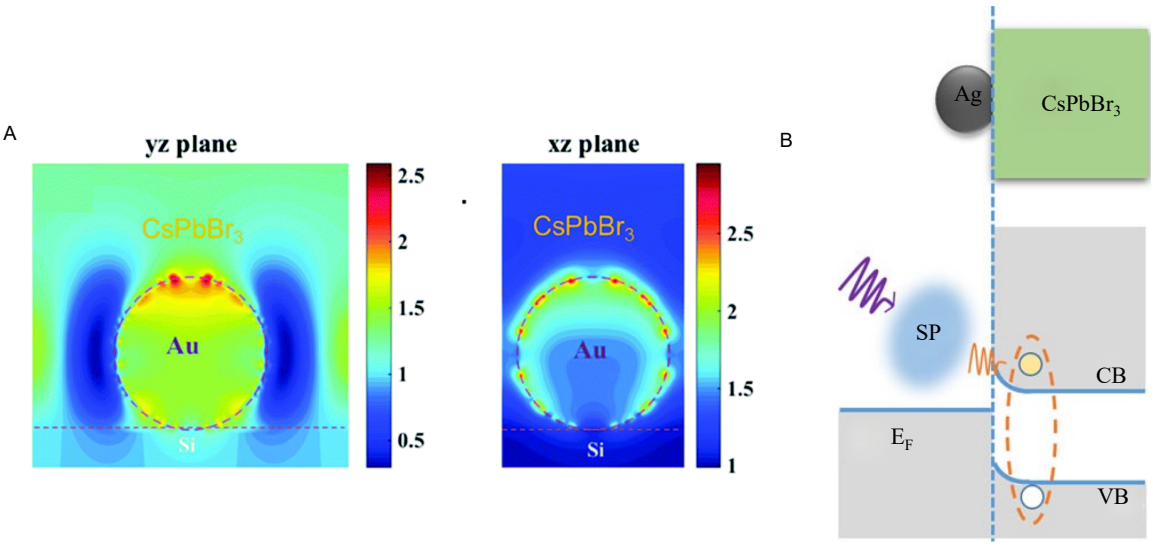

Figure 1.16. (A) Finite-difference time-domain (FDTD) simulation data of plasmon resonance enhancement of the local optical field. (B) A scheme of the plasmon-induced resonant energy transfer process. Reproduced from (A) Dong et al.[101] (B) Huang et al.[102]

used to understand the electric field distribution in metal NPs and 'hot spots' for fluorescent NPs or chromophores coupled with plasmonic NPs. The resonant energy transfer process (Figure 1.16B) gives rise to strong PL enhancement for PNCs coupled with LSPR, which results in an increased radiative decay rate.[106] This fast radiative decay shortens the excited state lifetime of fluorophores. Differences in PL lifetimes and PL intensities can vary from PNC to PNC, depending on the spatial geometry between PNCs and plasmonic cavities.

1.4 Applications of halide perovskites

1.4.1 Solar cells

Due to the excellent photovoltaic properties, such as large absorption cross-sections, wide and tunable bandgap, long-range charge carrier diffusion, and high PL quantum yield, halide perovskites have become an intense research subject for solar cells.[3,6,45] Today, halide perovskites are the most active semiconductor for solar cells. The rapid advances in the perovskite solar cell (PSC) technology are mainly due to their simple solution-processed preparation of high-quality thin films, the direct bandgap nature, high charge carrier mobility, and low Urbach energy. Halide perovskite-based solar cell was first reported by Miyasaka et al. in 2009.[107] They constructed a dye-sensitized solar cell using a hybrid organic-inorganic perovskite layer as the light absorber and reported ca 3.8% power conversion efficiency. This opened up the halide perovskites solar cell field. Although Miyasaka et al. showed the importance of halide perovskite to solar cells, the initial stability and the power conversion efficiency were poor. In 2012 Snaith et al.[108] introduced mesostructured perovskite solar cells made from TiO_2 and spiro-OMeTAD as the n-type and p-type materials, respectively. The fabricated solar cell showed efficiencies as higher as 8% and more interestingly, by replacing the mesoporous TiO_2 with Al_2O_3, they improved the power conversion efficiency to 10.9%. Thus, halide perovskites became the front runners among photovoltaic materials under investigation, lifting the power conversion efficiency to 25% or more.

Generally, the PSC's working principle is based on photoinduced charge generation *via* light absorption. The confinement and harvesting of such charge carriers are challenging. For this purpose, researchers have tested several electrons (ETL) and hole-transporting (HTL) layer materials by sandwiching the perovskite layer between them to extract the charge carriers to the external circuit. Such a PSC device architecture is shown in Figure 1.17A. The selection of an ETL material is based on the LUMO levels of the perovskite and the electron-accepting layer. Also, the HOMO levels of perovskite and the HTL material need careful consideration.

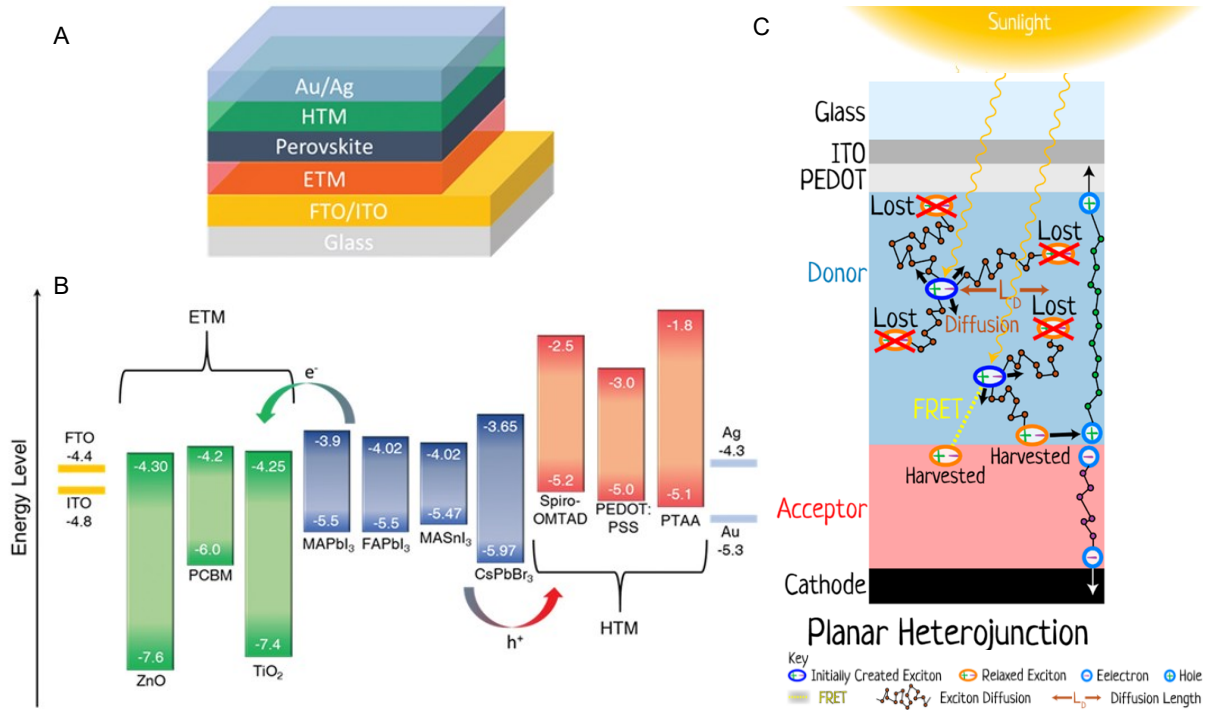

Figure 1.17. (A) A perovskite solar cell structure and (B) energy levels of various ETL, HTL, perovskites, and electrode materials. (C) Carrier diffusion dynamics in PSC. Reproduced from (A, B) Chouhan et al.[3] and (C) Hedley et al.[109]

The most common ETL in PSCs is TCNB, TCNQ, TiO_2, C_{60}, [6,6]-phenyl C_{61} butyric acid methyl ester (PCBM-C_{61}), or PCBM-C_{71}.[23,44]

The HTL materials include poly (3-hexylthiophene) (P3HT) and poly (3,4-ethylene dioxythiophene) polystyrene sulfonate (PEDOT: PSS), and 2,2',7,7'-tetrakis (N,N-di-p-methoxyphenylamine) 9,9'-spirobifluorene (spiro-OMeTAD) are commonly used in solar cells. The energy levels of various HTL, ETL, perovskite, and electrode materials are represented in Figure 1.17B. The HTL and ETL layers facilitate the charge collection from the perovskite layer and improve the charge turnover cycle in the PSCs. However, the fabricated perovskite thin films can agglomerate upon annealing and become thermodynamically unstable, which lowers the interfacial charge separation efficiency. Thus, the solution-processed perovskite thin-film fabrication requires more attention to prepare uniform films and interfacial heterostructures. For example, Snaith et al.[110] demonstrated the importance of film morphology in PSC devices by carefully controlling the solution processing techniques. They show the highest photocurrent attainability and high-power conversion efficiency with the highest perovskite film surface coverages.

Besides the charge separation and morphological issues, precise knowledge of charge carrier diffusion within each layer is crucial for optimizing the PSC efficiency. It is well known

that carrier losses can occur at the interface (Figure 1.17C), such as radiative or non-radiative geminate recombination, non-geminate recombination, and the relaxation of excitons that fail to diffuse to and separate at the interface. Therefore, donor-acceptor heterojunctions and interfaces need further exploration to understand interfacial carrier diffusion and carrier capturing efficiencies. For example, Stranks et al.[111] reported the electron-hole diffusion length exceeding 1 μm for a mixed halide perovskite. They performed transient absorption and PL quenching measurements to calculate the electron-hole diffusion lengths, carrier lifetimes, and the diffusion coefficients for $CH_3NH_3PbI_{3-x}$ Cl_x mixed halide and $CH_3NH_3PbI_3$ perovskites in the PSC devices.

1.4.2 Light-emitting diodes

The LEDs require a narrow and tunable emission material and intrinsically high electroluminescence (EL) quantum yield. These properties commonly observed in halide perovskites make them ideal candidates for LEDs. Recently, perovskite-based LEDs (PeLEDs) are emerging as next-generation displays. PNCs have become superior light emitters in PeLEDs, and the certified efficiency exceeds 20%.[112] However, controlling the size and composition of PNCs, internal and surface defect passivation, doping, and alloying of halide perovskites are necessary to improve the device efficiency. Also, device fabrication needs additional efforts, including external quantum efficiency (EQE) and optimization methods, interfacial engineering, and bandgap engineering. Historically, PeLEDs are fabricated using a perovskite as an active layer, sandwiched between an ETL and an HTL to confine and inject charge carriers. In a typical device, electrons and holes are injected from the anode and cathode through the ETL and HTL into the active layers resulting in inter-band radiative recombination EL emission.

In 2014, Friend et al.[114] fabricated PeLEDs for the first time. They used solution-processed $CH_3NH_3PbI_{3-x}Cl_x$ perovskite and demonstrated the PeLED by tuning the halide composition to generate visible and NIR EL. In this typical device fabrication, a 15 nm layer of perovskite was sandwiched between a TiO_2 and poly(9,9′-dioctylfluorene) layers; 0.76% EQE and 3.4% internal QE were reported. Figure 1.18A demonstrates a PeLED device architecture, and the corresponding EL spectra at different voltages are shown in Figure 1.18B.

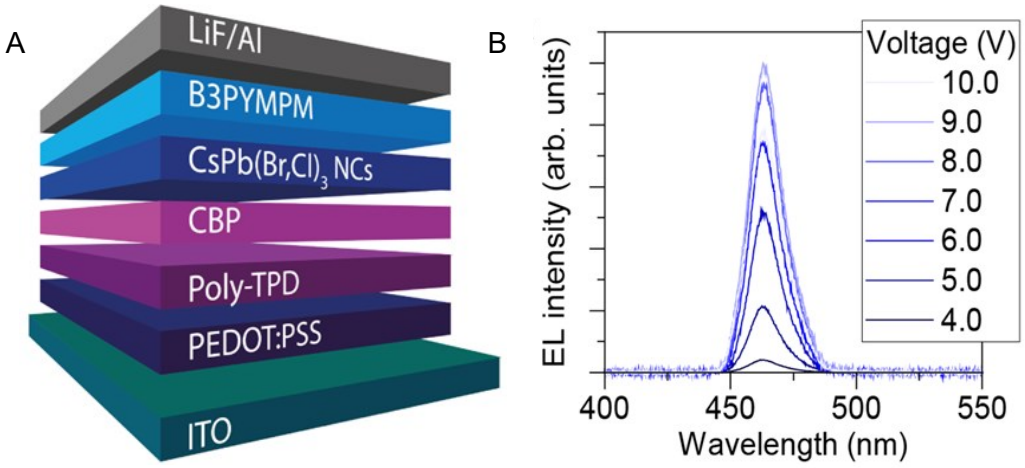

Figure 1.18. (A) A perovskite LED structure and (B) EL spectra of the PeLED at different applied voltages. Reproduced from Ochsenbein et al.[113]

1.4.3 Photodetectors

Along with PSCs and PLEDs, halide perovskites are broadly extended as a light absorber in photodetectors (Figure 1.19).[115,116] Over the years, three different perovskite photodetector (PPD) device architectures have been developed: planar heterojunction, phototransistor, and metal-semiconductor-metal. Generally, the planar heterojunction PPDs are constructed by sandwiching a perovskite layer between an ETL and HTL. For example, Dou et al.[116] constructed a solution-processed PPD using the $CH_3NH_3PbI_{3-x}Cl_x$ hybrid perovskite as an active layer. They demonstrated a device using PEDOT:PSS and PCBM layers, which operate at room temperature. The device showed high efficiency for detecting weak signals as low as 1014 Jones. Also, a linear dynamic range of over 100 decibels, a fast photo response with 3 decibels, and a bandwidth up to 3 MHz were reported for this PPD. Thereafter, PPDs are widely

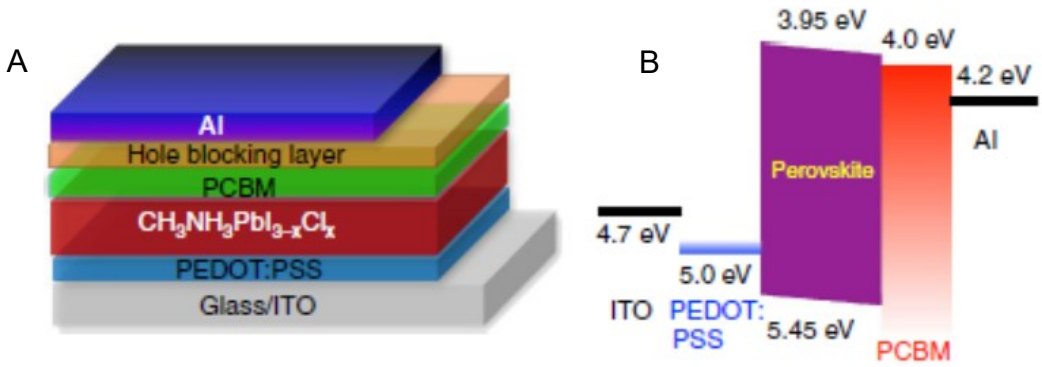

Figure 1.19. (A) A perovskite photodetector structure, and (B) the energy levels of perovskite photodetector under a reverse bias. Reproduced from Dou et al.[116]

investigated because of their prominent outputs, which are better than conventional organic photodetectors. The PPD device interface design and perovskite defect passivation and doping are critical issues, similar to PSCs and PeLEDs. Such a device architecture is represented in Figure 1.19A, along with the energy levels of a PPD under a reverse bias (Figure 1.19B). Metal-semiconductor-metal configuration is another simple PPD device, including a perovskite absorber layer and electrodes. In this case, the photogenerated electrons and holes separate and are transported through the perovskite layer. Such an architecture allows one to investigate the properties of active perovskite layers.

1.5 Research motivation and objectives

The most appealing properties of halide perovskites, including solution processability, tunable emission wavelengths, high photoluminescence quantum yields, and high photostability, made them the current most actively investigated semiconductor materials today. Their outstanding optical properties, low Urbach energy, minimal Stokes shift, high charge carrier mobility, and long carrier diffusion lengths have led to lightning advances in photovoltaic and optoelectronic technologies. While the generation of excitons and their splitting into free charge carriers are very crucial for solar cells, the confinement and harvesting of such charge carriers in perovskite nanocrystal assemblies and single PNC remain largely concealed. The charge carrier diffusion in halide perovskite single crystals and films motivated me to develop closely-packed self-assembled PNC films with electron acceptor heterojunctions and understand the interfacial electron transfer and charge carrier diffusion dynamics. To compare the carrier/exciton lifetime and electron transfer rates of perovskite films with isolated PNCs, I investigated the exciton lifetime and electron transfer dynamics at single-particle levels. Also, to enhance the photoluminescence intensities and improve the excitation-emission cycle in single PNCs, I was motivated to interface PNCs with the surface plasmon resonance of Au nanoparticles.

References

1. Li, X.; Bi, D.; Yi, C.; Décoppet, J. D.; Luo, J.; Zakeeruddin, S. M.; Hagfeldt, A.; Grätzel, M. A Vacuum Flash-Assisted Solution Process for High-Efficiency Large-Area Perovskite Solar Cells. *Science* **2016**, *353*, 58–62.

2. Liu, M.; Johnston, M. B.; Snaith, H. J. Efficient Planar Heterojunction Perovskite Solar Cells by Vapour Deposition. *Nature* **2013**, *501*, 395–398.

3. Chouhan, L.; Ghimire, S.; Subrahmanyam, C.; Miyasaka, T.; Biju, V. Synthesis, Optoelectronic Properties and Applications of Halide Perovskites. *Chem. Soc. Rev.* **2020**, *49*, 2869–2885.

4. Shamsi, J.; Urban, A. S.; Imran, M.; De Trizio, L.; Manna, L. Metal Halide Perovskite Nanocrystals: Synthesis, Post-Synthesis Modifications, and Their Optical Properties. *Chem. Rev.* **2019**, *119*, 3296–3348.

5. Dong, Y.; Zou, Y.; Song, J.; Song, X.; Zeng, H. Recent Progress of Metal Halide Perovskite Photodetectors. *J. Mater. Chem. C* **2017**, *5*, 11369–11394.

6. Zhu, X.; Ge, L.; Wang, Y.; Li, M.; Zhang, R.; Xu, M.; Zhao, Z.; Lv, W.; Chen, R. Recent Advances in Enhancing and Enriching the Optical Properties of Cl-Based $CsPbX_3$ Nanocrystals. *Adv. Opt. Mater.* **2021**.

7. Leng, J.; Liu, J.; Zhang, J.; Jin, S. Decoupling Interfacial Charge Transfer from Bulk Diffusion Unravels Its Intrinsic Role for Efficient Charge Extraction in Perovskite Solar Cells. *J. Phys. Chem. Lett.* **2016**, *7*, 5056–5061.

8. Scheidt, R. A.; Kerns, E.; Kamat, P. V. Interfacial Charge Transfer between Excited $CsPbBr_3$ Nanocrystals and TiO_2: Charge Injection versus Photodegradation. *J. Phys. Chem. Lett.* **2018**, *9*, 5962–5969.

9. Xu, D.; Liu, D.; Xie, T.; Cao, Y.; Wang, J. G.; Ning, Z. J.; Long, Y. T.; Tian, H. Plasmon Resonance Scattering at Perovskite $CH_3NH_3PbI_3$ Coated Single Gold Nanoparticles: Evidence for Electron Transfer. *Chem. Commun.* **2016**, *52*, 9933–9936.

10. Forde, A.; Kilin, D. Hole Transfer in Dye-Sensitized Cesium Lead Halide Perovskite Photovoltaics: Effect of Interfacial Bonding. *J. Phys. Chem. C* **2017**, *121*, 20113–20125.

11. Luo, X.; Liang, G.; Han, Y.; Li, Y.; Ding, T.; He, S.; Liu, X.; Wu, K. Triplet Energy Transfer from Perovskite Nanocrystals Mediated by Electron Transfer. *J. Am. Chem. Soc.* **2020**, *142*, 11270–11278.

12. Sachith, B. M.; Okamoto, T.; Ghimire, S.; Umeyama, T.; Takano, Y.; Imahori, H.; Biju, V. Long-Range Interfacial Charge Carrier Trapping in Halide Perovskite-C_{60} and Halide Perovskite-TiO_2 Donor-Acceptor Films. *J. Phys. Chem. Lett.* **2021**, 12, 8644–8651.

13. Wojciechowski, K.; Stranks, S. D.; Abate, A.; Sadoughi, G.; Sadhanala, A.; Kopidakis, N.; Rumbles, G.; Li, C.; Friend, R. H.; Jen, A. K.; Snaith, H. J. Heterojunction Modi Fi Cation for Highly Solar Cells. *ACS Nano* **2014**, *8*, 12701–12709.

14. Jiang, Q.; Ni, Z.; Xu, G.; Lin, Y.; Rudd, P. N.; Xue, R.; Li, Y.; Li, Y.; Gao, Y.; Huang, J. Interfacial Molecular Doping of Metal Halide Perovskites for Highly Efficient Solar Cells. *Adv. Mater.* **2020**, *32*, 1–10.

15. Jeon, N. J.; Noh, J. H.; Yang, W. S.; Kim, Y. C.; Ryu, S.; Seo, J.; Seok, S. Il. Compositional Engineering of Perovskite Materials for High-Performance Solar Cells. *Nature* **2015**, *517*, 476–480.

16. Brennan, M. C.; Forde, A.; Zhukovskyi, M.; Baublis, A. J.; Morozov, Y. V.; Zhang, S.; Zhang, Z.; Kilin, D. S.; Kuno, M. Universal Size-Dependent Stokes Shifts in Lead Halide Perovskite Nanocrystals. *J. Phys. Chem. Lett.* **2020**, *11*, 4937–4944.

17. Jeong, J.; Kim, M.; Seo, J.; Lu, H.; Ahlawat, P.; Mishra, A.; Yang, Y.; Hope, M. A.; Eickemeyer, F. T.; Kim, M.; Yoon, Y. J.; Choi, I. W.; Darwich, B. P.; Choi, S. J.; Jo,

Y.; Lee, J. H.; Walker, B.; Zakeeruddin, S. M.; Emsley, L.; Rothlisberger, U.; Hagfeldt, A.; Kim, D. S.; Grätzel, M.; Kim, J. Y. Pseudo-Halide Anion Engineering for α-$FAPbI_3$ Perovskite Solar Cells. *Nature* **2021**, *592*, 381–385.

18. Bi, E.; Chen, H.; Xie, F.; Wu, Y.; Chen, W.; Su, Y.; Islam, A.; Grätzel, M.; Yang, X.; Han, L. Diffusion Engineering of Ions and Charge Carriers for Stable Efficient Perovskite Solar Cells. *Nat. Commun.* **2017**, *8*, 15330.

19. Zhumekenov, A. A.; Saidaminov, M. I.; Haque, M. A.; Alarousu, E.; Sarmah, S. P.; Murali, B.; Dursun, I.; Miao, X. H.; Abdelhady, A. L.; Wu, T.; Mohammed, O. F.; Bakr, O. M. Formamidinium Lead Halide Perovskite Crystals with Unprecedented Long Carrier Dynamics and Diffusion Length. *ACS Energy Lett.* **2016**, *1*, 32–37.

20. Mandal, S.; Tkachenko, N. V. Multiphoton Excitation of $CsPbBr_3$ Perovskite Quantum Dots (PQDs): How Many Electrons Can One PQD Donate to Multiple Molecular Acceptors? *J. Phys. Chem. Lett.* **2019**, 2775–2781.

21. Lu, H.; Chen, X.; Anthony, J. E.; Johnson, J. C.; Beard, M. C. Sensitizing Singlet Fission with Perovskite Nanocrystals. *J. Am. Chem. Soc.* **2019**, *141*, 4919–4927.

22. Li, Z.; Wang, R.; Xue, J.; Xing, X.; Yu, C.; Huang, T.; Chu, J.; Wang, K. L.; Dong, C.; Wei, Z.; Zhao, Y.; Wang, Z. K.; Yang, Y. Core-Shell ZnO@SnO_2 Nanoparticles for Efficient Inorganic Perovskite Solar Cells. *J. Am. Chem. Soc.* **2019**, *141*, 17610–17616.

23. Rhee, S.; An, K.; Kang, K. T. Recent Advances and Challenges in Halide Perovskite Crystals in Optoelectronic Devices from Solar Cells to Other Applications. *Crystals* **2021**, *11*, 39.

24. Dey, A. et al. State of the Art and Prospects for Halide Perovskite Nanocrystals. *ACS Nano* **2021**, *15*, 10775–10981.

25. Chen, Y.; Wu, X.; Chu, Y.; Zhou, J.; Zhou, B.; Huang, J. Hybrid Field-Effect Transistors and Photodetectors Based on Organic Semiconductor and $CsPbI_3$ Perovskite Nanorods Bilayer Structure. *Nano-Micro Lett.* **2018**, *10*, 1–9.

26. Xie, C.; Liu, C. K.; Loi, H. L.; Yan, F. Perovskite-Based Phototransistors and Hybrid Photodetectors. *Adv. Funct. Mater.* **2020**, *30*, 1–28.

27. Trinh, C. T.; Minh, D. N.; Ahn, K. J.; Kang, Y.; Lee, K. G. Organic-Inorganic $FAPbBr_3$ Perovskite Quantum Dots as a Quantum Light Source: Single-Photon Emission and Blinking Behaviors. *ACS Photonics* **2018**, *5* (12), 4937–4943.

28. Jeong, J.; Kim, M.; Seo, J.; Lu, H.; Ahlawat, P.; Mishra, A.; Yang, Y.; Hope, M. A.; Eickemeyer, F. T.; Kim, M.; Yoon, Y. J.; Choi, I. W.; Darwich, B. P.; Choi, S. J.; Jo, Y.; Lee, J. H.; Walker, B.; Zakeeruddin, S. M.; Emsley, L.; Rothlisberger, U.; Hagfeldt, A.; Kim, D. S.; Grätzel, M.; Kim, J. Y. Pseudo-Halide Anion Engineering for α-$FAPbI_3$ Perovskite Solar Cells. *Nature* **2021**, *592*, 381–385.

29. Chen, J.; Xiang, H.; Wang, J.; Wang, R.; Li, Y.; Shan, Q.; Xu, X.; Dong, Y.; Wei, C.; Zeng, H. Perovskite White Light Emitting Diodes: Progress, Challenges, and Opportunities. *ACS Nano* **2021**, *15*, 17150–17174.

30. Maity, P.; Dana, J.; Ghosh, H. N. Multiple Charge Transfer Dynamics in Colloidal $CsPbBr_3$ Perovskite Quantum Dots Sensitized Molecular Adsorbate. *J. Phys. Chem. C* **2016**, *120*, 18348–18354.

31. Zhang, J.; Zhu, X.; Wang, M.; Hu, B. Establishing Charge-Transfer Excitons in 2D Perovskite Heterostructures. *Nat. Commun.* **2020**, *11*, 1–8.

32. An, Y.; Hidalgo, J.; Perini, C. A. R.; Castro-Méndez, A.-F.; Vagott, J. N.; Bairley, K.; Wang, S.; Li, X.; Correa-Baena, J.-P. Structural Stability of Formamidinium- and Cesium-Based Halide Perovskites. *ACS Energy Lett.* **2021**, *6*, 1942–1969.

33. Alcocer, M. J. P.; Leijtens, T.; Herz, L. M.; Petrozza, A.; Snaith, H. J. Electron-Hole Diffusion Lengths Exceeding Trihalide Perovskite Absorber. *Science* **2013**, *342*, 341–344.

34. Fan, P.; Gu, D.; Liang, G. X.; Luo, J. T.; Chen, J. L.; Zheng, Z. H.; Zhang, D. P. High-Performance Perovskite $CH_3NH_3PbI_3$ Thin Films for Solar Cells Prepared by Single-Source Physical Vapour Deposition. *Sci. Rep.* **2016**, *6*, 29910.

35. Chen, J.; Park, N. G. Materials and Methods for Interface Engineering toward Stable and Efficient Perovskite Solar Cells. *ACS Energy Lett.* **2020**, *5*, 2742–2786.

36. Jiménez-López, J.; Puscher, B. M. D.; Guldi, D. M.; Palomares, E. Improved Carrier Collection and Hot Electron Extraction across Perovskite, C_{60}, and TiO_2 Interfaces. *J. Am. Chem. Soc.* **2020**, *142*, 1236–1246.

37. Jeon, I.; Ueno, H.; Seo, S.; Aitola, K.; Nishikubo, R.; Saeki, A.; Okada, H.; Boschloo, G.; Maruyama, S.; Matsuo, Y. Lithium-Ion Endohedral Fullerene ($Li^+@C_{60}$) Dopants in Stable Perovskite Solar Cells Induce Instant Doping and Anti-Oxidation. *Angew. Chem. Int. Ed.* **2018**, *57*, 4607–4611.

38. Bishop, J. E.; Smith, J. A.; Lidzey, D. G. Development of Spray-Coated Perovskite Solar Cells. *ACS Appl. Mater. Interfaces* **2020**, *12*, 48237–48245.

39. Zhou, S.; Zhou, G.; Li, Y.; Xu, X.; Hsu, Y. J.; Xu, J.; Zhao, N.; Lu, X. Understanding Charge Transport in All-Inorganic Halide Perovskite Nanocrystal Thin-Film Field Effect Transistors. *ACS Energy Lett.* **2020**, *5*, 2614–2623.

40. Clinckemalie, L.; Valli, D.; Roeffaers, M. B. J.; Hofkens, J.; Pradhan, B.; Debroye, E. Challenges and Opportunities for $CsPbBr_3$ Perovskites in Low- and High-Energy Radiation Detection. *ACS Energy Lett.* **2021**, *6*, 1290–1314.

41. Tian, C.; Wang, F.; Wang, Y.; Yang, Z.; Chen, X.; Mei, J.; Liu, H.; Zhao, D. Chemical Vapor Deposition Method Grown All-Inorganic Perovskite Microcrystals for Self-Powered Photodetectors. *ACS Appl. Mater. Interfaces* **2019**, *11*, 15804–15812.

42. Wang, H.; Rahaq, Y.; Kumar, V. A Composite Light-Harvesting Layer from Photoactive Polymer and Halide Perovskite for Planar Heterojunction Solar Cells. *Sci. Rep.* **2016**, *6*, 29567.

43. Schulz, P. Interface Design for Metal Halide Perovskite Solar Cells. *ACS Energy Lett.* **2018**, *3*, 1287–1293.

44. Protesescu, L.; Yakunin, S.; Bodnarchuk, M. I.; Krieg, F.; Caputo, R.; Hendon, C. H.; Yang, R. X.; Walsh, A.; Kovalenko, M. V. Nanocrystals of Cesium Lead Halide Perovskites ($CsPbX_3$, X = Cl, Br, and I): Novel Optoelectronic Materials Showing Bright Emission with Wide Color Gamut. *Nano Lett.* **2015**, *15*, 3692–3696.

45. Lignos, I.; Stavrakis, S.; Nedelcu, G.; Protesescu, L.; Demello, A. J.; Kovalenko, M. V. Synthesis of Cesium Lead Halide Perovskite Nanocrystals in a Droplet-Based Microfluidic Platform: Fast Parametric Space Mapping. *Nano Lett.* **2016**, *16*, 1869–1877.

46. Udayabhaskararao, T.; Kazes, M.; Houben, L.; Lin, H.; Oron, D. Nucleation, Growth, and Structural Transformations of Perovskite Nanocrystals. *Chem. Mater.* **2017**, *29*, 1302–1308.

47. Kovalenko, M. V.; Protesescu, L.; Bodnarchuk, M. I. Properties and Potential Optoelectronic Applications of Lead Halide Perovskite Nanocrystals. *Science* **2017**, *358*, 745–750.

48. Zhang, F.; Zhong, H.; Chen, C.; Wu, X. G.; Hu, X.; Huang, H.; Han, J.; Zou, B.; Dong, Y. Brightly Luminescent and Color-Tunable Colloidal $CH_3NH_3PbX_3$ (X = Br, I, Cl) Quantum Dots: Potential Alternatives for Display Technology. *ACS Nano* **2015**, *9*, 4533–4542.

49. Pushkarev, A. P.; Korolev, V. I.; Markina, D. I.; Komissarenko, F. E.; Naujokaitis, A.; Drabavičius, A.; Pakštas, V.; Franckevičius, M.; Khubezhov, S. A.; Sannikov, D. A.; Zasedatelev, A. V.; Lagoudakis, P. G.; Zakhidov, A. A.; Makarov, S. V. A Few-Minute Synthesis of $CsPbBr_3$ Nanolasers with a High-Quality Factor by Spraying at Ambient Conditions. *ACS Appl. Mater. Interfaces* **2019**, *11*, 1040–1048.

50. Litvin, A. P.; Zhang, X.; Berwick, K.; Fedorov, A. V.; Zheng, W.; Baranov, A. V. Carbon-Based Interlayers in Perovskite Solar Cells. *Renew. Sustain. Energy Rev.* **2020**, *124*, 109774.

51. Gil-Escrig, L.; Dreessen, C.; Palazon, F.; Hawash, Z.; Moons, E.; Albrecht, S.; Sessolo, M.; Bolink, H. J. Efficient Wide-Bandgap Mixed-Cation and Mixed-Halide Perovskite Solar Cells by Vacuum Deposition. *ACS Energy Lett.* **2021**, *6*, 827–836.

52. Li, Y.; Wu, F.; Han, M.; Li, Z.; Zhu, L.; Li, Z. Merocyanine with Hole-Transporting Ability and Efficient Defect Passivation Effect for Perovskite Solar Cells. *ACS Energy Lett.* **2021**, *6*, 869–876.

53. Guo, Z.; Manser, J. S.; Wan, Y.; Kamat, P. V.; Huang, L. Spatial and Temporal Imaging of Long-Range Charge Transport in Perovskite Thin Films by Ultrafast Microscopy. *Nat. Commun.* **2015**, *6*, 7471.

54. Ghimire, S.; Nair, V. C.; Muthu, C.; Yuyama, K.; Vacha, M.; Biju, V. Photoinduced Photoluminescence Enhancement in Self-Assembled Clusters of Formamidinium Lead Bromide Perovskite Nanocrystals. *Nanoscale* **2019**, *11*, 9335–9340.

55. He, H.; Yu, Q.; Li, H.; Li, J.; Si, J.; Jin, Y.; Wang, N.; Wang, J.; He, J.; Wang, X.; Zhang, Y.; Ye, Z. Exciton Localization in Solution-Processed Organolead Trihalide Perovskites. *Nat. Commun.* **2016**, *7*, 10896.

56. Miyata, A.; Mitioglu, A.; Plochocka, P.; Portugall, O.; Wang, J. T. W.; Stranks, S. D.; Snaith, H. J.; Nicholas, R. J. Direct Measurement of the Exciton Binding Energy and Effective Masses for Charge Carriers in Organic-Inorganic Tri-Halide Perovskites. *Nat. Phys.* **2015**, *11*, 582–587.

57. Pradeep, K. R.; Acharya, D.; Jain, P.; Gahlot, K.; Yadav, A.; Camellini, A.; Zavelani-Rossi, M.; Cerullo, G.; Narayana, C.; Narasimhan, S.; Viswanatha, R. Harvesting Delayed Fluorescence in Perovskite Nanocrystals Using Spin-Forbidden Mn d States. *ACS Energy Lett.* **2020**, 353–359.

58. Zhai, Y.; Wang, K.; Zhang, F.; Xiao, C.; Rose, A. H.; Zhu, K.; Beard, M. C. Individual Electron and Hole Mobilities in Lead-Halide Perovskites Revealed by Noncontact Methods. *ACS Energy Lett.* **2020**, *5*, 47–55.

59. Qiao, T.; Son, D. H. Synthesis and Properties of Strongly Quantum-Confined Cesium Lead Halide Perovskite Nanocrystals. *Acc. Chem. Res.* **2021**, *54*, 1399–1408.

60. Bhatia, H.; Steele, J. A.; Martin, C.; Keshavarz, M.; Solis-Fernandez, G.; Yuan, H.; Fleury, G.; Huang, H.; Dovgaliuk, I.; Chernyshov, D.; Hendrix, J.; Roeffaers, M. B. J.; Hofkens, J.; Debroye, E. Single-Step Synthesis of Dual Phase Bright Blue-Green Emitting Lead Halide Perovskite Nanocrystal Thin Films. *Chem. Mater.* **2019**, *31*, 6824–6832.

61. Caselli, V. M.; Wei, Z.; Ackermans, M. M.; Hutter, E. M.; Ehrler, B.; Savenije, T. J. Charge Carrier Dynamics upon Sub-Bandgap Excitation in Methylammonium Lead Iodide Thin Films: Effects of Urbach Tail, Deep Defects, and Two-Photon Absorption. *ACS Energy Lett.* **2020**, *5*, 3821–3827.

62. Ledinsky, M.; Schönfeldová, T.; Holovský, J.; Aydin, E.; Hájková, Z.; Landová, L.; Neyková, N.; Fejfar, A.; De Wolf, S. Temperature Dependence of the Urbach Energy in Lead Iodide Perovskites. *J. Phys. Chem. Lett.* **2019**, *10*, 1368–1373.

63. Shi, D.; Adinolfi, V.; Comin, R.; Yuan, M.; Alarousu, E.; Buin, A.; Chen, Y.; Hoogland, S.; Rothenberger, A.; Katsiev, K.; Losovyj, Y.; Zhang, X.; Dowben, P. A.; Mohammed, O. F.; Sargent, E. H.; Bakr, O. M. Low Trap-State Density and Long Carrier Diffusion in Organolead Trihalide Perovskite Single Crystals. *Science* **2015**, *347*, 519–522.

64. Dang, Z.; Shamsi, J.; Palazon, F.; Imran, M.; Akkerman, Q. A.; Park, S.; Bertoni, G.; Prato, M.; Brescia, R.; Manna, L. In Situ Transmission Electron Microscopy Study of Electron Beam-Induced Transformations in Colloidal Cesium Lead Halide Perovskite Nanocrystals. *ACS Nano* **2017**, *11*, 2124–2132.

65. Wang, S.; Yu, J.; Zhang, M.; Chen, D.; Li, C.; Chen, R.; Jia, G.; Rogach, A. L.; Yang, X. Stable, Strongly Emitting Cesium Lead Bromide Perovskite Nanorods with High Optical Gain Enabled by an Intermediate Monomer Reservoir Synthetic Strategy. *Nano Lett.* **2019**, *19*, 6315–6322.

66. Shamsi, J.; Dang, Z.; Bianchini, P.; Canale, C.; Stasio, F. Di; Brescia, R.; Prato, M.; Manna, L. Colloidal Synthesis of Quantum Confined Single Crystal $CsPbBr_3$ Nanosheets with Lateral Size Control up to the Micrometer Range. *J. Am. Chem. Soc.* **2016**, *138*, 7240–7243.

67. Heo, J. H.; Lee, M. H.; Jang, M. H.; Im, S. H. Highly Efficient $CH_3NH_3PbI_{3-x}Cl_x$ Mixed Halide Perovskite Solar Cells Prepared by Re-Dissolution and Crystal Grain Growth via Spray Coating. *J. Mater. Chem. A* **2016**, *4*, 17636–17642.

68. Jang, D. M.; Park, K.; Kim, D. H.; Park, J.; Shojaei, F.; Kang, H. S.; Ahn, J. P.; Lee, J. W.; Song, J. K. Reversible Halide Exchange Reaction of Organometal Trihalide Perovskite Colloidal Nanocrystals for Full-Range Band Gap Tuning. *Nano Lett.* **2015**, *15*, 5191–5199.

69. Carretero-Palacios, S.; Calvo, M. E.; Míguez, H. Absorption Enhancement in Organic-Inorganic Halide Perovskite Films with Embedded Plasmonic Gold Nanoparticles. *J. Phys. Chem. C* **2015**, *119*, 18635–18640.

70. Wu, S. H.; Lin, M. Y.; Chang, S. H.; Tu, W. C.; Chu, C. W.; Chang, Y. C. A Design Based on a Charge-Transfer Bilayer as an Electron Transport Layer for Improving the Performance and Stability in Planar Perovskite Solar Cells. *J. Phys. Chem. C* **2018**, *122*, 236–244.

71. Wu, K.; Liang, G.; Shang, Q.; Ren, Y.; Kong, D.; Lian, T. Ultrafast Interfacial Electron and Hole Transfer from $CsPbBr_3$ Perovskite Quantum Dots. *J. Am. Chem. Soc.* **2015**, *137*, 12792–12795.

72. Yang, D.; Zhang, X.; Wang, K.; Wu, C.; Yang, R.; Hou, Y.; Jiang, Y.; Liu, S.; Priya, S. Stable Efficiency Exceeding 20.6% for Inverted Perovskite Solar Cells through Polymer-Optimized PCBM Electron-Transport Layers. *Nano Lett.* **2019**, *19*, 3313–3320.

73. Chueh, C. C.; Li, C. Z.; Jen, A. K. Y. Recent Progress and Perspective in Solution-Processed Interfacial Materials for Efficient and Stable Polymer and Organometal Perovskite Solar Cells. *Energy Environ. Sci.* **2015**, *8*, 1160–1189.

74. Nedelcu, G.; Protesescu, L.; Yakunin, S.; Bodnarchuk, M. I.; Grotevent, M. J.; Kovalenko, M. V. Fast Anion-Exchange in Highly Luminescent Nanocrystals of Cesium Lead Halide Perovskites ($CsPbX_3$, X = Cl, Br, I). *Nano Lett.* **2015**, *15*, 5635–5640.

75. Van der Stam, W.; Geuchies, J. J.; Altantzis, T.; Van Den Bos, K. H. W.; Meeldijk, J. D.; Van Aert, S.; Bals, S.; Vanmaekelbergh, D.; De Mello Donega, C. Highly Emissive Divalent-Ion-Doped Colloidal $CsPb_{1-X}M_xBr_3$ Perovskite Nanocrystals through Cation Exchange. *J. Am. Chem. Soc.* **2017**, *139*, 4087–4097.

76. Nair, V. C.; Muthu, C.; Rogach, A. L.; Kohara, R.; Biju, V. Channeling Exciton Migration into Electron Transfer in Formamidinium Lead Bromide Perovskite Nanocrystal/Fullerene Composites. *Angew. Chem. Int. Ed.* **2017**, *56*, 1214–1218.

77. Tong, Y. L.; Zhang, Y. W.; Ma, K.; Cheng, R.; Wang, F.; Chen, S. One-Step Synthesis of FA-Directing $FAPbBr_3$ Perovskite Nanocrystals toward High-Performance Display. *ACS Appl. Mater. Interfaces* **2018**, *10*, 31603–31609.

78. Golubev, T.; Liu, D.; Lunt, R.; Duxbury, P. Understanding the Impact of C_{60} at the Interface of Perovskite Solar Cells via Drift-Diffusion Modeling. *AIP Adv.* **2019**, *9*, 035026.

79. Credgington, D.; Jamieson, F. C.; Walker, B.; Nguyen, T. Q.; Durrant, J. R. Quantification of Geminate and Non-Geminate Recombination Losses within a Solution-Processed Small-Molecule Bulk Heterojunction Solar Cell. *Adv. Mater.* **2012**, *24*, 2135–2141.

80. Ye, J.; Byranvand, M. M.; Martínez, C. O.; Hoye, R. L. Z.; Saliba, M.; Polavarapu, L. Defect Passivation in Lead-Halide Perovskite Nanocrystals and Thin Films: Toward Efficient LEDs and Solar Cells. *Angew. Chem. Int. Ed.* **2021**, *60*, 21636–21660.

81. Lee, S. W.; Kim, S.; Bae, S.; Cho, K.; Chung, T.; Mundt, L. E.; Lee, S.; Park, S.; Park, H.; Schubert, M. C.; Glunz, S. W.; Ko, Y.; Jun, Y.; Kang, Y.; Lee, H. S.; Kim, D. UV Degradation and Recovery of Perovskite Solar Cells. *Sci. Rep.* **2016**, *6*, 38150.

82. Deng, Y.; Peng, E.; Shao, Y.; Xiao, Z.; Dong, Q.; Huang, J. Scalable Fabrication of Efficient Organolead Trihalide Perovskite Solar Cells with Doctor-Bladed Active Layers. *Energy Environ. Sci.* **2015**, *8*, 1544–1550.

83. Hendrik, U et al. Coherent Single-Photon Emission from Colloidal Lead Halide Perovskite Quantum Dots. *Science* **2019**, *363*, 1068–1072.

84. Sherkar, T. S.; Momblona, C.; Gil-Escrig, L.; Ávila, J.; Sessolo, M.; Bolink, H. J.; Koster, L. J. A. Recombination in Perovskite Solar Cells: Significance of Grain Boundaries, Interface Traps, and Defect Ions. *ACS Energy Lett.* **2017**, *2*, 1214–1222.

85. Wojciechowski, K.; Leijtens, T.; Siprova, S.; Schlueter, C.; Hörantner, M. T.; Wang, J. T. W.; Li, C. Z.; Jen, A. K. Y.; Lee, T. L.; Snaith, H. J. C_{60} as an Efficient N-Type Compact Layer in Perovskite Solar Cells. *J. Phys. Chem. Lett.* **2015**, *6*, 2399–2405.

86. Long, R.; Fang, W. H.; Prezhdo, O. V. Strong Interaction at the Perovskite/TiO_2 Interface Facilitates Ultrafast Photoinduced Charge Separation: A Nonadiabatic Molecular Dynamics Study. *J. Phys. Chem. C* **2017**, *121*, 3797–3806.

87. Chen, C.; Jiang, Y.; Guo, J.; Wu, X.; Zhang, W.; Wu, S.; Gao, X.; Hu, X.; Wang, Q.; Zhou, G.; Chen, Y.; Liu, J. M.; Kempa, K.; Gao, J. Solvent-Assisted Low-Temperature Crystallization of SnO_2 Electron-Transfer Layer for High-Efficiency Planar Perovskite Solar Cells. *Adv. Funct. Mater.* **2019**, *29*, 1–9.

88. Xu, C.; Zhang, Y.; Luo, P.; Sun, J.; Wang, H.; Lu, Y. W.; Ding, F.; Zhang, C.; Hu, J. Comparative Study on TiO_2 and C_{60} Electron Transport Layers for Efficient Perovskite Solar Cells. *ACS Appl. Energy Mater.* **2021**, *4*, 5543–5553.

89. Zhang, L.; Reddy, M. A.; Gao, P.; Diemant, T.; Jürgen Behm, R.; Fichtner, M. Study of All Solid-State Rechargeable Fluoride Ion Batteries based on Thin-Film Electrolyte. *J. Solid State Electrochem.* **2017**, *21*, 1243–1251.

90. Bera, S.; Pradhan, N. Perovskite Nanocrystal Heterostructures: Synthesis, Optical Properties, and Applications. *ACS Energy Lett.* **2020**, *5*, 2858–2872.

91. Manser, J. S.; Christians, J. A.; Kamat, P. V. Intriguing Optoelectronic Properties of Metal Halide Perovskites. *Chem. Rev.* **2016**, *116*, 12956–13008.

92. Alcocer, M. J. P.; Leijtens, T.; Herz, L. M.; Petrozza, A.; Snaith, H. J. Electron-Hole Diffusion Lengths Exceeding Trihalide Perovskite Absorber. *Science.* **2013**, *342*, 341–344.

93. Chen, X.; Lu, H.; Li, Z.; Zhai, Y.; Ndione, P. F.; Berry, J. J.; Zhu, K.; Yang, Y.; Beard, M. C. Impact of Layer Thickness on the Charge Carrier and Spin Coherence Lifetime in Two-Dimensional Layered Perovskite Single Crystals. *ACS Energy Lett.* **2018**, *3*, 2273–2279.

94. Stavrakas, C.; Delport, G.; Zhumekenov, A. A.; Anaya, M.; Chahbazian, R.; Bakr, O. M.; Barnard, E. S.; Stranks, S. D. Visualizing Buried Local Carrier Diffusion in Halide Perovskite Crystals via Two-Photon Microscopy. *ACS Energy Lett.* **2020**, *5*, 117–123.

95. Crothers, T. W.; Milot, R. L.; Patel, J. B.; Parrott, E. S.; Schlipf, J.; Müller-Buschbaum, P.; Johnston, M. B.; Herz, L. M. Photon Reabsorption Masks Intrinsic Bimolecular Charge-Carrier Recombination in $CH_3NH_3PbI_3$ Perovskite. *Nano Lett.* **2017**, *17*, 5782–5789.

96. Ahmed, T.; Seth, S.; Samanta, A. Mechanistic Investigation of the Defect Activity Contributing to the Photoluminescence Blinking of $CsPbBr_3$ Perovskite Nanocrystals. *ACS Nano* **2019,** *13*, 13537-13544.

97. Yuan, H.; Debroye, E.; Bladt, E.; Lu, G.; Keshavarz, M.; Janssen, K. P. F.; Roeffaers, M. B. J.; Bals, S.; Sargent, E. H.; Hofkens, J. Imaging Heterogeneously Distributed Photo-Active Traps in Perovskite Single Crystals. *Adv. Mater.* **2018**, *30*, 1–9.

98. Galland, C.; Ghosh, Y.; Steinbrück, A.; Sykora, M.; Hollingsworth, J. A.; Klimov, V. I.; Htoon, H. Two Types of Luminescence Blinking Revealed by Spectroelectrochemistry of Single Quantum Dots. *Nature* **2011**, *479*, 203–207.

99. Chouhan, L.; Ito, S.; Thomas, E. M.; Takano, Y.; Ghimire, S.; Miyasaka, H.; Biju, V. Real-Time Blinking Suppression of Perovskite Quantum Dots by Halide Vacancy Filling. *ACS Nano* **2021**, *15*, 2831–2838.

100. Rainoì, G.; Nedelcu, G.; Protesescu, L.; Bodnarchuk, M. I.; Kovalenko, M. V.; Mahrt, R. F.; Stöferle, T. Single Cesium Lead Halide Perovskite Nanocrystals at Low Temperature: Fast Single-Photon Emission, Reduced Blinking, and Exciton Fine Structure. *ACS Nano* **2016**, *10*, 2485–2490.

101. Dong, Y.; Zou, Y.; Song, J.; Song, X.; Zeng, H. Recent Progress of Metal Halide Perovskite Photodetectors. *J. Mater. Chem. C* **2017**, *5*, 11369–11394.

102. Huang, X.; Li, H.; Zhang, C.; Tan, S.; Chen, Z.; Chen, L.; Lu, Z.; Wang, X.; Xiao, M. Efficient Plasmon-Hot Electron Conversion in Ag–$CsPbBr_3$ Hybrid Nanocrystals. *Nat. Commun.* **2019**, *10*, 1–8.

103. Juan, F. *et al.* Plasmonic Au Nanooctahedrons Enhance Light Harvesting and Photocarrier Extraction in Perovskite Solar Cell. *ACS Appl. Energy Mater* **2021,** *4*, 3201–3209.

104. Shi, Z. *et al.* Localized Surface Plasmon Enhanced All-Inorganic Perovskite Quantum Dot Light-Emitting Diodes Based on Coaxial Core/Shell Heterojunction Architecture. *Adv. Funct. Mater.* **2018**, *28*, 1–11.

105. Hsieh, Y. H. *et al.* Perovskite Quantum Dot Lasing in a Gap-Plasmon Nanocavity with Ultralow Threshold. *ACS Nano* **2020**, *14*, 11670–11676.

106. Fu, Y., Zhang, J. & Lakowicz, J. R. Silver-Enhanced Fluorescence Emission of Single Quantum Dot Nanocomposites. *Chem. Commun.* **2009***,* 313–315.

107. Kojima, A.; Teshima, K.; Shirai, Y.; Miyasaka, T. Organometal Halide Perovskites as Visible-Light Sensitizers for Photovoltaic Cells. *J. Am. Chem. Soc.* **2009**, *131*, 6050–6051.

108. Micheal, L.; Joel, T.; Tsutomu, M.; Takurou, N. M.; Henry, J. S. Efficient Hybrid Solar Cells based on Meso-Superstructured Organometal Halide Perovskites. *Science* **2012**, *338*, 643–647.

109. Hedley, G. J.; Ruseckas, A.; Samuel, I. D. W. Light Harvesting for Organic Photovoltaics. *Chem. Rev.* **2017**, *117*, 796–837.

110. Eperon, G. E.; Burlakov, V. M.; Docampo, P.; Goriely, A.; Snaith, H. J. Morphological Control for High Performance, Solution-Processed Planar Heterojunction Perovskite Solar Cells. *Adv. Funct. Mater.* **2014**, *24*, 151–157.

111. Samuel, D. S.; Giles, E. E.; Giulia, G.; Christopher, M.; Marcelo, J. P A.; Tomas, L.; Laura, M. H.; Annamaria, P.; Henry, J. S. Electron-Hole Diffusion Lengths Exceeding 1 Micrometer in an Organometal Trihalide Perovskite Absorber. *Science* **2013**, *342*, 341–344.

112. Wei, Z.; Xing, J. The Rise of Perovskite Light-Emitting Diodes. *J. Phys. Chem. Lett.* **2019**, *10*, 3035–3042.

113. Ochsenbein, S. T.; Krieg, F.; Shynkarenko, Y.; Rainò, G.; Kovalenko, M. V. Engineering Color-Stable Blue Light-Emitting Diodes with Lead Halide Perovskite Nanocrystals. *ACS Appl. Mater. Interfaces* **2019**, *11*, 21655–21660.

114. Tan, Z. K.; Moghaddam, R. S.; Lai, M. L.; Docampo, P.; Higler, R.; Deschler, F.; Price, M.; Sadhanala, A.; Pazos, L. M.; Credgington, D.; Hanusch, F.; Bein, T.; Snaith, H. J.; Friend, R. H. Bright Light-Emitting Diodes Based on Organometal Halide Perovskite. *Nat. Nanotechnol.* **2014**, *9*, 687–692.

115. Li, C.; Ma, Y.; Xiao, Y.; Shen, L.; Ding, L. Advances in Perovskite Photodetectors. *InfoMat* **2020**, *2*, 1247–1256.

116. Dou, L.; Yang, Y. M.; You, J.; Hong, Z.; Chang, W. H.; Li, G.; Yang, Y. Solution-Processed Hybrid Perovskite Photodetectors with High Detectivity. *Nat. Commun.* **2014**, *5,* 1-6.

117. Yuan, G.; Gómez, D. E.; Kirkwood, N.; Boldt, K.; Mulvaney, P. Two Mechanisms Determine Quantum Dot Blinking. *ACS Nano* **2018**, *12*, 3397–3405.

Chapter 2
Experimental

This chapter details the materials, samples, distinct experimental procedures, and instrumentation techniques in this thesis. A brief overview of the chemicals and materials is followed by the perovskite nanocrystal synthesis and their characterization. I employed hot injection, ligand-assisted reprecipitation, and modified spray techniques to synthesize $CsPbBr_3$, $MAPbBr_3$, and $FAPbBr_3$ nanocrystals. These methods provided narrow and uniform size distributed perovskite nanocrystals. The synthesized perovskite nanocrystals dispersed in toluene were processed into single-particle samples or thin films by drop-casting, spin-coating, or spray techniques. Au nanoparticle films were prepared by sputter-coating. The scanning transmission electron microscopy, scanning electron microscopy, and a focused ion beam system was used to characterize the perovskite and Au nanoparticle sizes and perovskite film thicknesses. The steady-state UV-vis absorption spectroscopy was utilized to characterize the excitonic bands of the synthesized perovskite nanocrystals. The emission features were studied using steady-state and time-resolved techniques. The structural properties were analyzed by scanning transition electron microscopy. I used a single particle fluorescence microspectroscopy system with an EMCCD to understand the single-particle level exciton plasmon coupling and electron transfer. The exciton relaxation, plasmon coupling, and electron transfer dynamics of perovskite films were further analyzed using transient absorption spectroscopy.

2.1. Materials

The following chemicals and materials were used as received for the experiments; halide salts [CsBr (>98%), MABr (CH_3NH_3Br, >98%), FABr (>98%), and $PbBr_2$ (≥98%)] and oleic acid (>85%), and γ-butyrolactone (GBL, >99%) were from the Tokyo Chemical Industry. Hexadecyl amine (HDA, >95%), 1-hexadecene (>95%), 1-octadecene, dehydrated toluene (spectroscopic grade), dehydrated hexane (>99%), acetone, n-butanol (99%), and dehydrated *N,N*-dimethyl formamide (DMF, spectroscopic grade) were from the FUJI-film Wako Pure Chemicals, Japan. Cover glasses (24 mm x 50 mm or 18 mm x 18 mm, thickness 0.13-0.17 mm) were from Matsunami. Fullerene (C_{60}), TiO_2, and cesium acetate were from Sigma-Aldrich, Japan.

2.2. Methods

2.2.1. Synthesis of lead halide perovskite nanocrystals

Ligand-assisted reprecipitation method (LARP)

Synthesis of $MAPbBr_3$ PNCs

The $MAPbBr_3$ PNCs were synthesized by the LARP method.[1,2] The precursor mixture was prepared by dissolving MABr (0.25 mmol), $PbBr_2$ (0.27 mmol), hexadecyl amine (HDA, 0.19 mmol), and oleic acid (80 µl) in dry *N,N*-dimethyl formamide (DMF, 1 mL) by continuous stirring at 80 ºC (Figure 2.1). The clear reaction mixture was later injected into a vigorously stirring toluene (50 ml). The reaction mixture turned green, gradually precipitated, and turned into an orange-yellow turbid solution during vigorous stirring for 15 min. The precipitated PNCs were centrifuged at 12,000 rpm for 5 min, and the clear supernatant was discarded. To remove excess ligands, the residue was re-dispersed in toluene and washed with n-butanol.

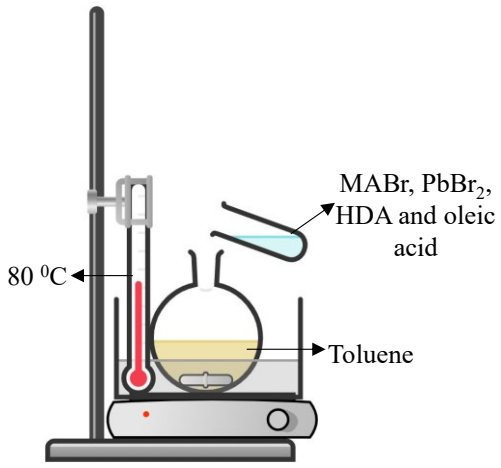

Figure 2.1. A scheme of $MAPbBr_3$ PNC synthesis by the LARP method.

Synthesis of $FAPbBr_3$ PNCs

A modified LARP technique was employed to synthesize the $FAPbBr_3$ PNCs.[3,4] At first, the ligand mixture, including oleic acid and octylammonium bromide, was dissolved in 1-octadecene at 80 °C under constant stirring. Similarly, the precursor mixture (FABr and $PbBr_2$) was dissolved in dry *N,N*-dimethyl formamide. Precursors, ligands, and solvents in the synthesis are summarized in Table 2.1. Later, the clear precursor solution was injected (Figure 2.2) into the vigorously stirring ligand mixture at 80 °C, and immediately, the reaction mixture turned into a bright orange solution. Precipitation of PNCs was carried out by adding the acetone-hexane mixture of a 1:2 ratio. The excess precursors and ligands in the above reaction mixture were separated by centrifuging at 10000 rpm for 3 min. The purified PNCs were dispersed in toluene and centrifuged at 4000 rpm, and the supernatant was stored for further studies.

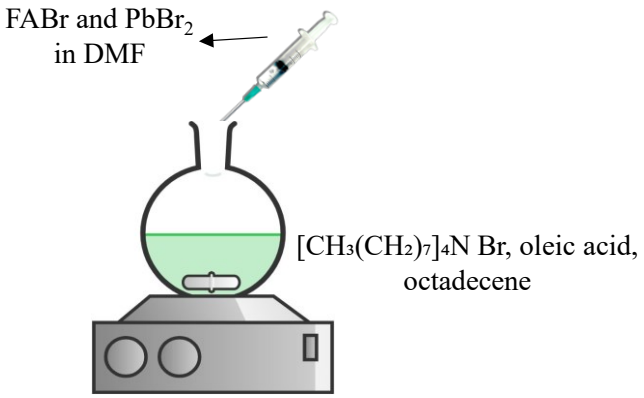

Figure 2.2. A scheme of $FAPbBr_3$ PNC synthesis by the LARP method.

Table 2.1 The amounts of precursors in the LARP synthesis of $MAPbBr_3$ and $FAPbBr_3$ PNCs

Samples	Precursors	mmol (mg)
$MAPbBr_3$	MABr	0.25 (28.2)
	$PbBr_2$	0.27 (100)
	HDA	0.19 (46)
$FAPbBr_3$	FABr	1 (100)
	$PbBr_2$	1 (367)
	Octylammonium bromide	0.6 (126)

Hot-injection techniques

Synthesis of $CsPbBr_3$ PNCs

A traditional hot-injection method was used to synthesize $CsPbBr_3$ PNCs.[5-8] All the precursors were dried under vacuum at 120 °C in two separate round bottom flasks. The first flask contained lead bromide, oleic acid, and hexadecyl amine dissolved in 1-hexadecene. A cesium oleate solution was prepared in another flask by reacting cesium acetate with oleic acid at 120 °C. The amounts of precursors in the synthesis are indicated in Table 2.2. While drying under vacuum, argon was flushed alternately every 15 min for 1 hr. The temperature of the first flask was raised to 170 °C under an argon atmosphere after the complete dissolution of the salts. Later, the prepared cesium oleate was injected into the above hot solution at 170 °C (Figure 2.3).

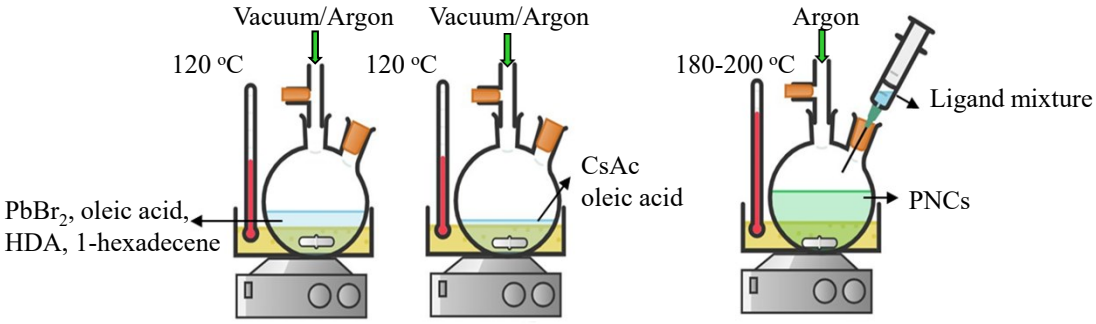

Figure 2.3. A scheme of $CsPbBr_3$ PNC synthesis by the hot-injection technique.

Immediately, the reaction mixture turned into a green-colored solution, and it was placed in an ice-water bath. The precipitated PNCs were washed using hexane and centrifuged at 12000 rpm for 3 min. The obtained residue was re-dispersed in toluene and stored for further studies.

Table 2.2 Amounts of precursors in the hot-injection synthesis of $CsPbBr_3$ PNCs.

Samples	Precursors	mmol (mg)
$CsPbBr_3$	CsAc	0.15 (28.8)
	$PbBr_2$	0.56 (207)
	HDA	4.56 (1101)

Modified spray techniques

Synthesis of $MAPbBr_3$ PNCs without ligands

To avoid the ligand-induced agglomeration of single PNCs, I prepared $MAPbBr_3$ PNCs without ligands (W-PNCs) using a modified spray technique.[9] MABr (0.5 M) and $PbBr_2$ (0.5 M) were dissolved in DMF (1 mL) to form a precursor complex. This complex solution was later poured into a glass vial with a spray cap (5 mL) containing γ-butyrolactone (GBL, 1:1, v/v ratio). This suspension was sprayed onto a substrate or an Au-coated glass under the ambient atmosphere (Figure 2.4). To reduce the size of the droplets, the distance between the spray bottle and the substrate was maintained at ~ 10 to 15 cm. The crystallization took place in seconds with a uniform size distribution of PNCs.

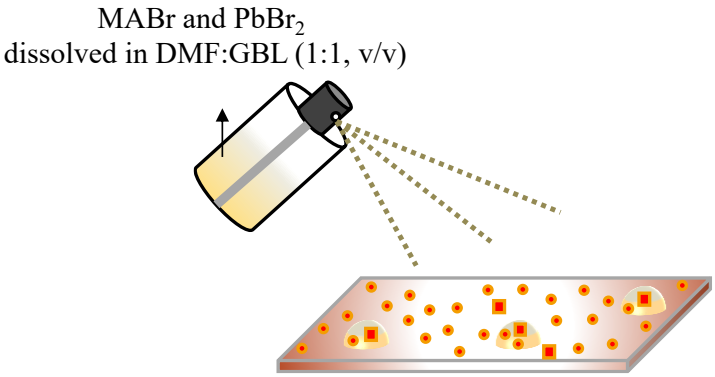

Figure 2.4. A scheme of $MAPbBr_3$ PNC synthesis by the spray technique.

2.2.2. Preparation of nanocrystal thin films

I used a spin-coating technique to prepare the PNCs thin film.[10,11] A scheme of PNCs film preparation by a spin-coating method is shown in Figure 2.5. The sequential deposition of a

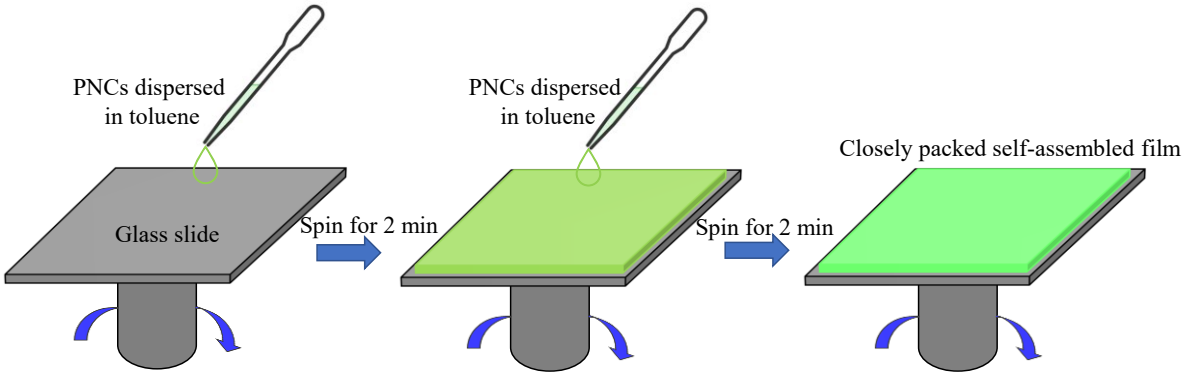

Figure 2.5. A scheme of PNC thin film preparation by the spin-coating technique.

PNC solution (dispersed in toluene, 1 mg mL^{-1}) on a glass substrate under constant spinning speed gave a closely packed perovskite thin film with uniform surface morphology, which is attributed to ligand-assisted self-assembling. Thus, PNCs in the films prepared from 1 mg/mL PNC solutions for PL studies are expected to self-assemble with the interparticle distance determined by the inter-penetrating oleic acid ligands.

2.2.3. Preparation of electron donor-acceptor heterojunction films

The heterojunction films of PNCs-C_{60} or PNCs-TiO_2 were prepared by the spin-coating or drop-casting technique. At first, the PNC thin-film with uniform morphology was obtained by the spin-coating method. One-half of a prepared PNC thin film was overlaid with high-density C_{60} by a drop-casting method. In the case of PNCs-TiO_2, I spin-coated the TiO_2 solution in ethanol on a glass substrate and annealed it to obtain a thin film with uniform thickness. Later one-half of the TiO_2 film was overlaid with a PNC solution by a drop-casting method.

2.2.4. Single-particle samples

The PNC samples for single-particle studies were prepared by a drop and drag method.[12,13] The PNC solution (10 µL, dispersed in toluene, 1 mg mL^{-1}) was diluted 100 times and dropped onto a glass coverslip. Immediately, the drop casted solution was dragged using a Whatman lens-cleaning paper. I controlled the density of the particles at 60-80 particles per 100 μm^2 area using this drop and drag technique. To avoid the ligand-induced agglomerations, I sprayed the precursor mixture on glass or Au-coated glass substrates.

2.2.5. Preparation of Au nanoparticle films

Figure 2.6 shows the scheme of Au NP film sputter-coating. Here, the excitons generated in

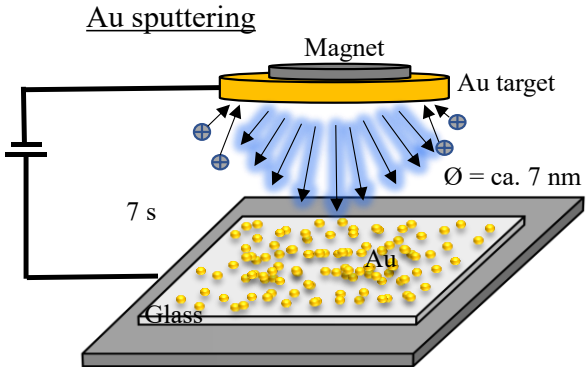

Figure 2.6. A scheme of Au NPs film preparation by magnetron sputtering.

perovskites were coupled with localized surface plasmon resonance (LSPR) of Au NPs. Au NP films were prepared by magnetron sputtering on the 25×50 glass coverslip for 7 s (100 V, 4 Pa, Figure 2.6). I obtained blue color Au plasmonic films with ca. 5 nm thick and ca. 8 nm long Au NPs.

2.3. Instrumentation

2.3.1 UV-vis spectrophotometry

To understand the excitonic properties of the PNCs, I characterized them using a UV-vis absorption spectrophotometer (Evolution 220, Thermo Fischer Scientific). The schematic representation of the spectrophotometer used in this study is shown in Figure 2.7. In this thesis,

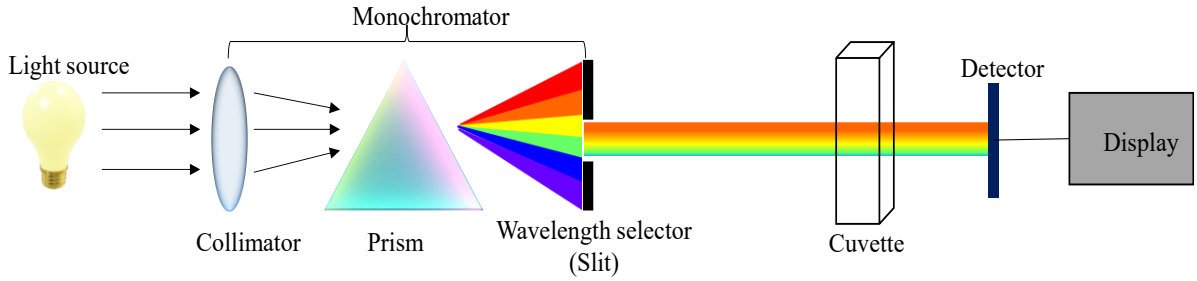

Figure 2.7. A scheme of a single-beam UV-vis absorption spectrophotometer.

I recorded the absorption of colloidal solutions of PNCs diluted in toluene from 350 to 700 nm. When the excitation light shines on the PNCs in toluene, the PNCs are electronically excited from the ground (VBM) to the excited state (CBM). The absorption spectrometer works based on the principle of Beer-Lambert's law: A= εcl, where 'ε' is the molar extinction coefficient (M^{-1} cm^{-1}), 'c' is concentration and 'l' is the path length. Typically, the spectrophotometer has four components: a light source, a monochromator, a sample holder, and a detector associated with the readout system. The combination of hydrogen or a deuterium lamp and a tungsten lamp is used as the light sources, which cover the wavelength region from 190 to 900 nm. The light source passes the monochromator and reaches the solution. The PNCs in the solution absorb the light and get excited from the ground state to the excited state. The detector records the transmitted light from the solution. Absorption spectra of PNCs solutions are presented in chapters 3, 4, and 5.

2.3.2 Steady-state fluorescence spectroscopy

The steady-state fluorescence spectroscopy was employed to examine the emission properties of PNC solutions using a fluorescence spectrometer (F-4500, Hitachi). The relaxation processes of the excitons from the excited to the ground states can be determined by this technique. A scheme of the optical setup of a fluorescence spectrometer in this study is shown in Figure 2.8. The excitation light source was a Xe-lamp, which provides a wavelength-

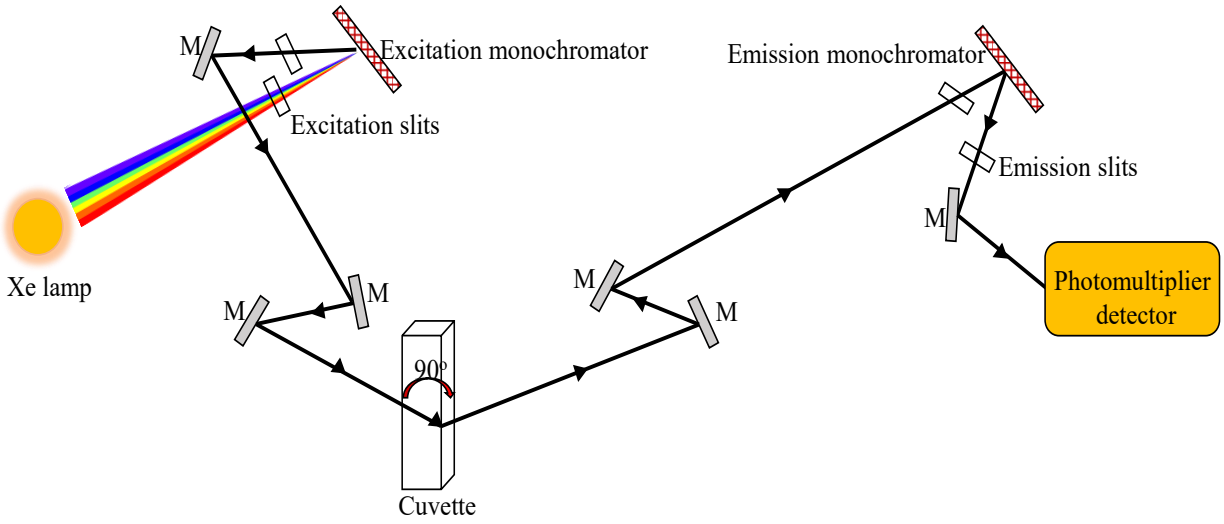

Figure 2.8. A scheme of a steady-state fluorescence spectrometer.

dependent bright light covering the UV to the infrared region. The spectrophotometer was constructed with several convenient optics surrounding the sample holder. To avoid the transmitted light in a fluorescence spectrum, the fluorescence was collected at 90°. In this study, the PNCs dispersed in toluene (1 mg mL^{-1}) were diluted 10 times, and the excitation wavelength was set at 400 nm. The emission intensities from the samples were scanned as a function of the wavelength. The PL quenching studies of electron donor-acceptor (D-A) samples (PNC-C_{60}, PNC-TCNB, and PNC-TCNQ) were also carried out using this fluorescence spectrometer. Fluorescence spectra of colloidal PNCs, and D-A's are shown in chapters 3, 4, and 5.

2.3.3 Time-resolved fluorescence spectroscopy

The exciton/carrier lifetimes of PNC solutions and films were studied using the time-resolved fluorescence spectroscopy. Similarly, the distance-dependent charge carrier diffusion and electron transfer dynamics in electron D-A systems were also analyzed using this technique. The optical setup for the time-resolved fluorescence spectroscopy is shown in Figure 2.9. The

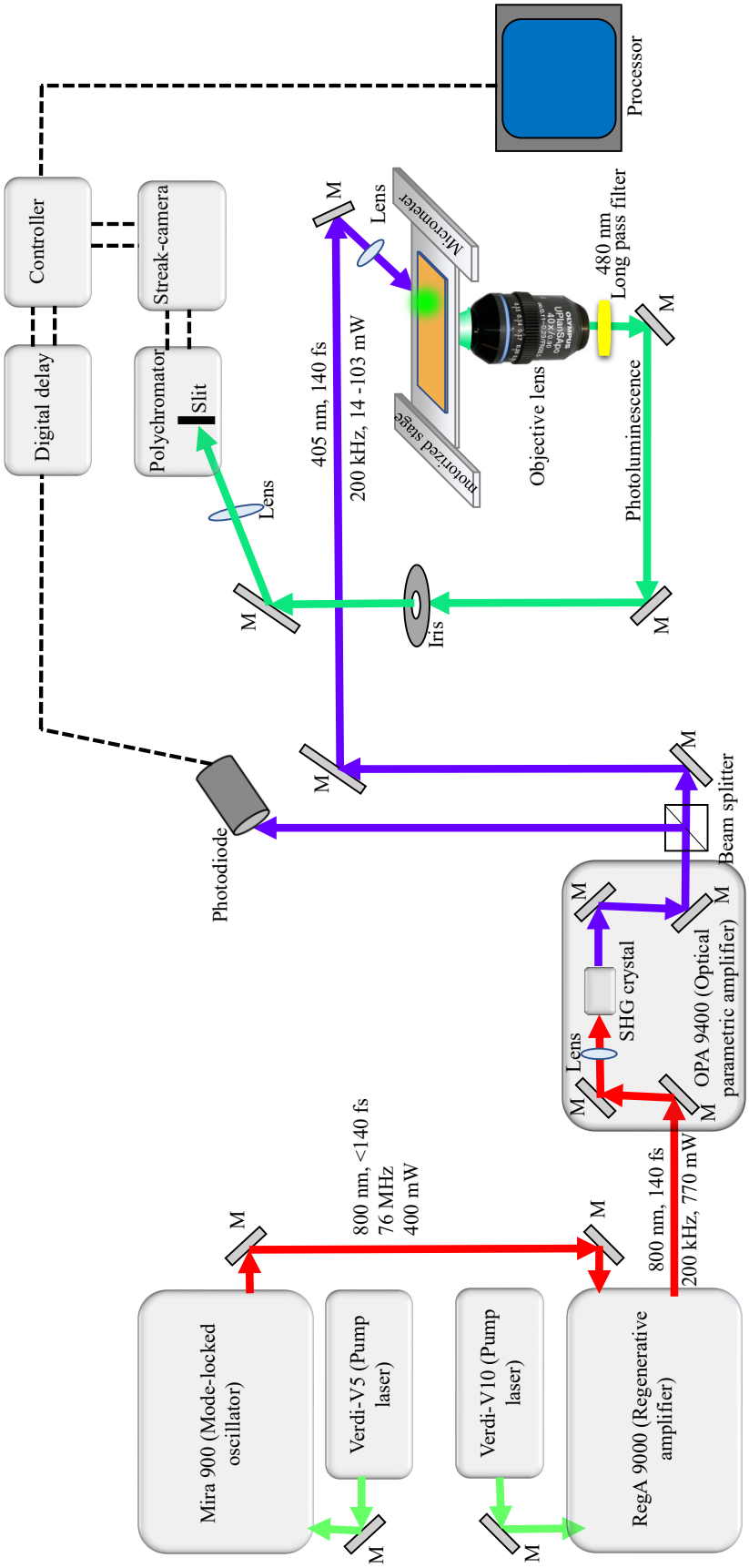

Figure 2.9. The optical setup of a time-resolved fluorescence spectrometer combined with an optical microscope.

second harmonic generation (SHG) signal (405 nm) from an optical parametric amplifier (Coherent OPA 9400) was used as an excitation light source. This OPA was pumped using a regenerative amplifier (Coherent RegA 9000) at 200 kHz. A mode-locked Ti-Sapphire oscillator (Coherent Mira 900) pumping at 76 MHz seeded the RegA. I used a polychromator (model 250IS, Chromex) and photon-counting Streak camera (model C4334, Hamamatsu) system to record the time-and spectrally resolved photons. The motorized stage with a micrometer was utilized in the distance-dependent PL measurements. PL decays of PNC solutions, films, and electron D-A systems (PNC-C_{60}/TiO_2/TCNB/TCNQ) are presented in chapters 3 and 4.

The PL decay profiles were fitted using the third exponential equation (1):

$$\gamma(t) = \alpha_0 + \alpha_1 e^{(-t/\tau 1)} + \alpha_2 e^{(-t/\tau 2)} + \alpha_3 e^{(-t/\tau 3)} \quad (1)$$

where α_0 is a constant, α_1, α_2, and α_3 are the amplitudes, and τ_1, τ_2, and τ_3 are the different lifetime components. Generally, the initial component arises from radiative recombination, and other two components are from non-radiative recombination. I calculated the intensity average PL lifetimes of the samples using equation (2):

$$\Sigma \alpha_n \tau_n / \Sigma \alpha_n \quad (2)$$

Time-correlated single-photon counting (TCSPC) system

The PL decay profiles of single PNCs were recorded using a TCSPC system. The schematic representation of the optical setup of the TCSPC system is shown in Figure 2.10. I used a picosecond (ps) laser (Advanced Laser Systems) pumping at 1 MHz with 465 nm ps pulses (45 ps) as the excitation light source. A TCSPC system made of an avalanche photodiode (APD, Perkin Elmer, SPCM-AQRH-15) and a TCSPC module (Becker & Hickl GmbH, SPC-M830) was utilized to track the PL decays. Furthermore, I placed an iris in front of the photodetector, to collect PL from selected single PNCs by restricting the detection area. During the measurements, neutral density (ND) filters were used to control the laser intensity. PL decays of single PNCs are discussed in chapters 4 and 5.

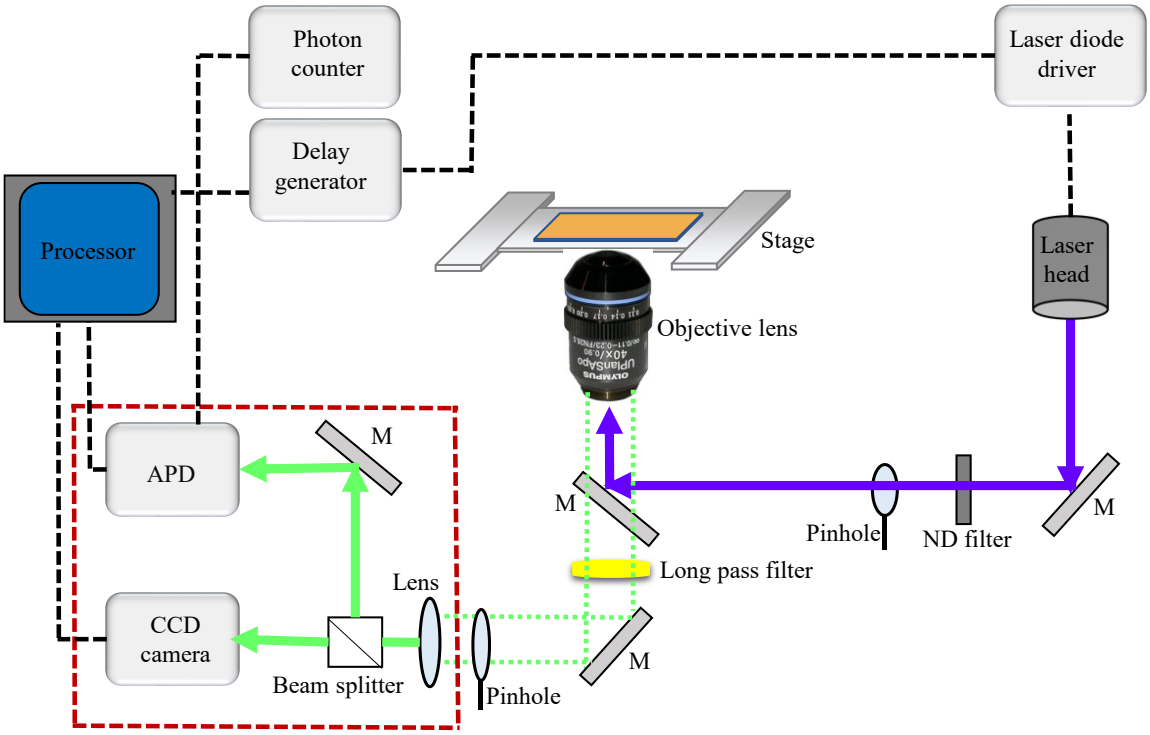

Figure 2.10. The optical setup of the TCSPC system.

2.3.4 Single-particle microspectroscopy

The PL blinking trajectories of single PNCs were recorded using a single-particle fluorescence microspectroscopy system under wide-field illumination. The optical setup of the system is shown in Figure 2.11. I used an IX71 Olympus inverted microscope connected with the iXon3, Andor Technology EMCCD camera to record the PL intensity trajectories of single PNCs. The

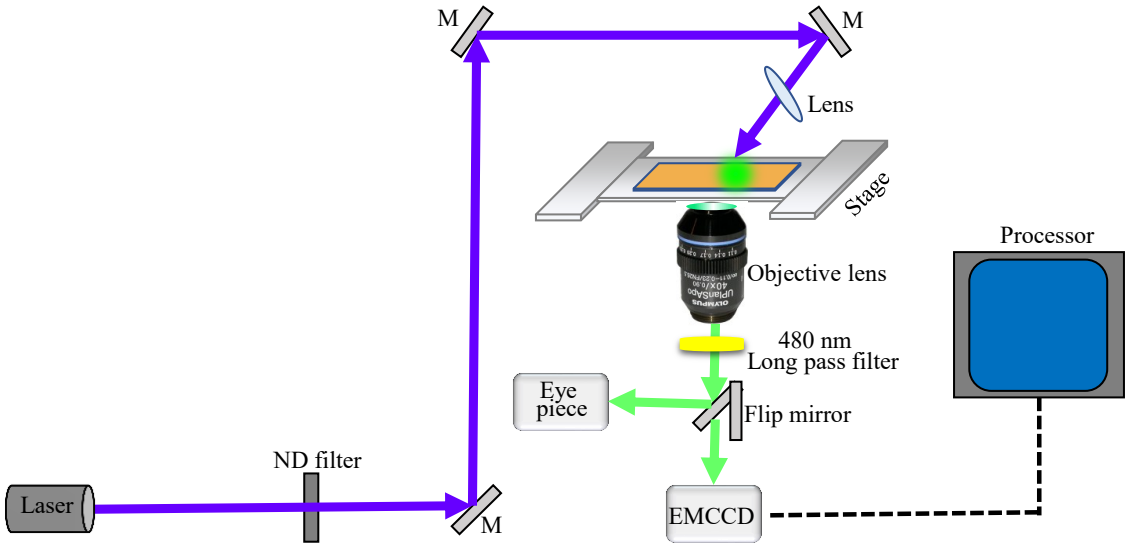

Figure 2.11. The optical setup for a single-particle fluorescence microspectroscopy

emitted PL was passed a 40x Olympus objective lens (NA = 0.60) followed by a 480 nm long-pass (LP) filter and recorded at 30 or 15 ms binning. I excited the samples with a 404 nm diode laser (ThorLabs, 6.5 mW). This laser diode and its temperature were controlled by the LDC210C (~400 mA) and TED200C (~12-13 ºC) controllers. The diffraction limit (hundreds of microns) is smaller than the focal spot in this optical setup. Hence, to minimize the background scattering, the fluorescence was collected using an objective lens at the back of the objective. I used EM gain at 100, where the signal-to-noise ratio is highest for this EMCCD. In this way, the PL blinking statistics of several isolated PNCs were collected within a single frame with high precision.

2.3.5 Transient absorption spectroscopy

Nanosecond transient absorption measurements

The NanoSpeK TSP-2000 (Unisoku Co., Ltd., Japan) system was employed for measuring the nanosecond TA of PNC-C_{60} D-A system. A PNC-C_{60} sample solution degassed by Ar-bubbling was excited with a Panther OPO pumped by a Nd:YAG laser (Continuum SLII-10, 4-6 ns full width at half maximum, CONTINUUM, USA). I used a Xe lamp (150 W) as the probe light while recording the absorbencies. A photomultiplier tube (Hamamatsu 2949, Hamamatsu photonics, Japan) was equipped as the detector. The temporal resolution of the IRF is less than 10 ns. The transient absorption data of the PNCs-C_{60} donor-acceptor sample are discussed in chapter 3.

2.3.6 Scanning transmission electron microscopy (STEM)

The sizes of the PNCs were estimated from STEM images. Samples for STEM measurements were prepared by dropping PNC solutions on the STEM Cu100P grids. In the case of W-PNCs, the nanocrystals were directly prepared on the STEM grids by spraying the precursor: GBL mixture (1:1) on the grids. The samples were dried overnight under a vacuum. The STEM and TEM images were recorded in a Hitachi HD-2000 microscope operated at 200 kV. The average edge length of PNCs was estimated using 'ImageJ' software. The STEM/TEM images are presented in chapters 3, 4, and 5.

2.3.7 Scanning electron microscopy (SEM)

Surface morphologies and the thicknesses of PNC films were recorded using a HITACHI SU8230 microscope. PNC thin films were prepared on glass slides by the spin-coating technique and dried under a vacuum for 12 hrs or longer. The films were cut at the center using

a diamond cutter to determine the thicknesses, and the cross-section images were recorded. The microscope consists of an electron source, and the emitted electrons move at high speeds under the applied thermal energy. These electrons interact with the sample surface and generate photons, which provide information regarding a sample's surface topography or composition. The SEM images of PNC films and electron D-A systems are shown in chapter 3.

2.3.8 The focused ion beam (FIB) fabrication

FIB is a micro-fabrication tool. FIB was used for preparing a cross-section TEM sample. The FIB grid is different from a TEM grid; there is no carbon film on the FIB grid. The sample cross-section was set at the edge of the FIB grid. Three processes were followed during the FIB processing: imaging, sputtering, and deposition. When the Ga ion was irradiated to the sample, the secondary ions and electrons were emitted from the surface. The sample image was obtained by detecting these secondary particles. This image is called a scanned ion microscope (SIM) image. The Ga ion is used as an ion beam source due to its low atomic mass (69.723), low melting point (29.8 °C), and good wettability. The acceleration voltage of the Ga ion beam was 40 kV (15 kV is used for finishing). The beam intensity was tuned by varying the aperture size. Strong Ga ion beam irradiation sputters the sample. The irradiated Ga ion is reflected or penetrates the sample surface. During FIB sputtering, the real-time SIM images of the samples were observed. The third function of FIB, tungsten deposition, protects the sample, stick samples, and probes on the FIB grid. Tungsten deposition was made by the reaction between secondary electrons and tungsten hexacarbonyl gas. Tungsten atoms were deposited on the sample surface, and CO formed as a byproduct was removed under a vacuum. A scheme of these three FIB processes is shown in Figure 2.12. The cross-section TEM image of Au NPs obtained by this FIB technique is presented in chapter 5.

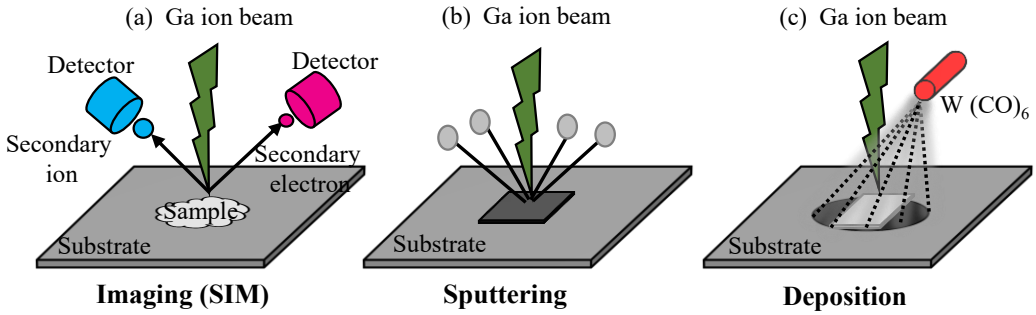

Figure 2.12. A scheme of the FIB principles: (a) SIM imaging, (b) ion beam sputtering, and (c) tungsten deposition.

References

1. Chouhan, L.; Ito, S.; Thomas, E. M.; Takano, Y.; Ghimire, S.; Miyasaka, H.; Biju, V. Real-Time Blinking Suppression of Perovskite Quantum Dots by Halide Vacancy Filling. *ACS Nano* **2021**, *15*, 2831–2838.

2. Chouhan, L.; Ghimire, S.; Subrahmanyam, C.; Miyasaka, T.; Biju, V. Synthesis, Optoelectronic Properties and Applications of Halide Perovskites. *Chem. Soc. Rev.* **2020**, *49*, 2869–2885.

3. Sachith, B. M.; Okamoto, T.; Ghimire, S.; Umeyama, T.; Takano, Y.; Imahori, H.; Biju, V. Long-Range Interfacial Charge Carrier Trapping in Halide Perovskite-C_{60} and Halide Perovskite-TiO_2 Donor-Acceptor Films. *J. Phys. Chem. Lett.* **2021**, 12, 8644–8651.

4. Nair, V. C.; Muthu, C.; Rogach, A. L.; Kohara, R.; Biju, V. Channeling Exciton Migration into Electron Transfer in Formamidinium Lead Bromide Perovskite Nanocrystal/Fullerene Composites. *Angew. Chem. Int. Ed.* **2017**, *56*, 1214–1218.

5. Ghimire, S.; Chouhan, L.; Takano, Y.; Takahashi, K.; Nakamura, T.; Yuyama, K. I.; Biju, V. Amplified and Multicolor Emission from Films and Interfacial Layers of Lead Halide Perovskite Nanocrystals. *ACS Energy Lett.* **2019**, *4*, 133–141.

6. Protesescu, L.; Yakunin, S.; Bodnarchuk, M. I.; Krieg, F.; Caputo, R.; Hendon, C. H.; Yang, R. X.; Walsh, A.; Kovalenko, M. V. Nanocrystals of Cesium Lead Halide Perovskites ($CsPbX_3$, X = Cl, Br, and I): Novel Optoelectronic Materials Showing Bright Emission with Wide Color Gamut. *Nano Lett.* **2015**, *15*, 3692–3696.

7. Wu, K.; Liang, G.; Shang, Q.; Ren, Y.; Kong, D.; Lian, T. Ultrafast Interfacial Electron and Hole Transfer from $CsPbBr_3$ Perovskite Quantum Dots. *J. Am. Chem. Soc.* **2015**, *137*, 12792–12795.

8. Clinckemalie, L.; Valli, D.; Roeffaers, M. B. J.; Hofkens, J.; Pradhan, B.; Debroye, E. Challenges and Opportunities for $CsPbBr_3$ Perovskites in Low- A Nd High-Energy Radiation Detection. *ACS Energy Lett.* **2021**, *6*, 1290–1314.

9. Pushkarev, A. P.; Korolev, V. I.; Markina, D. I.; Komissarenko, F. E.; Naujokaitis, A.; Drabavičius, A.; Pakštas, V.; Franckevičius, M.; Khubezhov, S. A.; Sannikov, D. A.; Zasedatelev, A. V.; Lagoudakis, P. G.; Zakhidov, A. A.; Makarov, S. V. A Few-Minute Synthesis of $CsPbBr_3$ Nanolasers with a High-Quality Factor by Spraying at Ambient Conditions. *ACS Appl. Mater. Interfaces* **2019**, *11*, 1040–1048.

10. Zhou, S.; Zhou, G.; Li, Y.; Xu, X.; Hsu, Y. J.; Xu, J.; Zhao, N.; Lu, X. Understanding Charge Transport in All-Inorganic Halide Perovskite Nanocrystal Thin-Film Field Effect Transistors. *ACS Energy Lett.* **2020**, *5*, 2614–2623.

11. Guo, Z.; Manser, J. S.; Wan, Y.; Kamat, P. V.; Huang, L. Spatial and Temporal Imaging of Long-Range Charge Transport in Perovskite Thin Films by Ultrafast Microscopy. *Nat. Commun.* **2015**, *6*, 7471.

12. Thomas, E. M.; Ghimire, S.; Kohara, R.; Anil, A. N.; Yuyama, K. I.; Takano, Y.; Thomas, K. G.; Biju, V. Blinking Suppression in Highly Excited CdSe/ZnS Quantum

Dots by Electron Transfer under Large Positive Gibbs (Free) Energy Change. *ACS Nano* **2018**, *12*, 9060–9069.

13. Chouhan, L.; Ghimire, S.; Biju, V. Blinking Beats Bleaching: The Control of Superoxide Generation by Photo-Ionized Perovskite Nanocrystals. *Angew. Chem. Int. Ed.* **2019**, *58*, 4875–4879.

14. Okuhata, T.; Katayama, T.; Tamai, N. Ultrafast and Hot Electron Transfer in CdSe QD-Au Hybrid Nanostructures. *J. Phys. Chem. C* **2020**, *124*, 1099–1107.

15. Zang, X.; Shi, X.; Oshikiri, T.; Ueno, K.; Sunaba, Y.; Sasaki, K.; Misawa, H. Highly Sensitive and Spatially Homogeneous Surface-Enhanced Raman Scattering Substrate under Plasmon-Nanocavity Coupling. *J. Phys. Chem. C* **2021**, 125, 19880-19886.

Chapter 3
Charge carrier and electron transfer dynamics in perovskite nanocrystal films

Abstract

Photoinduced electron transfer (PET) studies in perovskite nanocrystal-based electron donor-acceptor (D-A) systems receive great momentum, owing to their potential application to solar cell technology. Nevertheless, radiative and nonradiative carrier losses adversely affect the energy conversion efficiency in thick perovskite films. To overcome these challenges, it is particularly important to investigate the photoinduced electron transfer dynamics, carrier trapping, and relaxation process at perovskite-based donor-acceptor interfaces. In this chapter, I demonstrate long-range charge carrier diffusion and distance-dependent electron transfer in heterojunction films of cesium or formamidinium lead bromide ($Cs/FAPbBr_3$) PNCs and C_{60} or TiO_2. I synthesized $CsPbBr_3$ and $FAPbBr_3$ PNCs by the hot-injection and LARP methods, respectively, and their thin films with different thicknesses were prepared by ligand-assisted assembly formation. To understand the electron transfer, the PL quenching experiment was performed for $Cs/FAPbBr_3$ PNC solution by treating them with a C_{60} solution (in toluene) in 25 μM portions in a stepwise fashion. The PET and charge separation were confirmed from the PL lifetime, PL intensity, and TA spectra in the solution phase. Subsequently, I prepared the D-A heterojunction films with $Cs/FAPbBr_3$ PNCs as the donor and C_{60} or TiO_2 as the acceptor. To understand the carrier collection as a function of the distance and thicknesses in the films, I conducted distance-dependent PL experiments by systematically moving the excitation from the perovskite to D-A interface region. Interestingly, the carrier recombination rates at different distances reveal the complete electron transfer and emission quenching within 100 μm of the interface. Here, radiative recombination dominates the electron transfer process while moving the interface away from the excitation center. Also, the electron transfer becomes negligibly small at 800 μm or beyond the interface.

3.1 Introduction

Halide perovskite nanocrystals (PNCs) become attractive due to their high photoluminescence quantum yields,[1,2] tunable bandgaps,[3] and straightforward syntheses.[6-9] As a result, these materials have become superior light absorbers in solar cells,[10-23] and the certified power conversion efficiency of a perovskite solar cell (PSC) exceeds 25%.[24] The long-range migration of charge carriers and delayed emission from PNC films attract much attention in the PSC field.[25] Generally, radiative relaxations are delayed in bulk films or microcrystals,[26,27] but PNCs undergo ultrafast radiative recombination. By processing these PNCs into thin films, high-efficiency PSCs have been developed.[28,29] Several methods, including one-step spin-coating, two-step sequential deposition, and vapor deposition in a high-vacuum chamber, have been used to prepare PNC thin films for solar cell fabrication.[30-35] Additionally, different types of device architectures are reported in the literature, particularly the mesostructured and planar type solar cells are well-established architectures. The typical device configuration of a heterojunction PSC comprises a perovskite layer sandwiched between the anode and cathode. In such an architecture, the device performance mainly depends on the electron donor-acceptor (D–A) systems. The electron D-A interfaces consist of perovskite as the electron donor and TiO_2, SnO_2, TCNB, TCNQ, or fullerene (C_{60}) derivatives such as PCBM-C_{61}, or PCBM-C_{71}.[36-42] However, individual PNC's charge carrier dynamics and electron transfer efficiencies can be different from their films. Also, the distance- or thickness-dependent recombination dynamics of photogenerated excitons/charge carriers at the perovskite-electron acceptor interface are important subjects in the PSC field.

Photoinduced electron transfer (PET) is the fundamental process in a solar cell.[43-47] In principle, the photogenerated excitons in PNCs split into free carriers, and it's necessary to capture them more efficiently using hole and electron transport layers (ETLs). This was first achieved in 2015 by Snaith and co-workers[48] developed efficient PSCs using solution spin-coated C_{60} in regular n-i-p structures. They found the effectiveness of C_{60} as an ETL, which shows excellent electron extraction ability and increases the long-term performance of PSCs. This opened a door for developing regular n-i-p high-performance PSCs. Later many reports showed higher power conversion efficiencies in PSC by achieving charge separation using different ETLs. For example, Long and co-workers[49] used TiO_2 as an electron acceptor in a PSC and reported the high efficiency contributed by the ultrafast interfacial charge separation. The electron injection is fast at the perovskite-electron acceptor (e.g., TiO_2) interface. In a subsequent study, Chen and co-workers[50] used a high-quality polycrystalline SnO_2 film as the electron-transport layer (ETL) in an n-i-p-type PSC. They reported the best solar cells

fabricated using these layers and achieved 20.52% power conversion efficiency, which was among the best in the planar n–i–p-type PSCs class. Recently, Xu and co-workers[51] used four types of ETLs, i.e., compact titanium dioxide (c-TiO_2), mesoporous titanium dioxide (m-TiO_2) composite layers, C_{60}, and c-TiO_2 and C_{60}. The c-TiO_2-based PSCs showed higher efficiency (20.15%) than other ETL materials. The champion device efficiency using the C_{60} ETL achieved before was 17.15%. These outcomes encouraged me to evaluate the interfacial region between the PNCs and electron acceptors and control the electron transfer from perovskite films by controlling the diffusion of photogenerated charge carriers.

This chapter demonstrates the long-range charge carrier diffusion and distance-dependent electron transfer in heterojunction films of Cs/$FAPbBr_3$ PNCs and C_{60} or TiO_2. I synthesized $CsPbBr_3$ and $FAPbBr_3$ PNCs and their thin films by ligand-assisted assembly formation. The as-prepared PNCs show short PL lifetimes, whereas the films show longer lifetimes due to the diffusion of photogenerated excitons among PNCs and an increased rate of trapping-detrapping. First, the PL quenching experiment was performed for Cs/FAPbBr3 PNC solutions to understand the electron transfer by treating them with C_{60} solutions (in toluene) in 25 μM portions in a stepwise fashion. This C_{60} treatment resulted in a static PL quenching suggesting the adsorption of C_{60} onto the hydrophobic surface of the PNCs. Also, transient absorption studies reveal the formation of C_{60} radical anion at ca. 980 nm. I prepared the heterojunction films with Cs/$FAPbBr_3$ PNCs as the electron donors and C_{60} or TiO_2 as the electron acceptors. I conducted distance-dependent PL experiments to understand the carrier collection at different distances and thicknesses in the films by systematically moving the excitation from the perovskite region to the interface region. The carrier recombination rates at different distances helped me reveal quantitative electron transfer and emission quenching within 100 μm of the interface. Conversely, radiative recombination dominated the electron transfer process by moving the interface away from the excitation center. This electron transfer becomes negligible at 800 μm or beyond the interface.

3.2 Results and discussion

3.2.1 Characterization of PNCs and their films

The synthesis of $FAPbBr_3$ PNCs was carried out by a modified LARP method, whereas a modified hot-injection technique was employed to prepare $CsPbBr_3$ PNCs. The detailed synthesis procedures are given in section 2.2.1. As-synthesized PNCs dispersed in toluene were processed into thin films by ligand-assisted self-assembly formation. The pristine PNCs and their films were characterized using STEM, SEM, UV-vis absorption, and PL spectroscopy.

The STEM images of both $FAPbBr_3$ and $CsPbBr_3$ PNCs are shown in Figures 3.1A and B, respectively.

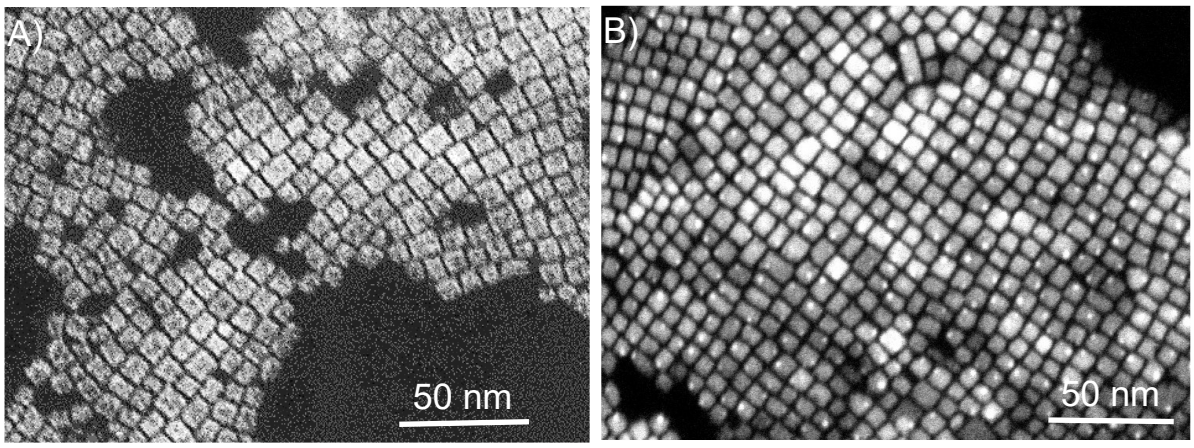

Figure 3.1. Structural characteristics of PNCs. STEM images of (A) $FAPbBr_3$ and (B) $CsPbBr_3$ PNCs.

The STEM images reveal a uniform size distribution of the PNCs. I analyzed the STEM images using imageJ software and estimated the size distribution. The hot-injection synthesis of $CsPbBr_3$ provides cubic PNCs with a size distribution of ca. 10 nm, and the LARP synthesis of $FAPbBr_3$ provides ca. 12 nm PNCs. The STEM samples prepared from a very low concentration of PNC solution showed a close-packing or self-assembling character, supported by the surface ligands. According to the obtained STEM images, the interparticle distance is 1.6 nm, the same as the ligand length. Thus, the thin films prepared for electron transfer studies are expected to be formed by self-assembling.

The surface morphological features and thicknesses of the prepared films were studied by SEM imaging. The SEM images with uniform surface morphologies of $FAPbBr_3$ and $CsPbBr_3$ PNC thin films are represented in Figures 3.2A and B, respectively. A cross-section analysis method[52] was employed to understand the thicknesses of the films, as shown in Figures 3.2C ($FAPbBr_3$) and D ($CsPbBr_3$). The cross-section SEM images were analyzed using imageJ software and estimated the average thicknesses at 2.5 μm for $FAPbBr_3$ and 1.4 μm for $CsPbBr_3$, and 1.7 μm for C_{60} and 4.6 μm for TiO_2. It is well established that PSCs exhibit high performance for the film thickness within 100's of nm (experimentally 250-2000 nm).[53-55] Thus, optimizing the electron transfer properties of PNC films is critical to enhancing the impact of PSCs.

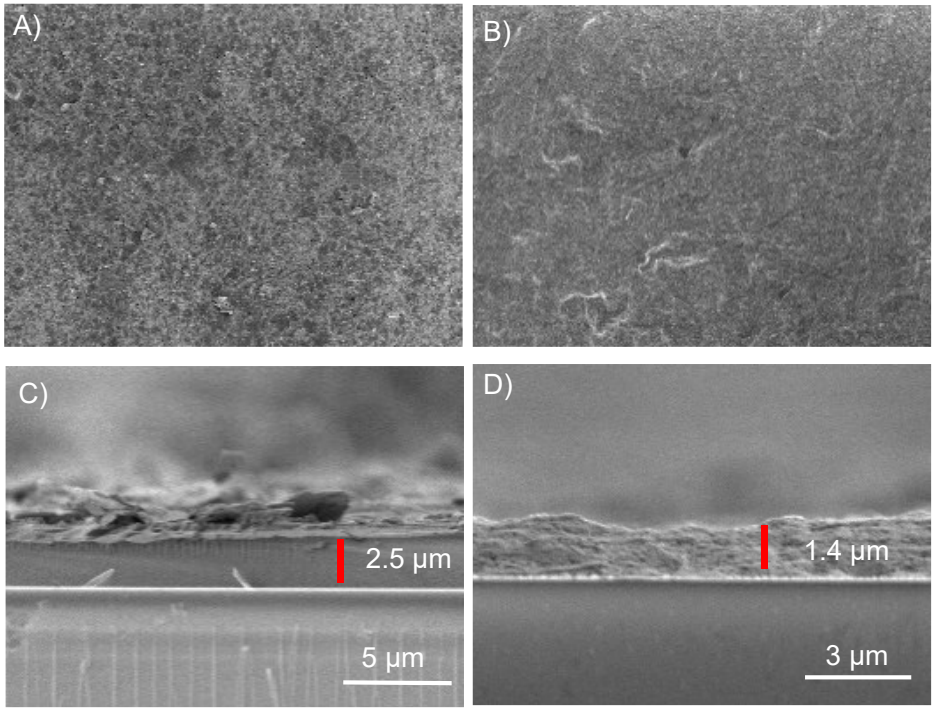

Figure 3.2. (A, B) Surface morphologies and (C, D) cross-sections of PNCs films. SEM images of (A, C) $FAPbBr_3$ and (B, D) $CsPbBr_3$ PNC films.

Moreover, the film thicknesses used in this chapter are ideal for efficient charge carrier collection and for controlling the radiative recombination rates.

First, I studied the optical properties of the PNCs by UV-vis absorption and steady-state fluorescence measurements. The absorption and PL spectra of FA/$CsPbBr_3$ PNC solutions (dispersed in toluene) are presented in Figure 3.3A. Photograph of a $FAPbBr_3$ PNC solution is

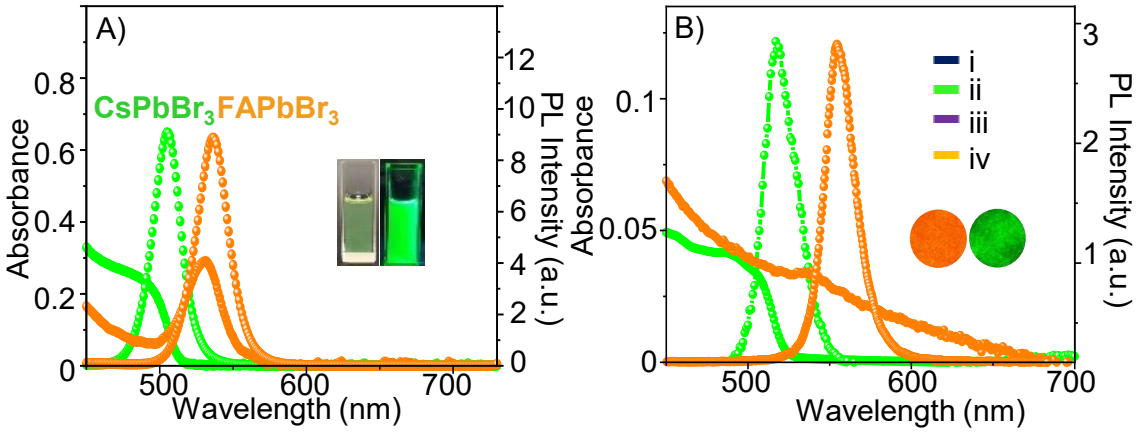

Figure 3.3. Optical properties of PNCs and films. (A) Absorption and PL spectra of PNC solutions; [insets: the photographs of a $FAPbBr_3$ solution under the room light (left) and UV light (right)] and (B) their films [(i, ii): $CsPbBr_3$. (iii, iv): $FAPbBr_3$, λ_{ex}: 400 nm].

shown in the inset (taken under room light or UV light). A $CsPbBr_3$ solution exhibited the PL ca. 505 nm, whereas the $FAPbBr_3$ solution showed it at ca. 533 nm. The PL is intense and shows a narrow fwhm (23 and 25 nm for $CsPbBr_3$ and $FAPbBr_3$, respectively). The small widths are consistent with their small sizes. Similarly, the PNC films were characterized, and their absorption and PL spectra are shown in Figure 3.3B. Interestingly, the films show red-shifted PL compared to their solutions (513 nm for $CsPbBr_3$ and 554 nm for $FAPbBr_3$). These redshifted maxima of the films are due to photon recycling and migration of carriers in the films.

3.2.2 Charge carrier dynamics in solutions and films

Charge carrier dynamics in PNC solutions and films are studied using a TCSPC system. Figures 3.4A show the PL decay profiles of a $FAPbBr_3$ PNC solution and film, and the inset represents the photograph of $FAPbBr_3$ PNCs dispersed in toluene and taken under UV light. The PL decay profiles were fitted using the third exponential equation (1):

$$\gamma(t) = \alpha_0 + \alpha_1 e^{(-t/\tau 1)} + \alpha_2 e^{(-t/\tau 2)} + \alpha_3 e^{(-t/\tau 3)} \quad (1)$$

where α_0 is a constant, α_1, α_2, and α_3 are the amplitudes, and τ_1, τ_2, and τ_3 are the lifetime components. Generally, the initial component arises from radiative recombination and the other two from non-radiative recombinations. I calculated the average PL lifetimes of the samples using equation (2):

$$\Sigma \alpha_n \tau_n / \Sigma \alpha_n \quad (2)$$

The obtained average PL lifetime of a $FAPbBr_3$ solution is ca. 87 ns, but surprisingly, its corresponding film showed a much longer PL lifetime (645 ns). When the PNCs were dissolved in toluene, the hydrophobic ligands well-extend in the solvent, rendering PNCs isolated. In contrast, the PNCs in a thin film are expected to self-assemble with the interparticle distance determined by the interpenetrating ligands.

The closely packed self-assembled PNC film induces a large dielectric constant, decreasing the degree of quantum confinement and the exciton binding energy. The electron's mean-free paths in halide perovskites generally range within 10's of nm, and electron delocalization and hole localization can occur. According to the obtained STEM images, the interparticle distance is 1.6 nm, the same as the ligand length. I assume the early excitons split

into free carriers and migrate in the films, lowering the recombination rates.[56,57] I propose the diffusion or migration of charge carriers by hopping among $FAPbBr_3$ PNCs in close-packed films, which increases the PL lifetime by lowering the recombination rates. A scheme of such a ligand-assisted self-assembled close-packed film is shown in Figure 3.4B.

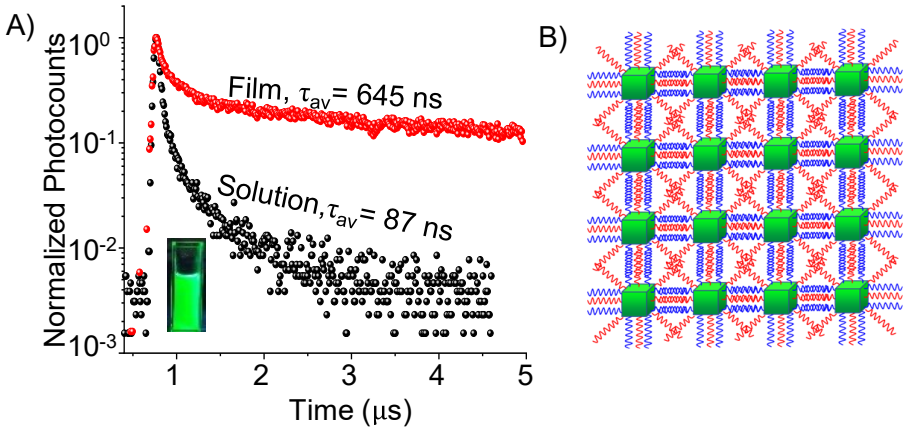

Figure 3.4. Charge carrier dynamics of $FAPbBr_3$ PNCs. (A) PL decay profiles of a solution and a film. The samples were excited with a 405 nm laser. (B) A scheme of ligand-assisted self-assembly of PNCs.

3.2.3 Electron transfer dynamics in solutions

To study the electron transfer dynamics in a PNC solution, I choose C_{60} as the electron acceptor. The prepared electron D-A system was studied using a steady-state PL spectroscopy system. Figure 3.5 indicates the PL spectra of a $FAPbBr_3$ PNC solution without or with C_{60} and their

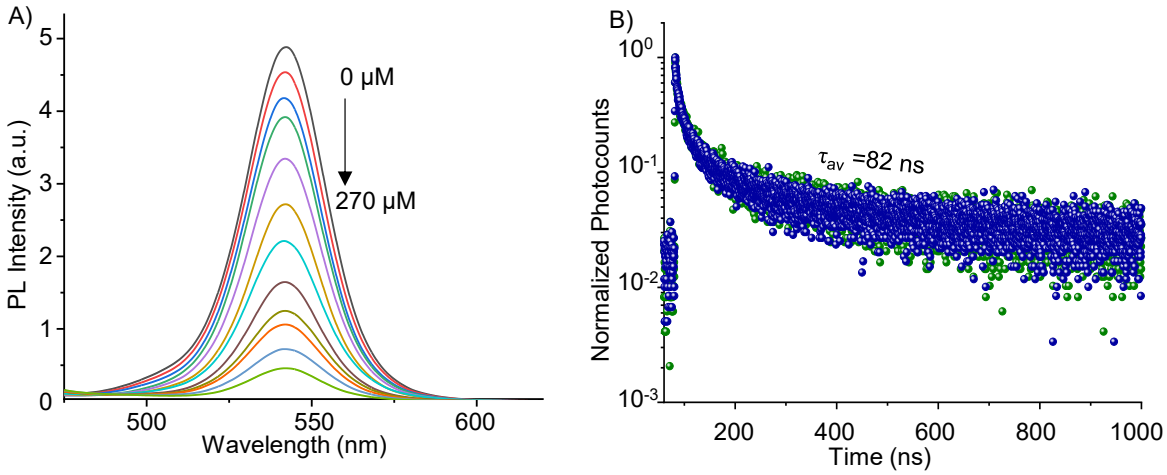

Figure 3.5. PL quenching in the solution phase. (A) PL spectra and (B) PL decay profiles of $FAPbBr_3$ PNC solutions treated with C_{60} (λ_{ex}: 405 nm).

PL decay profiles. At first, the PL quenching experiment was performed for a $FAPbBr_3$ PNC solution by treating it with a C_{60} solution (in toluene). As the concentration of C_{60} was increased from 25 µM to 270 µM, the PL intensity of the PNC solution was quantitatively decreased, which suggests efficient electron transfer from photoactivated PNCs to C_{60}. Similarly, the PL decay profiles of a $FAPbBr_3$ PNC solution without or with different concentrations of C_{60} were recorded using a TCSPC system. Interestingly, the PL lifetime of the samples remained constant (82 ns) regardless of the concentration of C_{60}.

To confirm this electron transfer dynamics, I performed similar experiments in the $CsPbBr_3$:C_{60} D-A system. As the concentration of C_{60} was increased, the PL intensity of a $CsPbBr_3$ PNC solution was decreased (Figure 3.6A), and the corresponding PL lifetime remained constant (9 ns) regardless of the C_{60} concentration (Figure 3.6B).

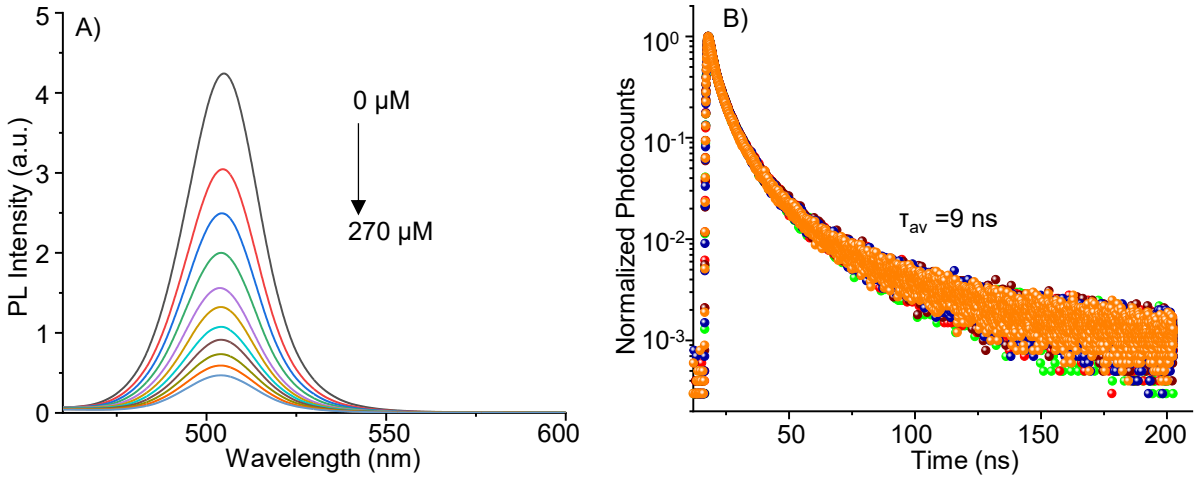

Figure 3.6. PL quenching in the solution phase. (A) PL spectra and (B) PL decay profiles of $CsPbBr_3$ PNC solutions treated with C_{60} (λ_{ex}: 405 nm).

Both the donor-acceptor systems showed the static electron transfer behavior, which is evident with the constant PL lifetime with a decrease in the PL intensity by increasing the C_{60} concentration. In other words, the PNCs, when dispersed in toluene, the long-chain ligands attached to the hydrophobic surface of the PNC make them isolated. Thus, the added C_{60} was adsorbed onto the hydrophobic surface, resulting in the PL quenching, and the PL signals we detected are from the PNCs free from C_{60} adsorption. To understand this PL quenching behavior, I mapped the photocounts or PL lifetimes against the acceptor (C_{60}) concentration (Figure. 3.7A). The resulted graph suggests that the PL quenching is dominated by static interaction at lower C_{60} concentrations. Here, the C_{60} effectively quenched the PL intensity by

trapping excited electrons in the PNCs. Thus, the PL we detected from the C_{60}-free PNCs show the lifetime equivalent to the pristine PNC.

I used nanosecond transient absorption spectroscopy to obtain further insight into the electron transfer dynamics in the D-A systems. The transient absorption spectrum of a $FAPbBr_3$ PNC solution supplemented with C_{60} is represented in Figure 3.7B. After adding C_{60} to the PNC solution, the electron transfer process was evident from the formation of $C_{60}^{\bullet-}$ ca 980 nm (Figure 3A). The kinetic decay profile of $C_{60}^{\bullet-}$ at 980 nm has a half-life of 3.1 µs, as shown in Figure. 3.7C. As reported in the literature, the C_{60} triplet lifetime is 45 µs in toluene,[58] which is

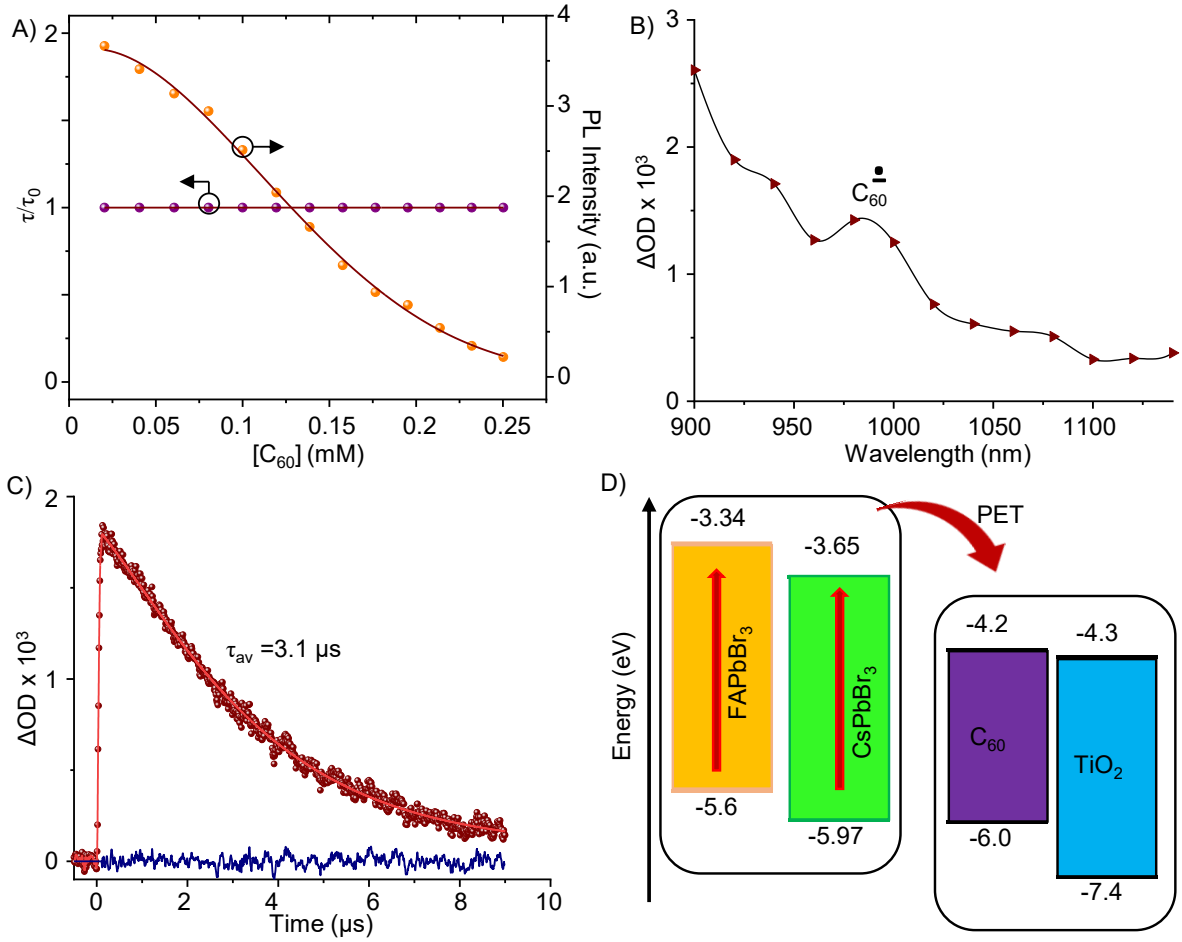

Figure 3.7. Electron transfer dynamics. (A) The PL intensity or lifetime plotted against the concentration of C_{60}. (B) The transient absorption spectrum of a $FAPbBr_3$ PNC solution supplemented with C_{60} and (C) the kinetic decay profile of the C_{60} radical anion. (D) A scheme describing the energy levels of $FA/CsPbBr_3$ and C_{60}/TiO_2, according to the vacuum level.

completely different from the result that I obtained at 980 nm (3.1 µs). Therefore, the transient absorption band is attributed to $C_{60}^{\bullet-}$. Also, the positive signals were not detected for PNC alone

in this region or the timescale without C_{60}. Figure 3.7D represents the energy level diagram (relative to the vacuum level)[41,43,47] for the donors and acceptors. The energy levels FA/$CsPbBr_3$ and C_{60}/TiO_2 suggest the feasibility of electron transfer, where the LUMO of C_{60} is lower than the FA/$CsPbBr_3$ conduction band.

3.2.4 Electron transfer dynamics in heterojunction films

The thickness of a PNC film plays a significant role in controlling the carrier dynamics. It is well established that a thicker film over 100 µm undergoes radiative recombination within the film and photon recycling, lowering the carrier collection efficiency. To understand the long-range carrier migration at heterojunctions, thin films were prepared using $FAPbBr_3$ PNCs by drop-casting. Later, I used C_{60} (high density) to cover one-half of the film. The images of the prepared heterojunction film ($FAPbBr_3$:C_{60}) taken under room or UV light and its scheme are shown in Figure 3.8A. On the other hand, I chose TiO_2 as another electron acceptor to-

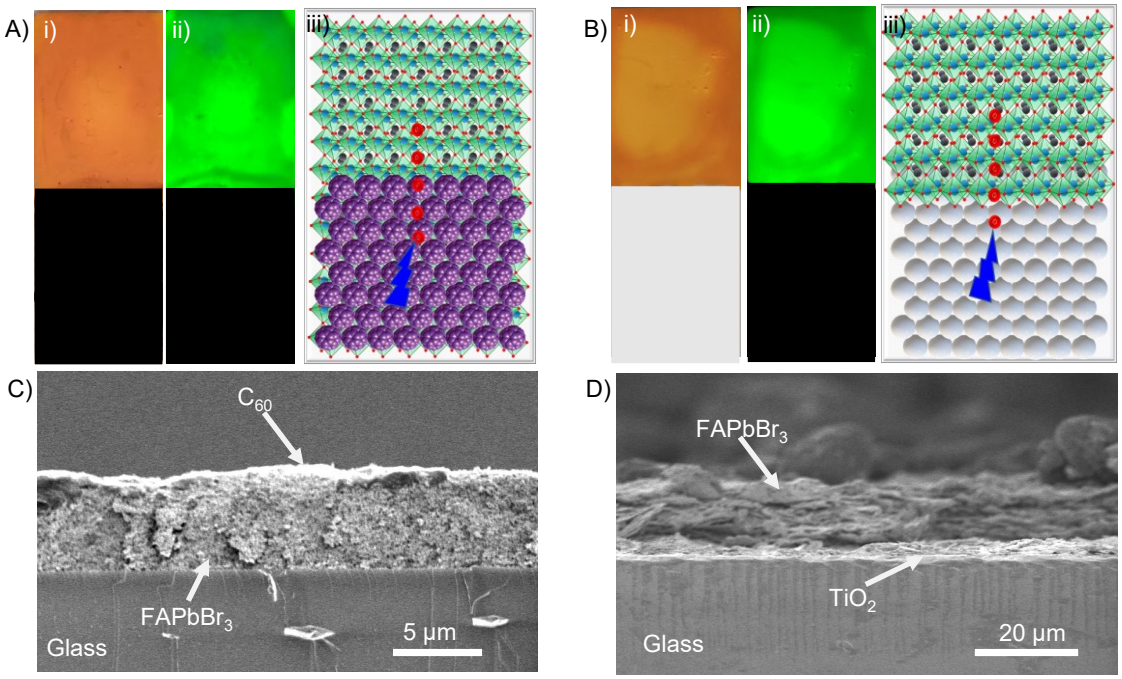

Figure 3.8. Electron donor-acceptor heterojunction films with $FAPbBr_3$ as the donor. (A, B) Photographs and (C, D) SEM images of the heterojunction films with (A, C) C_{60} and (B, D) TiO_2. (i, ii) The images taken under (i) room light and (ii) UV light.

correlate the interfacial electron transfer dynamics. In this case, one-half of the TiO_2 film was covered with $FAPbBr_3$ PNCs (Figure 3.8B). I marked the interface region as 0 µm by observing through the optical microscope. Similarly, I marked the electron acceptor region as negative

(e.g., -100 µm) and positive for the PNC-only region (e.g., 100 µm), as shown in Figure 3.8 (iii). The prepared heterojunction films were confirmed by the SEM cross-section method. Figure 3.8C and D show the SEM cross-section images of $FAPbBr_3$:C_{60} and $FAPbBr_3$:TiO_2, respectively. Furthermore, the heterojunction films' surface morphologies are also studied by SEM imaging. Figures 3.9A and B show that both the heterojunction films show uniform surfaces and distinct interfaces.

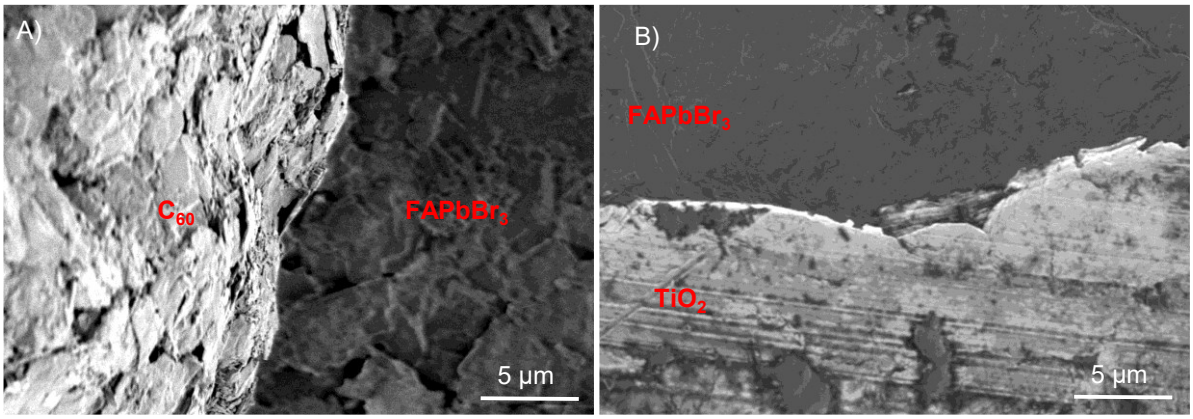

Figure 3.9. Heterojunction films. SEM images of the heterojunction films with (A) C_{60} and (B) TiO_2, showing the donor ($FAPbBr_3$) and the acceptor (C_{60} or TiO_2) regions.

To investigate the interfacial distance-dependent carrier dynamics, I used an assembly of a polychromator and a photon-counting Streak camera. Spectrally and temporally resolved photons (Figure 3.10A) were systematically collected from the heterojunction films at every 100 µm distance. As the collection point was moved towards the interface region, the PL lifetime of the $FAPbBr_3$/C_{60} heterojunction film was decreased from 675 ns to 36 ns, along with a decrease in photocounts. This observation is different from the PNC solution treated with C_{60}. These results indicate the efficient electron transfer from PNCs to C_{60}, dominated by dynamic interactions. The instrumental setup for this distance-dependent PL experiment is discussed in section 2.3.3. Figure 3.10A represents the distance-dependent PL decay profiles of a $FAPbBr_3$:C_{60} heterojunction film, and the photons emitted at 1000 µm, and 0 µm distances are shown in Figures 3.10B.

To correlate these obtained results, I performed similar distance-dependent experiments by recording the PL intensities and lifetimes for the heterojunction film of $FAPbBr_3$:TiO_2. I obtained similar results, i.e., by moving the excitation from the perovskite-only region to the interface region, the PL lifetime was decreased from 622 to 36 ns [Figure. 3.11A and B (i: 1000 µm), (ii: 0 µm)], which is accompanied by a decrease in the number of emitted photons. Like

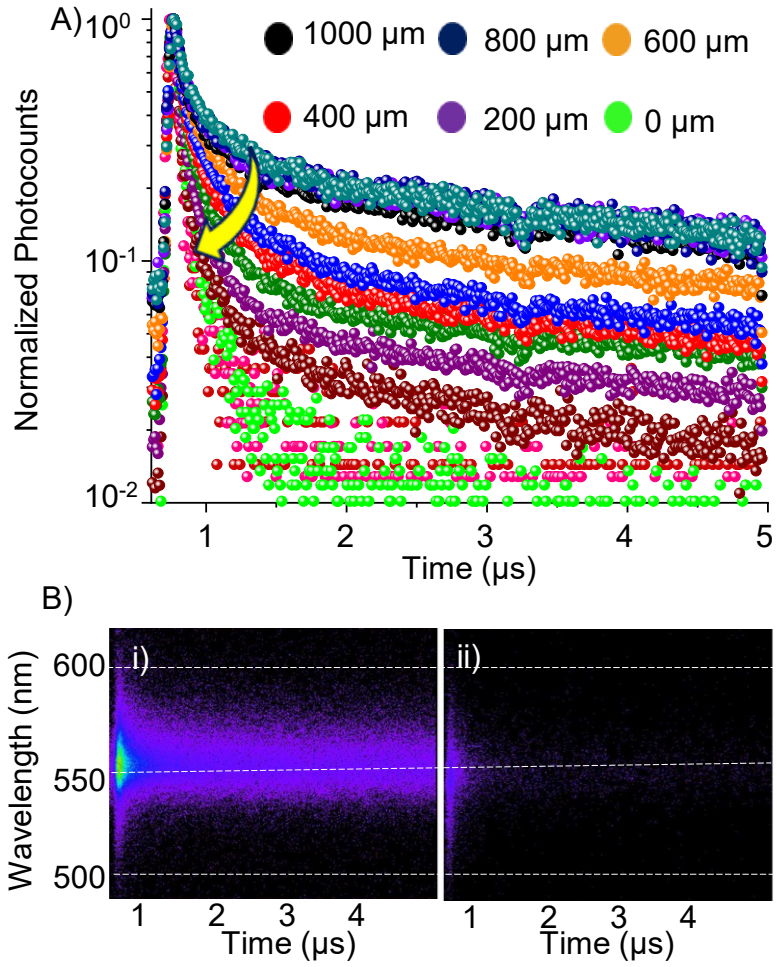

Figure 3.10. (A) Distance-dependent PL decay profiles of a $FAPbBr_3$:C_{60} heterojunction film and the corresponding photocount maps at (i) 1000 µm and (ii) 0 µm from the interface.

the discussions given in the previous section, I consider the early excitons split into free carriers, and their migration lowers the recombination rates. The efficient electron transfer at the interfaces causes a decrease in the PL lifetimes, where the acceptors (C_{60}/TiO_2) act as non-radiative recombination centers.

To obtain more insight into this distance-dependent diffusion and scavenging of photogenerated electrons above, below, and at the interface, I plotted photocounts or lifetimes against the distance from the $FAPbBr_3$ PNC-only region to the interface [Figures 3.12A ($FAPbBr_3$:C_{60}) and B ($FAPbBr_3$:TiO_2)]. The major outcomes of this chapter can be described by combining the different charge carrier properties of PNCs in films and solutions. In the case of films, closely packed self-assembly induces a large dielectric constant and low exciton binding energy. The films are characterized by STEM imaging, which shows close-packed PNCs even at sub-nanometer thickness prepared on TEM grids. The electron's mean-free path

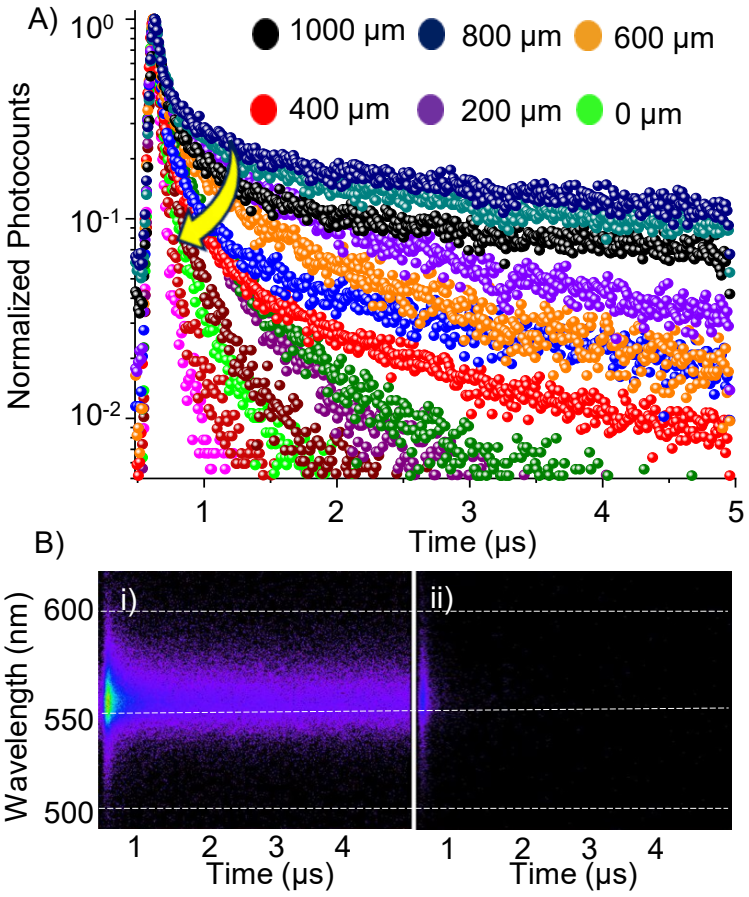

Figure 3.11. (A) Distance-dependent PL decay profiles of a $FAPbBr_3$:TiO_2 heterojunction film and the corresponding photocount maps at (i) 1000 µm and (ii) 0 µm from the interface.

in perovskite generally ranges within 10's of nm, and electron delocalization and hole localization can occur. According to the obtained STEM images, the interparticle distance is 1.6 nm, comparable to the ligand length. These properties support the early exciton splitting and resultant free carriers to migrate in the films by hopping among the PNCs, lowering the recombination rates.

Figures 3.13A and B describe the long-range carrier diffusion in films and the adsorption of C_{60} molecules on isolated PNCs in a solution. This difference in carrier properties allowed us to evaluate films' distance-dependent electron transfer dynamics. In the heterojunction films of $FAPbBr_3$:C_{60}/ TiO_2, the electron transfer is distance-dependent (0 – 800 µm). However, the PL lifetimes become constant or intact for distances over 800 µm due to the dominant radiative recombination. Also, in the interface region, i.e., below 0 µm, negligibly small photocounts

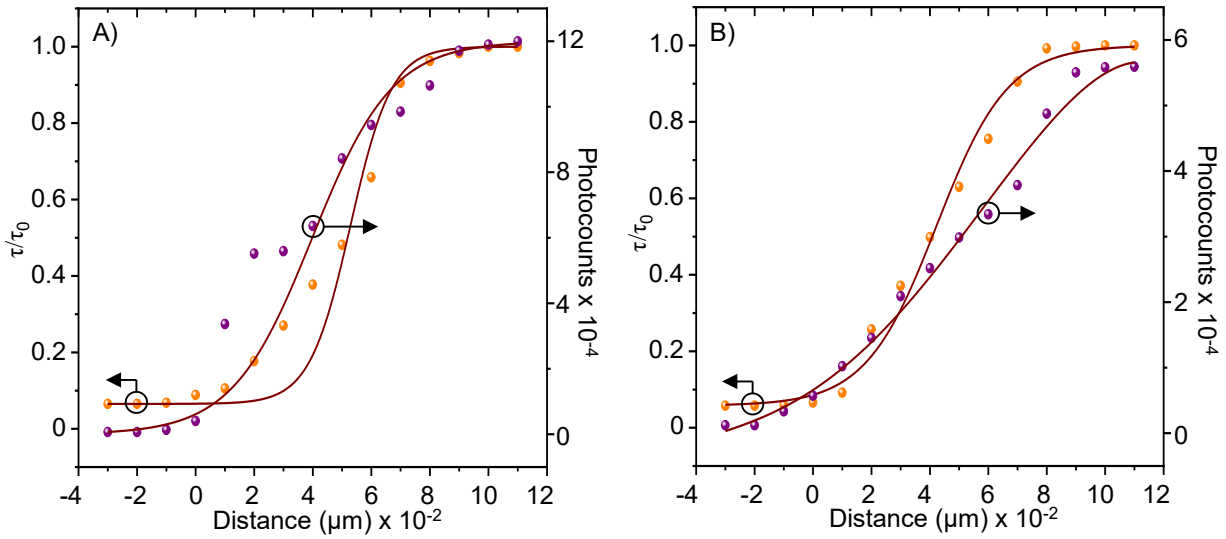

Figure 3.12. Distance-dependent carrier dynamics. The graphs of photocounts or PL lifetimes against the distance in heterojunction films of $FAPbBr_3$ with (A) C_{60} and (B) TiO_2. The lines represent sigmoidal fits.

and short PL lifetimes were observed. This is mainly due to the efficient capturing of free carriers by the acceptors (C_{60}/ TiO_2). A correlation between the charge carrier diffusion and interfacial electron transfer in the $FAPbBr_3$:TiO_2 and $FAPbBr_3$:C_{60} heterojunction films are represented in Figures 3.13C and D, respectively.

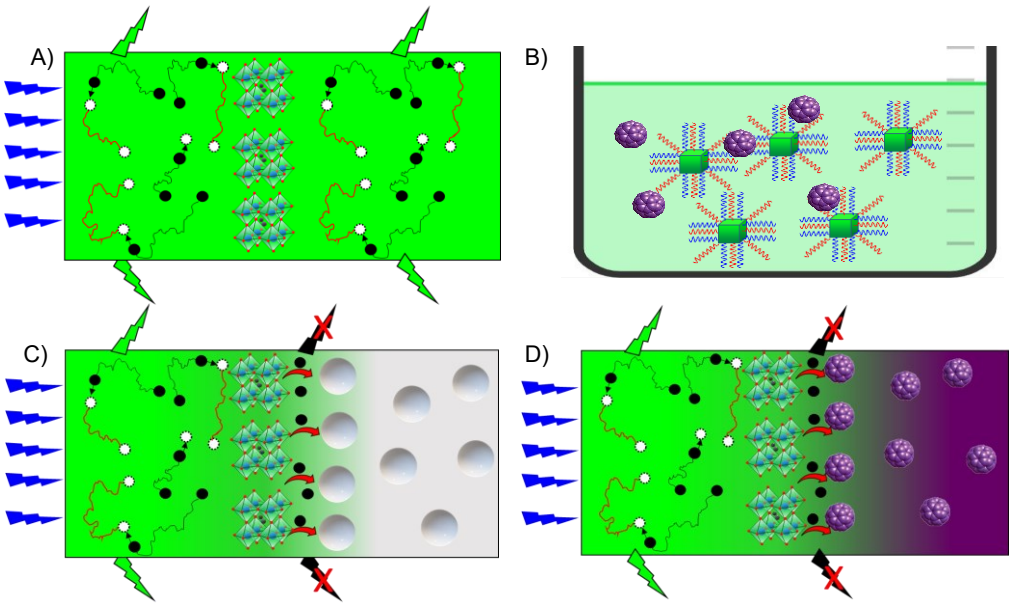

Figure 3.13. Schemes of charge carrier dynamics in (A) $FAPbBr_3$ film and interface films covered with (B) TiO_2 and (C) C_{60}.

3.2.5 Carrier diffusion mechanism and electron transfer dynamics

Generally, the halide perovskites are called defect tolerant materials, but the surface traps or halide vacancies cause major drawbacks. Specifically, these vacancies or shallow traps are the origins of non-radiative recombination, electron trapping (k_t), and de-trapping (k_{dt}) processes in PNCs.[59,60] In this chapter, I found that carrier diffusion and electron transfer dynamics dominated over rates of trapping or de-trapping, which is obvious from the above results. The arrangement of energy states in a single donor (PNC) and D-A (PNC:C_{60}) system in a solution is shown in Figure 3.14. On the one hand, in addition to the radiative processes (k_r), non-radiative recombination (k_{nr}) should also be considered alongside [(due to the presence of trap

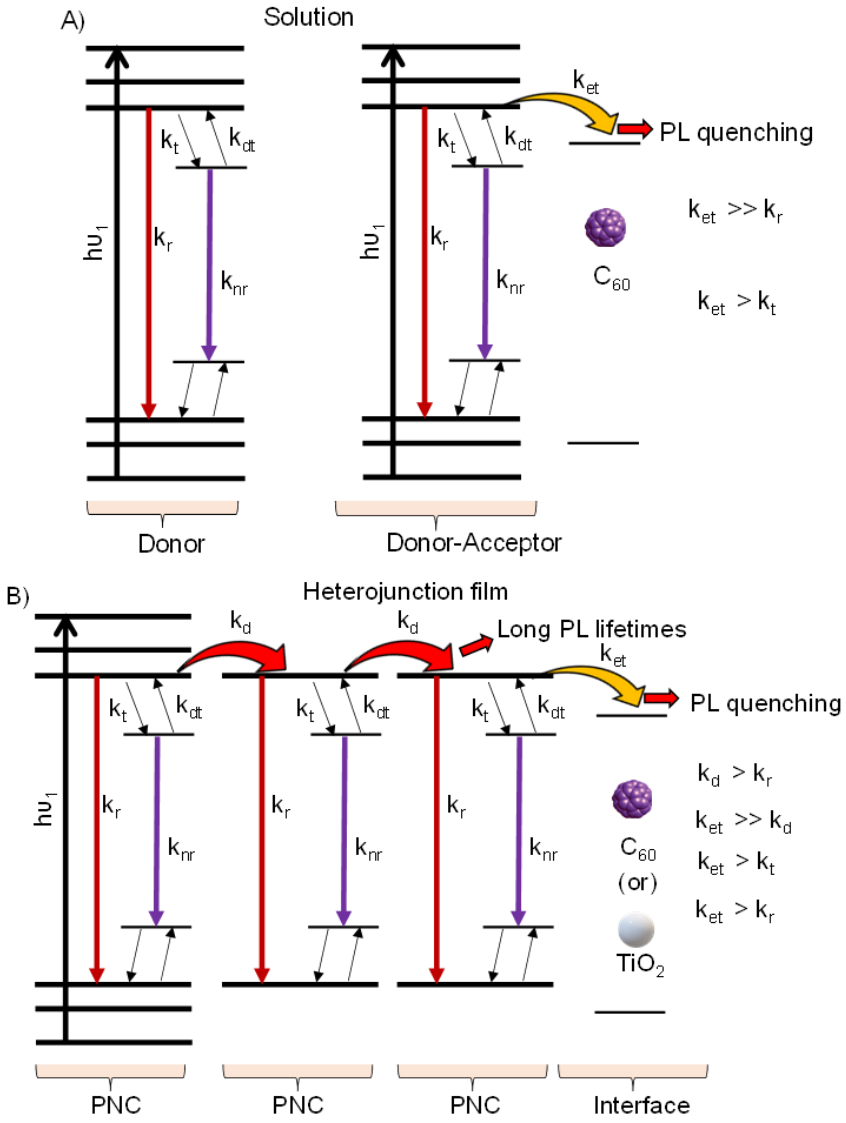

Figure 3.14. Schemes of electron transfer dynamics in (A) D-A system in a solution and (B) an interface-film overlaid with TiO_2/C_{60}.

states, hot electrons, and deep hole generation (k_t, k_{dt})]. On the other hand, the electron transfer rate (k_{et}) is expected to be higher than this k_r or k_{nr} in the D-A system ($k_{et}>>k_t/k_{dt}$), where a C_{60} adsorbed onto the hydrophobic PNC surface acts as a non-radiative recombination center. The closely-packed PNC film with C_{60}/TiO_2 interface is shown in Figure 3.14B, which illustrates the carrier diffusion (k_d) and k_{et} processes dominating the k_r and k_t/k_{dt}. In this case, a PNCs film supports the diffusion of charge carriers among closely packed PNCs. Thus, the recombination rates become lower in the film than in a solution, resulting in long PL lifetimes ($k_d>k_r$).[61-63] Conversely, at and near the interface, k_{et} dominates over the k_d.

3.3 Conclusions

While lead halide perovskites are exciting materials for photovoltaic and optoelectronic devices, the potential applications of ligand-assisted self-assembly and close-packed PNCs to various devices are yet to be explored. In this chapter, I summarized the long-range carrier migration and interfacial electron transfer in D-A systems. I found longer PL lifetimes for PNCs in a film than in a solution, indicating the long-range diffusion of photogenerated carriers among PNCs. On the other hand, adsorption of C_{60} molecules onto the hydrophobic surface of PNCs in a solution resulted in the PL quenching with constant PL lifetime values at all acceptor concentrations, suggesting a static electron transfer. The interfacial electron transfer was obvious from forming the C_{60} anion radical. Interestingly, as I moved the pump-probe region towards the interface in a D-A film, at every 100 μm distance, the PL lifetime decreased gradually and became saturated near the interface. Therefore, the interfacial electron transfer is distance-dependent, evident from a decrease in the PL lifetime by moving the carrier generation center towards the interface. I believe this study about thin films and distance-dependent carrier capturing enables one to improve the electronic and photovoltaic applications of PSCs.

References

1. Jeon, N. J.; Noh, J. H.; Yang, W. S.; Kim, Y. C.; Ryu, S.; Seo, J.; Seok, S. Il. Compositional Engineering of Perovskite Materials for High-Performance Solar Cells. *Nature* **2015**, *517*, 476–480.

2. Rhee, S.; An, K.; Kang, K. T. Recent Advances and Challenges in Halide Perovskite Crystals in Optoelectronic Devices from Solar Cells to Other Applications. *Crystals* **2021**, *11*, 39.

3. Chouhan, L.; Ghimire, S.; Subrahmanyam, C.; Miyasaka, T.; Biju, V. Synthesis, Optoelectronic Properties and Applications of Halide Perovskites. *Chem. Soc. Rev.* **2020**, *49*, 2869–2885.

4. Kovalenko, M. V.; Protesescu, L.; Bodnarchuk, M. I. Properties and Potential Optoelectronic Applications of Lead Halide Perovskite Nanocrystals. *Science* **2017**, *358*, 745–750.

5. Li, X.; Bi, D.; Yi, C.; Décoppet, J. D.; Luo, J.; Zakeeruddin, S. M.; Hagfeldt, A.; Grätzel, M. A Vacuum Flash-Assisted Solution Process for High-Efficiency Large-Area Perovskite Solar Cells. *Science* **2016**, *353*, 58–62.

6. Liu, M.; Johnston, M. B.; Snaith, H. J. Efficient Planar Heterojunction Perovskite Solar Cells by Vapour Deposition. *Nature* **2013**, *501*, 395–398.

7. Bi, E.; Chen, H.; Xie, F.; Wu, Y.; Chen, W.; Su, Y.; Islam, A.; Grätzel, M.; Yang, X.; Han, L. Diffusion Engineering of Ions and Charge Carriers for Stable Efficient Perovskite Solar Cells. *Nat. Commun.* **2017**, *8*, 15330.

8. An, Y.; Hidalgo, J.; Perini, C. A. R.; Castro-Méndez, A.-F.; Vagott, J. N.; Bairley, K.; Wang, S.; Li, X.; Correa-Baena, J.-P. Structural Stability of Formamidinium- and Cesium-Based Halide Perovskites. *ACS Energy Lett.* **2021**, *6*, 1942–1969.

9. Alcocer, M. J. P.; Leijtens, T.; Herz, L. M.; Petrozza, A.; Snaith, H. J. Electron-Hole Diffusion Lengths Exceeding Trihalide Perovskite Absorber. *Science* **2013**, *342*, 341–344.

10. Fan, P.; Gu, D.; Liang, G. X.; Luo, J. T.; Chen, J. L.; Zheng, Z. H.; Zhang, D. P. High-Performance Perovskite $CH_3NH_3PbI_3$ Thin Films for Solar Cells Prepared by Single-Source Physical Vapour Deposition. *Sci. Rep.* **2016**, *6*, 29910.

11. Zhumekenov, A. A.; Saidaminov, M. I.; Haque, M. A.; Alarousu, E.; Sarmah, S. P.; Murali, B.; Dursun, I.; Miao, X. H.; Abdelhady, A. L.; Wu, T.; Mohammed, O. F.; Bakr, O. M. Formamidinium Lead Halide Perovskite Crystals with Unprecedented Long Carrier Dynamics and Diffusion Length. *ACS Energy Lett.* **2016**, *1*, 32–37.

12. Chen, J.; Park, N. G. Materials and Methods for Interface Engineering toward Stable and Efficient Perovskite Solar Cells. *ACS Energy Lett.* **2020**, *5*, 2742–2786.

13. Jiménez-López, J.; Puscher, B. M. D.; Guldi, D. M.; Palomares, E. Improved Carrier Collection and Hot Electron Extraction across Perovskite, C_{60}, and TiO_2 Interfaces. *J. Am. Chem. Soc.* **2020**, *142*, 1236–1246.

14. Zhou, S.; Zhou, G.; Li, Y.; Xu, X.; Hsu, Y. J.; Xu, J.; Zhao, N.; Lu, X. Understanding Charge Transport in All-Inorganic Halide Perovskite Nanocrystal Thin-Film Field Effect Transistors. *ACS Energy Lett.* **2020**, *5*, 2614–2623.

15. Clinckemalie, L.; Valli, D.; Roeffaers, M. B. J.; Hofkens, J.; Pradhan, B.; Debroye, E. Challenges and Opportunities for $CsPbBr_3$ Perovskites in Low- and High-Energy Radiation Detection. *ACS Energy Lett.* **2021**, *6*, 1290–1314.

16. Jeon, I.; Ueno, H.; Seo, S.; Aitola, K.; Nishikubo, R.; Saeki, A.; Okada, H.; Boschloo, G.; Maruyama, S.; Matsuo, Y. Lithium-Ion Endohedral Fullerene ($Li^+@C_{60}$) Dopants in Stable Perovskite Solar Cells Induce Instant Doping and Anti-Oxidation. *Angew. Chem. Int. Ed.* **2018**, *57*, 4607–4611.

17. Wang, H.; Rahaq, Y.; Kumar, V. A Composite Light-Harvesting Layer from Photoactive Polymer and Halide Perovskite for Planar Heterojunction Solar Cells. *Sci. Rep.* **2016**, *6*, 29567.

18. Schulz, P. Interface Design for Metal Halide Perovskite Solar Cells. *ACS Energy Lett.* **2018**, *3*, 1287–1293.

19. Litvin, A. P.; Zhang, X.; Berwick, K.; Fedorov, A. V.; Zheng, W.; Baranov, A. V. Carbon-Based Interlayers in Perovskite Solar Cells. *Renew. Sustain. Energy Rev.* **2020**, *124*, 109774.

20. Gil-Escrig, L.; Dreessen, C.; Palazon, F.; Hawash, Z.; Moons, E.; Albrecht, S.; Sessolo, M.; Bolink, H. J. Efficient Wide-Bandgap Mixed-Cation and Mixed-Halide Perovskite Solar Cells by Vacuum Deposition. *ACS Energy Lett.* **2021**, *6*, 827–836.

21. Li, Y.; Wu, F.; Han, M.; Li, Z.; Zhu, L.; Li, Z. Merocyanine with Hole-Transporting Ability and Efficient Defect Passivation Effect for Perovskite Solar Cells. *ACS Energy Lett.* **2021**, *6*, 869–876.

22. Guo, Z.; Manser, J. S.; Wan, Y.; Kamat, P. V.; Huang, L. Spatial and Temporal Imaging of Long-Range Charge Transport in Perovskite Thin Films by Ultrafast Microscopy. *Nat. Commun.* **2015**, *6*, 7471.

23. Dey, A.; Ye, J.; De, A.; Debroye, E.; Ha, S. K.; Bladt, E.; Kshirsagar, A. S.; Wang, Z.; Yin, J.; Wang, Y. *et al.* State of the Art and Prospects for Halide Perovskite Nanocrystals. *ACS Nano* **2021**, *15*, 10775–10981.

24. Jeong, J.; Kim, M.; Seo, J.; Lu, H.; Ahlawat, P.; Mishra, A.; Yang, Y.; Hope, M. A.; Eickemeyer, F. T.; Kim, M.; Yoon, Y. J.; Choi, I. W.; Darwich, B. P.; Choi, S. J.; Jo, Y.; Lee, J. H.; Walker, B.; Zakeeruddin, S. M.; Emsley, L.; Rothlisberger, U.; Hagfeldt, A.; Kim, D. S.; Grätzel, M.; Kim, J. Y. Pseudo-Halide Anion Engineering for α-FAPbI3 Perovskite Solar Cells. *Nature* **2021**, *592*, 381–385.

25. Guo, Z.; Zhou, N.; Williams, O. F.; Hu, J.; You, W.; Moran, A. M. Imaging Carrier Diffusion in Perovskites with a Diffractive Optic-based Transient Absorption Microscope. *J. Phys. Chem. C* **2018**, *122*, 10650–10656.

26. Tian, C.; Wang, F.; Wang, Y.; Yang, Z.; Chen, X.; Mei, J.; Liu, H.; Zhao, D. Chemical Vapor Deposition Method Grown All-Inorganic Perovskite Microcrystals for Self-Powered Photodetectors. *ACS Appl. Mater. Interfaces* **2019**, *11*, 15804–15812.

27. He, H.; Yu, Q.; Li, H.; Li, J.; Si, J.; Jin, Y.; Wang, N.; Wang, J.; He, J.; Wang, X.; Zhang, Y.; Ye, Z. Exciton Localization in Solution-Processed Organolead Trihalide Perovskites. *Nat. Commun.* **2016**, *7*, 10896.

28. Miyata, A.; Mitioglu, A.; Plochocka, P.; Portugall, O.; Wang, J. T. W.; Stranks, S. D.; Snaith, H. J.; Nicholas, R. J. Direct Measurement of the Exciton Binding Energy and

Effective Masses for Charge Carriers in Organic-Inorganic Tri-Halide Perovskites. *Nat. Phys.* **2015**, *11*, 582–587.

29. Zhai, Y.; Wang, K.; Zhang, F.; Xiao, C.; Rose, A. H.; Zhu, K.; Beard, M. C. Individual Electron and Hole Mobilities in Lead-Halide Perovskites Revealed by Noncontact Methods. *ACS Energy Lett.* **2020**, *5*, 47–55.

30. Qiao, T.; Son, D. H. Synthesis and Properties of Strongly Quantum-Confined Cesium Lead Halide Perovskite Nanocrystals. *Acc. Chem. Res.* **2021**, *54*, 1399–1408.

31. Bhatia, H.; Steele, J. A.; Martin, C.; Keshavarz, M.; Solis-Fernandez, G.; Yuan, H.; Fleury, G.; Huang, H.; Dovgaliuk, I.; Chernyshov, D.; Hendrix, J.; Roeffaers, M. B. J.; Hofkens, J.; Debroye, E. Single-Step Synthesis of Dual Phase Bright Blue-Green Emitting Lead Halide Perovskite Nanocrystal Thin Films. *Chem. Mater.* **2019**, *31*, 6824–6832.

32. Brennan, M. C.; Forde, A.; Zhukovskyi, M.; Baublis, A. J.; Morozov, Y. V.; Zhang, S.; Zhang, Z.; Kilin, D. S.; Kuno, M. Universal Size-Dependent Stokes Shifts in Lead Halide Perovskite Nanocrystals. *J. Phys. Chem. Lett.* **2020**, *11*, 4937–4944.

33. Caselli, V. M.; Wei, Z.; Ackermans, M. M.; Hutter, E. M.; Ehrler, B.; Savenije, T. J. Charge Carrier Dynamics upon Sub-Bandgap Excitation in Methylammonium Lead Iodide Thin Films: Effects of Urbach Tail, Deep Defects, and Two-Photon Absorption. *ACS Energy Lett.* **2020**, *5*, 3821–3827.

34. Ledinsky, M.; Schönfeldová, T.; Holovský, J.; Aydin, E.; Hájková, Z.; Landová, L.; Neyková, N.; Fejfar, A.; De Wolf, S. Temperature Dependence of the Urbach Energy in Lead Iodide Perovskites. *J. Phys. Chem. Lett.* **2019**, *10*, 1368–1373.

35. Shi, D.; Adinolfi, V.; Comin, R.; Yuan, M.; Alarousu, E.; Buin, A.; Chen, Y.; Hoogland, S.; Rothenberger, A.; Katsiev, K.; Losovyj, Y.; Zhang, X.; Dowben, P. A.; Mohammed, O. F.; Sargent, E. H.; Bakr, O. M. Low Trap-State Density and Long Carrier Diffusion in Organolead Trihalide Perovskite Single Crystals. *Science* **2015**, *347*, 519–522.

36. Wu, S. H.; Lin, M. Y.; Chang, S. H.; Tu, W. C.; Chu, C. W.; Chang, Y. C. A Design Based on a Charge-Transfer Bilayer as an Electron Transport Layer for Improving the Performance and Stability in Planar Perovskite Solar Cells. *J. Phys. Chem. C* **2018**, *122*, 236–244.

37. Wu, K.; Liang, G.; Shang, Q.; Ren, Y.; Kong, D.; Lian, T. Ultrafast Interfacial Electron and Hole Transfer from $CsPbBr_3$ Perovskite Quantum Dots. *J. Am. Chem. Soc.* **2015**, *137*, 12792–12795.

38. Yang, D.; Zhang, X.; Wang, K.; Wu, C.; Yang, R.; Hou, Y.; Jiang, Y.; Liu, S.; Priya, S. Stable Efficiency Exceeding 20.6% for Inverted Perovskite Solar Cells through Polymer-Optimized PCBM Electron-Transport Layers. *Nano Lett.* **2019**, *19*, 3313–3320.

39. Nair, V. C.; Muthu, C.; Rogach, A. L.; Kohara, R.; Biju, V. Channeling Exciton Migration into Electron Transfer in Formamidinium Lead Bromide Perovskite Nanocrystal/Fullerene Composites. *Angew. Chem. Int. Ed.* **2017**, *56*, 1214–1218.

40. Imahori, H.; Tamaki, K.; Guldi, D. M.; Luo, C.; Fujitsuka, M.; Ito, O.; Sakata, Y.; Fukuzumi, S. Modulating Charge Separation and Charge Recombination Dynamics in Porphyrin-Fullerene Linked Dyads and Triads: Marcus-Normal versus Inverted Region. *J. Am. Chem. Soc.* **2001**, *123*, 2607–2617.

41. Chueh, C. C.; Li, C. Z.; Jen, A. K. Y. Recent Progress and Perspective in Solution-Processed Interfacial Materials for Efficient and Stable Polymer and Organometal Perovskite Solar Cells. *Energy Environ. Sci.* **2015**, *8*, 1160–1189.

42. Tong, Y. L.; Zhang, Y. W.; Ma, K.; Cheng, R.; Wang, F.; Chen, S. One-Step Synthesis of FA-Directing $FAPbBr_3$ Perovskite Nanocrystals toward High-Performance Display. *ACS Appl. Mater. Interfaces* **2018**, *10*, 31603–31609.

43. Golubev, T.; Liu, D.; Lunt, R.; Duxbury, P. Understanding the Impact of C_{60} at the Interface of Perovskite Solar Cells via Drift-Diffusion Modeling. *AIP Adv.* **2019**, *9*, 035026.

44. Credgington, D.; Jamieson, F. C.; Walker, B.; Nguyen, T. Q.; Durrant, J. R. Quantification of Geminate and Non-Geminate Recombination Losses within a Solution-Processed Small-Molecule Bulk Heterojunction Solar Cell. *Adv. Mater.* **2012**, *24*, 2135–2141.

45. Lee, S. W.; Kim, S.; Bae, S.; Cho, K.; Chung, T.; Mundt, L. E.; Lee, S.; Park, S.; Park, H.; Schubert, M. C.; Glunz, S. W.; Ko, Y.; Jun, Y.; Kang, Y.; Lee, H. S.; Kim, D. UV Degradation and Recovery of Perovskite Solar Cells. *Sci. Rep.* **2016**, *6*, 38150.

46. Deng, Y.; Peng, E.; Shao, Y.; Xiao, Z.; Dong, Q.; Huang, J. Scalable Fabrication of Efficient Organolead Trihalide Perovskite Solar Cells with Doctor-Bladed Active Layers. *Energy Environ. Sci.* **2015**, *8*, 1544–1550.

47. Sherkar, T. S.; Momblona, C.; Gil-Escrig, L.; Ávila, J.; Sessolo, M.; Bolink, H. J.; Koster, L. J. A. Recombination in Perovskite Solar Cells: Significance of Grain Boundaries, Interface Traps, and Defect Ions. *ACS Energy Lett.* **2017**, *2*, 1214–1222.

48. Wojciechowski, K.; Leijtens, T.; Siprova, S.; Schlueter, C.; Hörantner, M. T.; Wang, J. T. W.; Li, C. Z.; Jen, A. K. Y.; Lee, T. L.; Snaith, H. J. C_{60} as an Efficient N-Type Compact Layer in Perovskite Solar Cells. *J. Phys. Chem. Lett.* **2015**, *6*, 2399–2405.

49. Long, R.; Fang, W. H.; Prezhdo, O. V. Strong Interaction at the Perovskite/TiO_2 Interface Facilitates Ultrafast Photoinduced Charge Separation: A Nonadiabatic Molecular Dynamics Study. *J. Phys. Chem. C* **2017**, *121*, 3797–3806.

50. Chen, C.; Jiang, Y.; Guo, J.; Wu, X.; Zhang, W.; Wu, S.; Gao, X.; Hu, X.; Wang, Q.; Zhou, G.; Chen, Y.; Liu, J. M.; Kempa, K.; Gao, J. Solvent-Assisted Low-Temperature Crystallization of SnO_2 Electron-Transfer Layer for High-Efficiency Planar Perovskite Solar Cells. *Adv. Funct. Mater.* **2019**, *29*, 1–9.

51. Xu, C.; Zhang, Y.; Luo, P.; Sun, J.; Wang, H.; Lu, Y. W.; Ding, F.; Zhang, C.; Hu, J. Comparative Study on TiO_2 and C_{60} Electron Transport Layers for Efficient Perovskite Solar Cells. *ACS Appl. Energy Mater.* **2021**, *4*, 5543–5553.

52. Zhang, L.; Reddy, M. A.; Gao, P.; Diemant, T.; Jürgen Behm, R.; Fichtner, M. Study of All Solid-State Rechargeable Fluoride Ion Batteries Based on Thin-Film Electrolyte. *J. Solid State Electrochem.* **2017**, *21*, 1243–1251.

53. Bera, S.; Pradhan, N. Perovskite Nanocrystal Heterostructures: Synthesis, Optical Properties, and Applications. *ACS Energy Lett.* **2020**, *5*, 2858–2872.

54. Chen, X.; Lu, H.; Li, Z.; Zhai, Y.; Ndione, P. F.; Berry, J. J.; Zhu, K.; Yang, Y.; Beard, M. C. Impact of Layer Thickness on the Charge Carrier and Spin Coherence Lifetime in Two-Dimensional Layered Perovskite Single Crystals. *ACS Energy Lett.* **2018**, *3*, 2273–2279.

55. Crothers, T. W.; Milot, R. L.; Patel, J. B.; Parrott, E. S.; Schlipf, J.; Müller-Buschbaum, P.; Johnston, M. B.; Herz, L. M. Photon Reabsorption Masks Intrinsic Bimolecular Charge-Carrier Recombination in $CH_3NH_3PbI_3$ Perovskite. *Nano Lett.* **2017**, *17*, 5782–5789.

56. Protesescu, L.; Yakunin, S.; Bodnarchuk, M. I.; Krieg, F.; Caputo, R.; Hendon, C. H.; Yang, R. X.; Walsh, A.; Kovalenko, M. V. Nanocrystals of Cesium Lead Halide Perovskites ($CsPbX_3$, X = Cl, Br, and I): Novel Optoelectronic Materials Showing Bright Emission with Wide Color Gamut. *Nano Lett.* **2015**, *15*, 3692–3696.

57. Ghimire, S.; Nair, V. C.; Muthu, C.; Yuyama, K.; Vacha, M.; Biju, V. Photoinduced Photoluminescence Enhancement in Self-Assembled Clusters of Formamidinium Lead Bromide Perovskite Nanocrystals. *Nanoscale* **2019**, *11*, 9335–9340.

58. Quaranta, A.; Qu, H.; Vencel, T.; Zhang, Y.; Leibl, W.; Leach, S.; Bensasson, R. V. Photophysical Properties in Aqueous Solutions of C_{60} Embedded in 2:1 γ-Cyclodextrin/ [60] Fullerene Inclusion Complexes. *Chem. Phys. Lett.* **2014**, *614*, 234–237.

59. Biju, V.; Chouhan, L.; Ito, S.; Thomas, E. M.; Takano, Y.; Ghimire, S.; Miyasaka, H. Real-Time Blinking Suppression of Perovskite Quantum Dots by Halide Vacancy Filling. *ACS Nano* **2021**, *15*, 2831–2838.

60. Sachith, B. M.; Okamoto, T.; Ghimire, S.; Umeyama, T.; Takano, Y.; Imahori, H.; Biju, V. Long-Range Interfacial Charge Carrier Trapping in Halide Perovskite-C_{60} and Halide Perovskite-TiO_2 Donor-Acceptor Films. *J. Phys. Chem. Lett.* **2021**, 12, 8644–8651.

61. Rehman, W.; Milot, R. L.; Eperon, G. E.; Wehrenfennig, C.; Boland, J. L.; Snaith, H. J.; Johnston, M. B.; Herz, L. M. Charge-Carrier Dynamics and Mobilities in Formamidinium Lead Mixed-Halide Perovskites. *Adv. Mater.* **2015**, *27*, 7938–7944.

62. Ghimire, S.; Chouhan, L.; Takano, Y.; Takahashi, K.; Nakamura, T.; Yuyama, K.; Biju, V. Amplified and Multicolor Emission from Films and Interfacial Layers of Lead Halide Perovskite Nanocrystals. *ACS Energy Lett.* **2019**, *4*, 133–141.

63. Trinh, C. T.; Minh, D. N.; Ahn, K. J.; Kang, Y.; Lee, K. G. Organic-Inorganic $FAPbBr_3$ Perovskite Quantum Dots as a Quantum Light Source: Single-Photon Emission and Blinking Behaviors. *ACS Photonics* **2018**, *5*, 4937–4943.

Chapter 4

Photoinduced electron transfer in single-particle donor-acceptor systems

Abstract

Halide perovskite nanocrystals are promising materials for energy harvesting and light-emitting applications. While the perovskite-based electron donor-acceptor interfaces offer unique control of the optical bandgap throughout the visible region of the electromagnetic spectrum, nonradiative losses adversely affect the charge injection efficiency. Thus, electron D-A systems composed of perovskite nanocrystals receive considerable attention. In this chapter, to understand the electron transfer dynamics in perovskite D-A systems, I demonstrate the real-time electron transfer of single perovskite nanocrystals treated with acceptors such as tetracyanobenzene (TCNB) and tetracyanoquinodimethane (TCNQ) molecules. The calculated negative Gibbs free energy change values of electron transfer for these electron acceptors suggest the feasibility of the electron transfer. I synthesize $CsPbBr_3$ by the hot-injection method and $MAPbBr_3$ with or without ligands by the ligand-assisted reprecipitation and spray techniques. At first, the photoluminescence quenching experiments are performed using fluorescence spectroscopy. The acceptors quench the PL intensity of the perovskite nanocrystals, accompanied by decreases in the PL lifetimes in solutions. The photoinduced electron transfer and charge separation are confirmed from the formation of the long-living radical anion of TCNQ. Statistical analyses of 450 or more single perovskite nanocrystals reveal an increase in the OFF-time probability, which helps confirm the electron transfer.

4.1 Introduction

Lead halide perovskite nanocrystals (PNCs) are greatly attracted to solar cell devices due to their large absorption coefficient, excellent defect tolerance, wide and tunable photoluminescence (PL) color, long-range charge carrier diffusion, and high PL quantum yields.[1-15] The efficient extraction of photogenerated charge carriers from PNCs is essential for perovskite solar cells (PSCs). This can be achieved by preparing electron donor-acceptor (D-A) systems by controlling the free energy change of electron transfer and the bandgap of perovskites.[16] Photoinduced electron transfer (PET) and subsequent charge separation between electron donors and acceptors require much attention to enhance PSCs' power conversion efficiency (PCE). Historically, PET in solar cells has been realized with various electron acceptors, including TiO_2, SnO_2, TCNB, TCNQ, and fullerene (C_{60}) derivatives such as [6,6]-phenyl C_{61} butyric acid methyl ester (PCBM)-C_{61}, and PCBM-C_{71}.[17-25] Especially, TCNQ and TCNB are the prominent strong electron acceptor molecules,[26,27] but less explored as the hole transport materials in PSCs. The perovskite-based electron D-A system from these strong electron acceptors could be promising for PSCs. However, the electron transfer rate and its dynamics need exploration.

Recently, the electron D-A systems made of TCNQ/TCNB have received considerable attention because of their high electron affinities. For example, Hye *et al*.[28] used TCNQ as an electron scavenger in photoelectrochemical studies and reported the rapid electron transfer from an electrode to TCNQ. Here the electron transfer was studied based on *in-situ* spectro-electrochemical methods. Chang *et al*.[29] prepared a layer-by-layer graphene/TCNQ anode for organic solar cells, where TCNQ molecules were tethered between two graphene layers. The strong electron affinity of TCNQ helped in achieving a high PCE and became attractive for next-generation solar cells. In a comparable study, Yoshiyuki *et al*.[30] successfully measured the electron transfer for CdTe nanocrystal/TCNB D-A system using steady-state and time-resolved PL spectroscopy. They observed PL quenching of CdTe nanocrystals by TCNB through static electron transfer. The above works explain the importance of TCNQ/TCNB as an electron scavenger. However, PET can differ for every single PNC in films, depending on their heterogeneity.[31] Therefore, understanding the electron transfer process at the single-particle level can provide further insights into the construction of efficient electron donor-acceptor (D-A) interfaces composed of halide perovskites.

The photoexcited state properties of single PNCs have been widely investigated concerning PL fluctuations (blinking). PL blinking is one of the most critical issues affecting the efficient capturing of electrons.[32] Generally, the bright state in the PNC blinking is called

the ON state, and the dark state is OFF. Two approaches have been widely accepted to understanding the PL blinking of PNCs: i) the charging/discharging model (type-A)[33] and ii) activation/deactivation of nonradiative recombination centers (type-B).[34] The ionized/charged state can initiate nonradiative Auger recombination processes (type-A blinking) *via* the flow of the exciton energy to a third carrier (either an electron or a hole).[35] In type-B blinking, the presence of multiple recombination centers causes PNC to undergo activation and deactivation mechanism. The shallow traps or short-lived traps in the bandgap, called multiple recombination centers, regulate the non-radiative recombination rates. The electrons trapped in the surface trap state can transfer to the electron acceptor at a heterojunction by channeling the neutralization of charged PNCs through the acceptor resulting in blinking suppression. Nevertheless, PL quenching occurred in most particles; for example, TiO_2 was used as an electron acceptor to suppress the PL blinking of CdSe/ZnS QDs.[36] The nonradiative carrier recombination in QDs was changed into electron transfer to TiO_2 nanoparticles, evident from the decrease in the PL intensity. Despite such examples, a high electron transfer rate for a PNC-based D-A interface can be valuable for developing next-generation PSC devices.

In this chapter, I reveal the dynamics and rates of electron transfer through the real-time blinking suppression and enhancement of single PNCs treated with TCNQ or TCNB molecules. At first, I confirmed the electron transfer feasibility by measuring steady-state absorption spectra, which evidenced the formation of TCNQ radical anion at 730 nm. Also, I calculated the Gibbs free energy change electron transfer for PNC-acceptor systems by measuring the oxidation and reduction potentials of the donors and acceptors. Later, I recorded the PL lifetime, PL intensity, and PL blinking trajectories of single PNCs before or after the treatment with TCNB/TCNQ. TCNB/TCNQ molecules quenched the PL intensities of PNCs accompanied by decreases in the PL lifetimes in a solution, revealing a dynamic electron transfer. I investigate the blinking of single PNCs before or after the treatment with TCNB/TCNQ. The blinking was suppressed in real-time; the PL intensity trajectory of a single PNC with TCNB shows a stable off-state, accompanied by rare PL blinking events, whereas a PNC with TCNQ showed long-living OFF and intermittent ON events. After analyzing several hundred single PNCs before or after treatment with TCNB/TCNQ, the ON/OFF-time probability distributions are summarized.

4.2 Results and discussion

4.2.1 Characterization of perovskite nanocrystals

The synthesis of colloidal $CsPbBr_3$ PNCs (C- PNCs) was carried out by a hot-injection technique. The hot-injection method provided C- PNCs in the cubic phase with uniform size distributions. The structural properties of pristine PNCs are characterized using TEM. PNCs solutions were drop-casted on copper grids and dried under a vacuum overnight. I analyzed the TEM images (Figure 4.1A) using imageJ software and estimated the size distribution of PNCs. The size of C- PNCs is estimated at 10.3 nm. The size distribution of >130 C- PNCs is shown in Figure 4.1B.

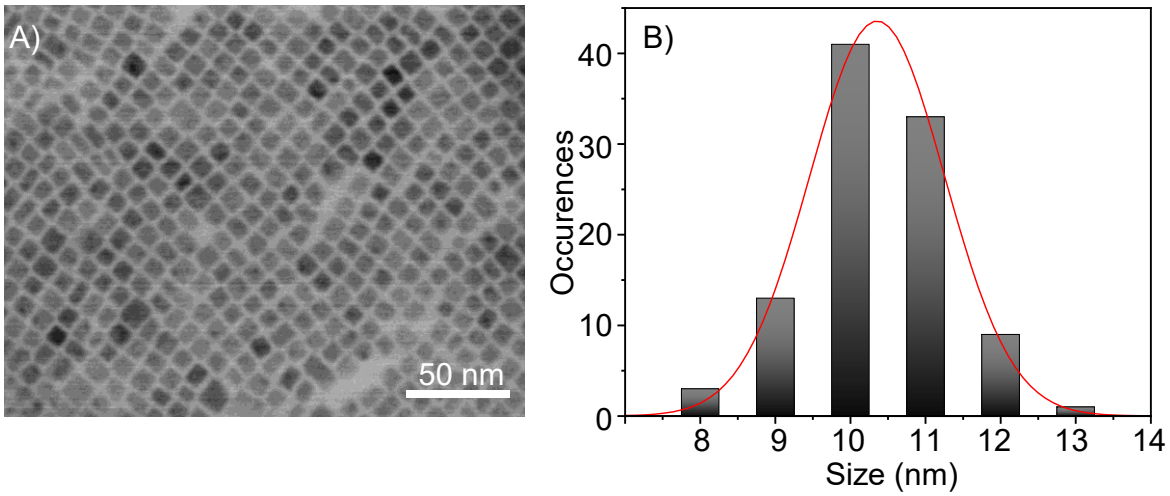

Figure 4.1. Structural characteristics of PNCs. (A) a TEM image and (B) the size distribution of C- PNCs.

The ligand-assisted reprecipitation (LARP) and modified spray techniques were employed to prepare $MAPbBr_3$ PNCs with (L- PNCs) or without ligand (W- PNCs), respectively. The detailed synthesis procedures are given in section 2.2.1. The LARP synthesis provided L- PNCs in the cubic phase with an edge length ca. 10.5 nm, whereas the modified spray method gives smaller W- PNCs with an average size ca. 6.4 nm. The TEM images these samples are shown in Figures 4.2A and 4.3A. Similarly, the imageJ software was employed to analyze the TEM images and finding the size distributions of L/W-PNCs (Figures 4.2B and 4.3B).

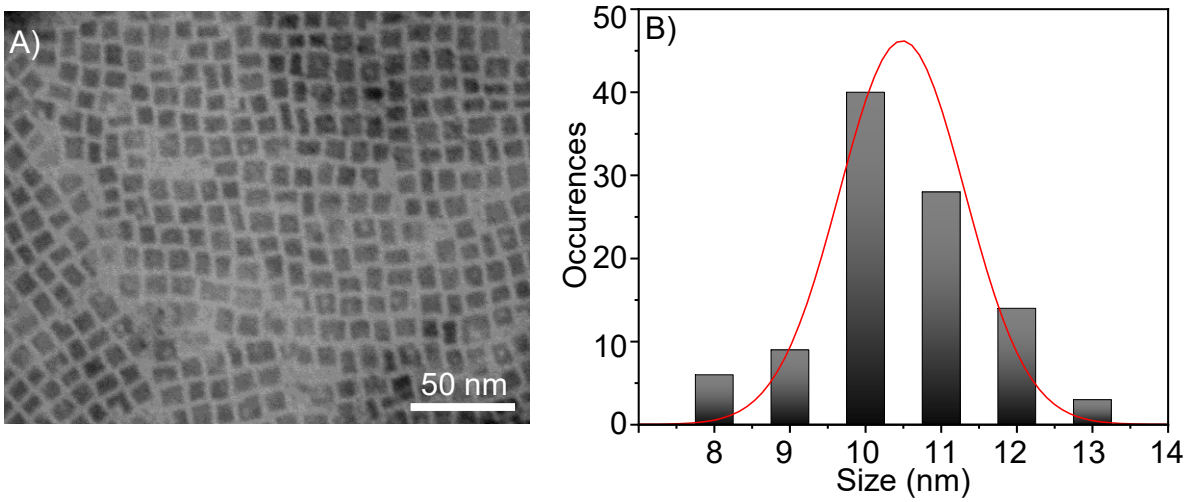

Figure 4.2. Structural characteristics of PNCs. (A) a TEM image and (B) the size distribution of L-PNCs.

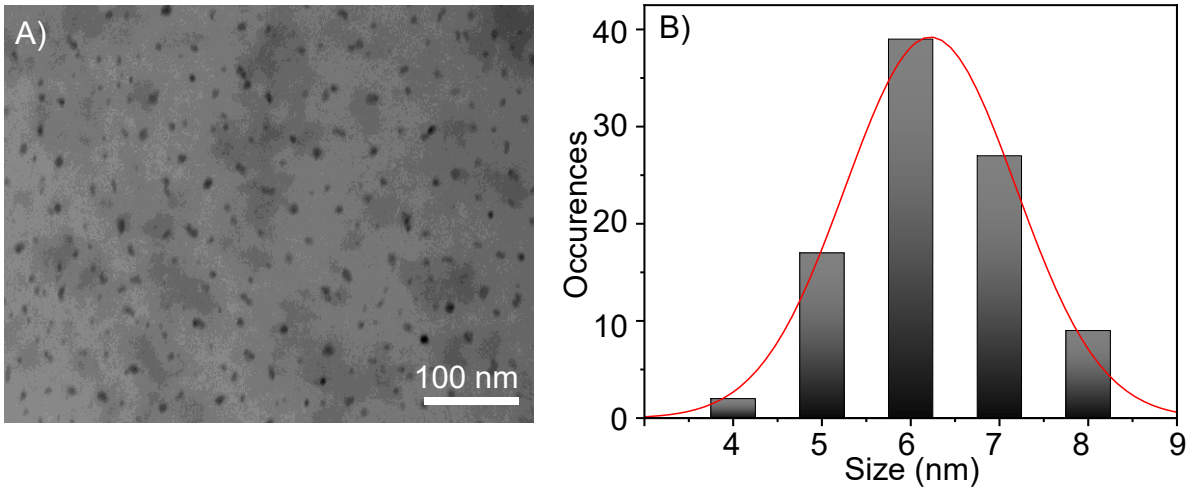

Figure 4.3. Structural characteristics of PNCs. (A) a TEM image and (B) the size distribution of W-PNCs.

The photophysical properties of PNCs are studied using UV-vis absorption and steady-state PL spectroscopy. Here, the PNCs were dispersed in toluene and diluted further. Figure 4.4 represents the UV-vis absorption and PL spectra of the PNCs samples in toluene (insets: images of the PNCs dispersed in toluene and taken under room or UV light). The absorption spectra are dominated by excitonic peaks ca. 510 nm for C-PNCs (Figure 4.4A) and 518 nm for L-PNCs (Figure 4.4B). The PL spectra show narrow full width at half maxima (*fwhm* 19 nm for C-PNCs, 23 nm for L-PNCs, and 16 nm for W-PNCs). The smaller *fwhm's* are consistent with their smaller sizes, and the Stokes shifts are mainly caused by the excitonic recombination.[37]

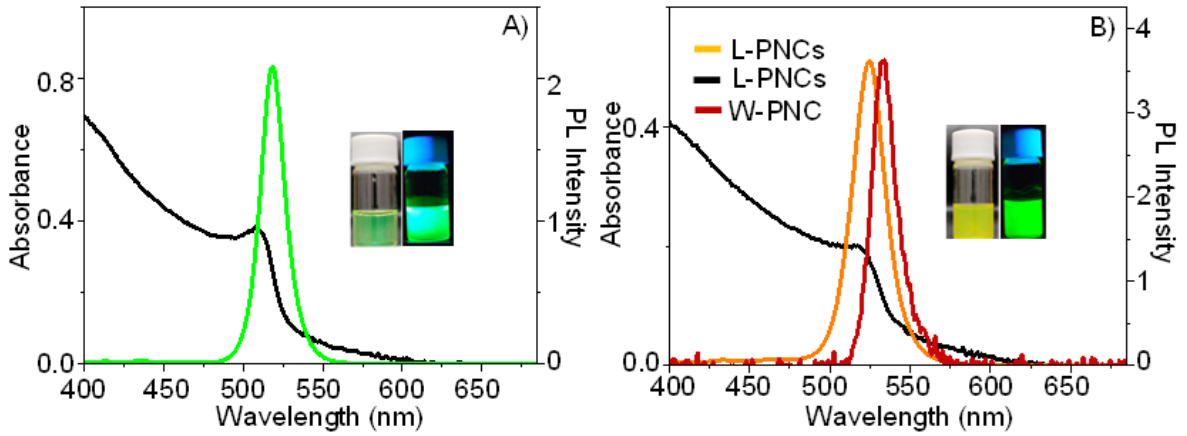

Figure 4.4. Optical properties of PNCs. (A) Absorption and PL spectra of C-PNCs dispersed in toluene and (B) L/W-PNCs (L-PNCs: orange and black. W-PNC: brown, λ_{ex}: 405 nm). Insets: the photographs of the PNCs solutions taken under the room light (left) or UV light (right).

4.2.2 Free energy change of electron transfer

The reaction-free energy (ΔG^o, Gibbs) change is crucial in determining the electron transfer rate.[38] To predict the feasibility of electron transfer from PNCs to TCNB/TCNQ, I estimated the free energy change using equation 1

$$\Delta G^0_{et} = E_{OX} - E_{RED} - E_{00} + C \quad (1)$$

where, E_{00} is the zero-zero transition energy, E_{OX} is the oxidation potential of the donor (C-PNCs or L-PNCs), E_{RED} is the reduction potential of the acceptor, and C is the work function. Nevertheless, the free energy change can be precisely estimated using equation 2, including the reorganization energy.

$$\Delta G^0_{et} = E_{OX} - E_{RED} - E_{00} + \frac{e2}{2}\left(\frac{1}{r_A} + \frac{1}{r_D} - \frac{2}{R_{cc}}\right)\left(\frac{1}{\epsilon_T} - \frac{1}{\epsilon_{REF}}\right) - \frac{e2}{\epsilon_{REF} R_{cc}} \quad (2)$$

r_A is the effective radius of TCNB (0.348 nm) or TCNQ (0.398 nm), r_D is the effective radius of the donor perovskite (L-PNC: 5.2 nm and C-PNC: 5 nm), R_{cc}, is the center-to-center distance between the ions, ε_T, and ε_{REF} are the dielectric constants of the solvents in which the electron transfer and redox properties are measured. I used the Rehm-Weller equation (equation 1), without the work function, to estimate the ΔG^0_{et} values. The oxidation (E_{OX}) and reduction

(E_{RED}) potentials were estimated by DPV measurements. From the DPV curves (Figure 4.5), the obtained E_{OX} values for C-PNCs and L-PNCs are 0.74 eV and 0.58 eV, the E_{RED} values for TCNQ and TCNB are estimated at -0.204 and -1.13 eV, respectively. The chemical structures of TCNB and TCNQ are shown in Figures 4.5E, F. The DPV data were collected for samples suspended/dissolved in tetrahydrofuran. I calculated the ΔG^0_{et} for L-PNCs/TCNQ and L-PNCs/TCNB at -1.11 eV and -0.12 eV, respectively. For C-PNCs/TCNQ and C-PNCs/TCNB systems, the calculated ΔG^0_{et} values are -1.16 eV and -0.17 eV, respectively. These results indicate the probability of PET from C-PNCs/ L-PNCs to TCNB/TCNQ.

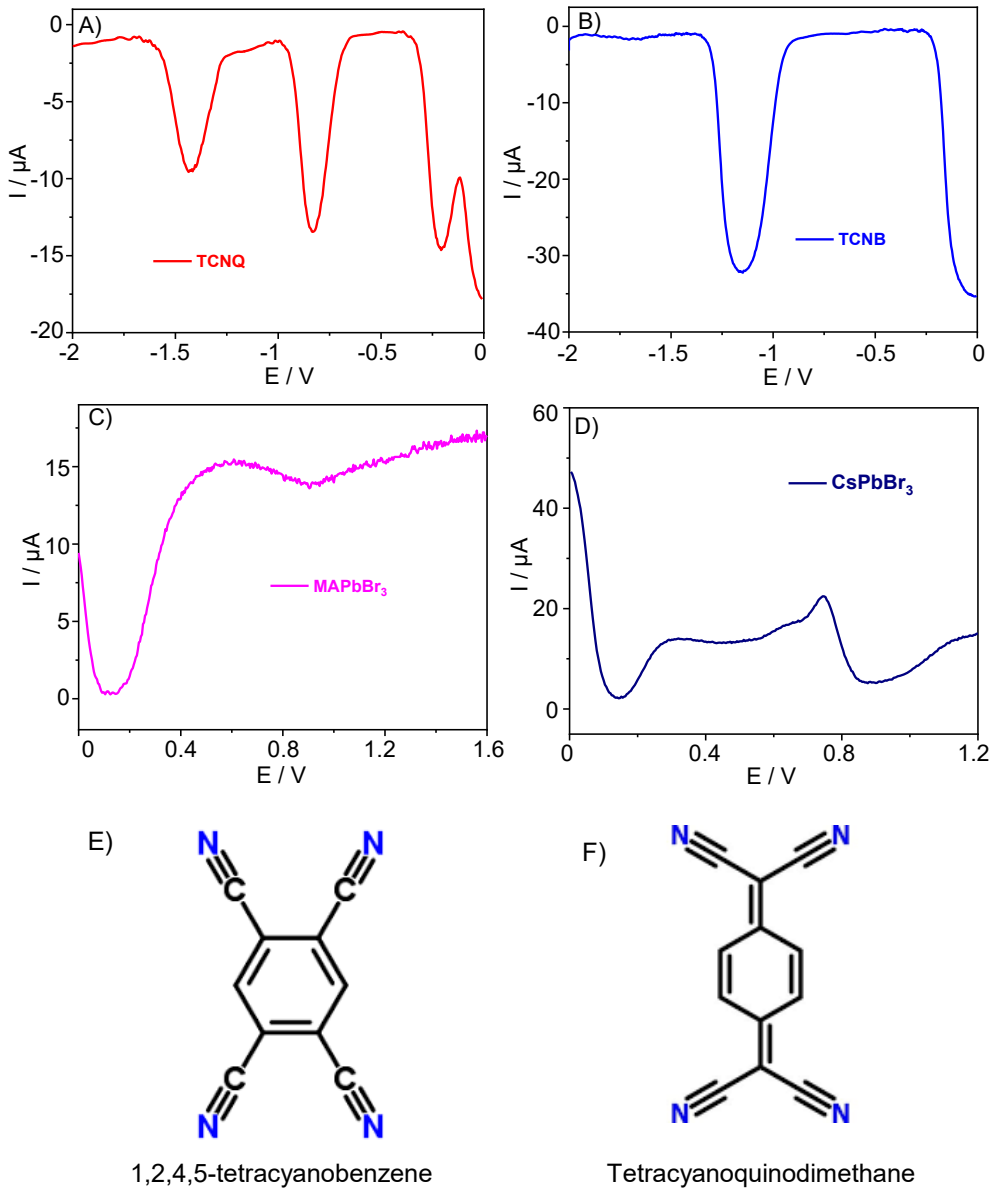

Figure 4.5. Redox potentials of donors and acceptors. DPV of (A) TCNQ (B) TCNB, (C) L-PNCs, and (D) C-PNCs. (E, F) The structures of TCNB and TCNQ.

4.2.3 Electron transfer dynamics in solutions

It is well-known that the TCNQ/TCNB can generate a radical anion when photoexcited (the donor or acceptor) in the presence of an electron donor and when the ΔG^0_{et} is negative. To understand the formation of TCNQ•−, I recorded the steady-state absorption spectra of PNCs without or with TCNQ/TCNB in toluene. The absorption maximum of L-PNCs in toluene is 518 nm. After adding TCNQ, I found three more absorption features at 393, 755, and 845 nm, as shown in Figure 4.6. The absorption shoulder at 393 nm corresponds to the $S_0 \rightarrow S_1$ transition of TCNQ. Due to the unpaired single electron in the TCNQ anion, its electronic structure contains doublet states. The anion has broad absorption bands in the 600–900 nm region with two bands ca. 755 and 848 nm, due to the $D_0 \rightarrow D_1$ and $D_0 \rightarrow D_2$ transitions.[39,40]

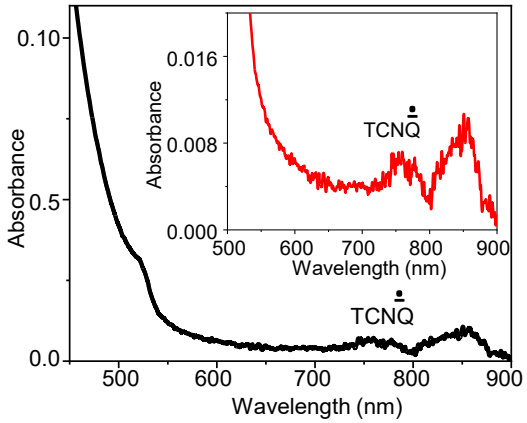

Figure 4.6. Steady-state absorption spectrum of L-PNCs with TCNQ. Inset: zoomed-in image showing the TCNQ radical anion absorption at 730 nm.

The electron transfer dynamics between PNCs and TCNB/TCNQ molecules were investigated by analyzing the PL spectra and decays of PNCs in the solution phase. The ensemble PL spectra were recorded for the colloidal C-PNCs in the presence or absence of TCNB/TCNQ (Figures 4.7A and B). At first, the PL spectrum of an L- PNC solution was recorded using a fluorescence spectrometer. A PNC solution was prepared by dissolving PNCs in toluene (0.1 mg/mL). I added 10 µL of 1.0 mM a TCNB or TCNQ solution in toluene to the L-PNC solution. As shown in Figures 4.7A and B, with the increase in the concentration of TCNB/TCNQ, the PL of the PNC solution was quenched gradually. This PL quenching in the solution phase suggests the electron transfer processes. In parallel, I studied the PL properties of PNCs by recording the PL decays using time-correlated single-photon counting (TCSPC) system. The PL decay

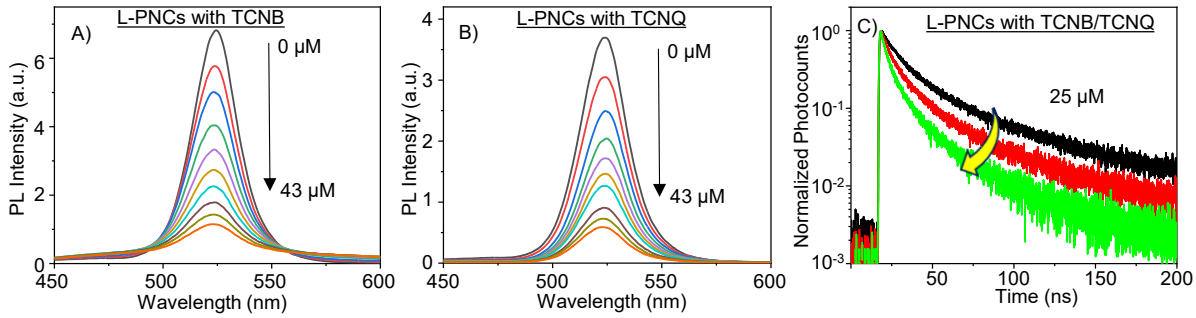

Figure 4.7. (A, B) PL spectra and (C) PL decay profiles of L-PNC solutions supplemented with (A) TCNQ or (B) TCNB (λ_{ex}: 405 nm).

profiles of L-PNCs without or with 25 μM of TCNB/TCNQ are shown in Figure 4.7C. The PL decay profiles were fitted using the third exponential equation (3):

$$\gamma(t) = \alpha_0 + \alpha_1 e^{(-t/\tau 1)} + \alpha_2 e^{(-t/\tau 2)} + \alpha_3 e^{(-t/\tau 3)} \quad (3)$$

where α_0 is a constant, α_1, α_2, and α_3 are the amplitudes, and τ_1, τ_2, and τ_3 are the lifetime components. Generally, the initial component arises from radiative recombination and the other two from non-radiative recombinations. I calculated the average PL lifetimes of the samples using the equation (4):

$$\Sigma\, \alpha_n \tau_n \,/\, \Sigma\, \alpha_n \quad (4)$$

The average PL lifetimes of the PNC solutions were also decreased (Table 4.1) with increases in the concentration of TCNB/TCNQ. The PL decay profiles of L-PNCs without or with TCNB and TCNQ are shown in Figures 4.8A and 4.9A, respectively. Here, the PL lifetime decreased with increases in the quencher/acceptor (TCNB/TCNQ) concentration. These results completely differ from chapter 3, where static PL quenching was the dominant process. In static quenching, the PL intensity was decreased but without affecting the PL lifetime. Here, a decrease in the PL lifetime accompanied by a decrease in the PL photocounts suggests dynamic quenching of the excited states of colloidal PNCs by TCNB/TCNQ. To get more insight into this PL quenching mechanism, the concentration of TCNB/TCNQ was plotted against the photocounts or the PL lifetimes of L-PNCs (Figures 4.8B, and 4.9B). The plotted graphs show a quenching mechanism dominated by the dynamic interaction between PNCs and TCNB/TCNQ.

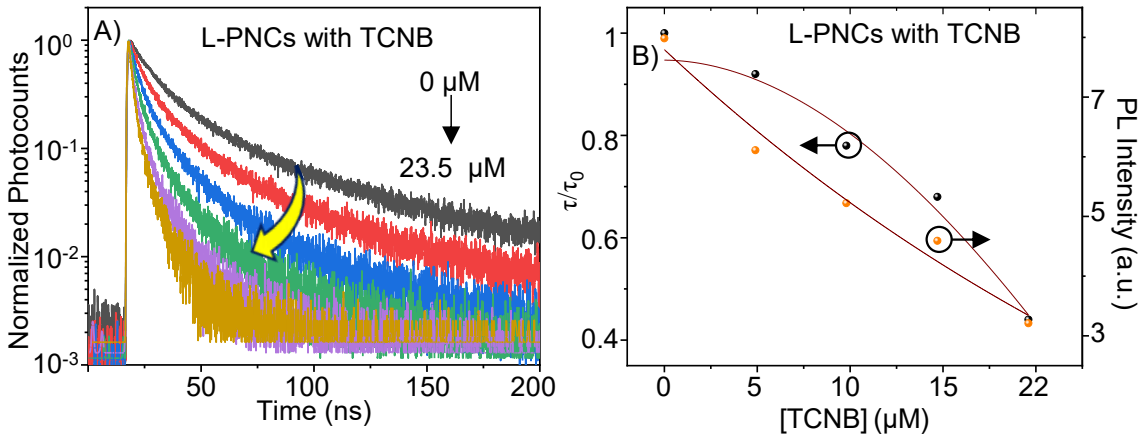

Figure 4.8. (A) PL decays of L-PNCs without or with different concentrations of TCNB. (B) The plots of the PL intensity or τ/τ_0 [ratio between the L-PNCs lifetime without (τ_0) or with (τ) TCNB] *vs* the TCNB concentration.

To confirm this dynamic quenching by electron transfer in a PNC solution, I performed similar experiments using the C-PNC-TCNB/TCNQ D-A systems. As the concentration of TCNB/TCNQ was increased, the PL intensity of the C-PNC solution was decreased (Figures 4.10A, B). Although, the corresponding PL lifetimes are also decreased (Figure 4.10C) with the increase in the TCNB/TCNQ concentration, the decrease was less prominent than L-PNCs.

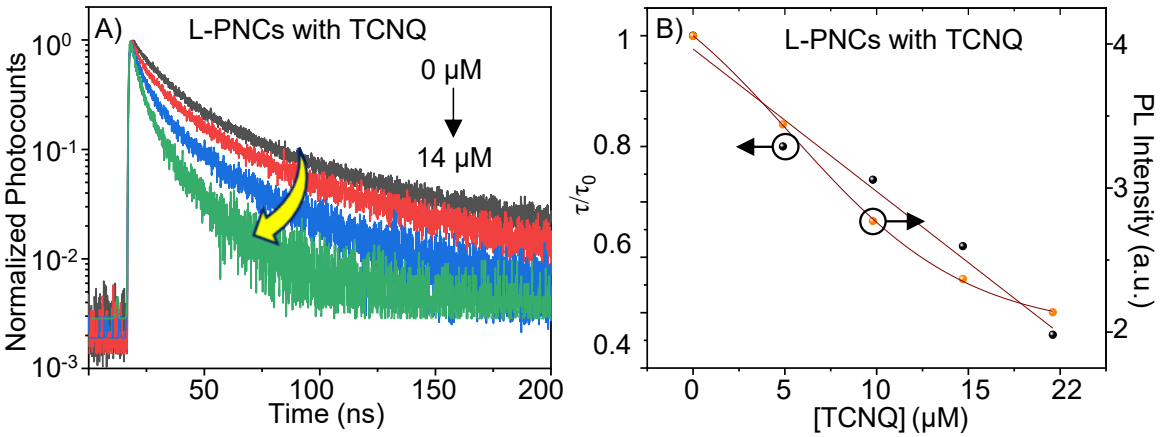

Figure 4.9. (A) PL decays of L-PNCs without or with different concentrations of TCNQ. (B) The plots of PL intensity or τ/τ_0 [ratio between the L-PNCs lifetime without (τ_0) or with (τ) TCNQ] vs the TCNQ concentration.

A gradual decrease in the average PL lifetimes of C/L-PNCs after the addition of different concentrations of TCNB/TCNQ is represented in Table 4.1. The PL intensity and lifetime

decreases show the quenchers in the solution phase dynamically interact with the PNC surface, and the interfacial electron transfer is dynamic in nature.

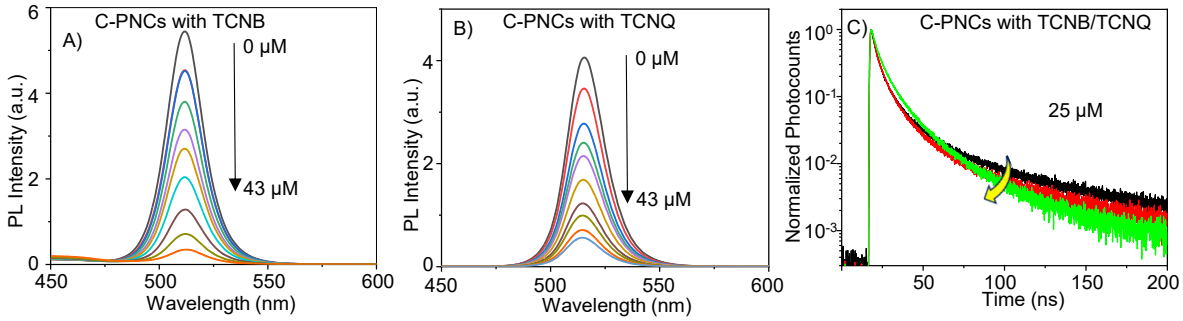

Figure 4.10. (A, B) PL spectra and (C) PL decay profiles of C-PNC solutions before or after the addition of (A) TCNQ or (B) TCNB (λ_{ex}: 405 nm).

Table 4.1: Triexponentially fitted average PL lifetimes of L/W-PNCs without or with TCNB/TCNQ.

Conc. of TCNB/TCNQ (µM)	τ_{av} (ns)			
	L-PNCs/ TCNB	L-PNCs/ TCNQ	C-PNCs/ TCNB	C-PNCs/ TCNQ
0	30.67	29.80	11.31	9.90
4.9	20.00	22.77	10.46	9.00
9.8	12.80	15.77	8.93	8.65
14.7	8.89	12.56	7.70	8.07
19.6	6.24	9.95	5.01	7.23

4.2.4 Electron transfer dynamics in nanocrystals

To obtain more insight into this electron transfer process, I investigated the effect of TCNB/TCNQ on PNCs at the single-particle level. At first, I evaluated the blinking behavior of pristine PNCs using a single-particle fluorescence microscope. The samples were prepared on a glass substrate by a drop and drag method to control the density of single C-PNCs at 60-80 particles per 100-100 µm^2 area, as shown in Figure 4.11A. In the case of W-PNCs, I spray cast the precursor mixture on a glass substrate. This method provided the density of single W-PNCs at 120-160 particles per 100-100 µm^2 area (Figure 4.11B). The electron transfer can be understood from changes in the blinking behavior of single PNCs. The PL blinking behavior

of both L-PNCs and W-PNCs is characterized by stochastic intensity fluctuations with short ON and OFF durations (Figure 4.12).

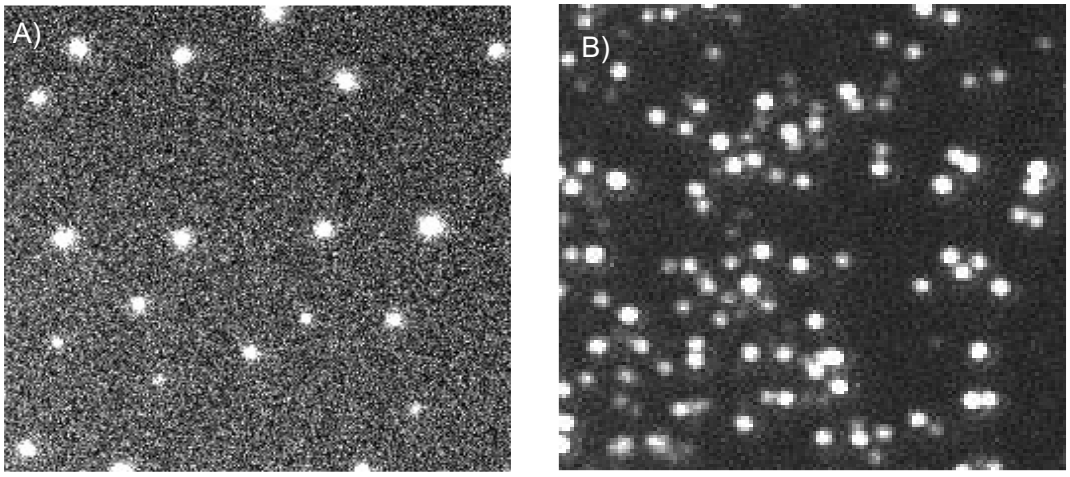

Figure 4.11. Single-particle PL images of (A) C-PNCs and (B) W-PNCs (λ_{ex}: 404 nm). The image sizes are 50 x 50 μm^2.

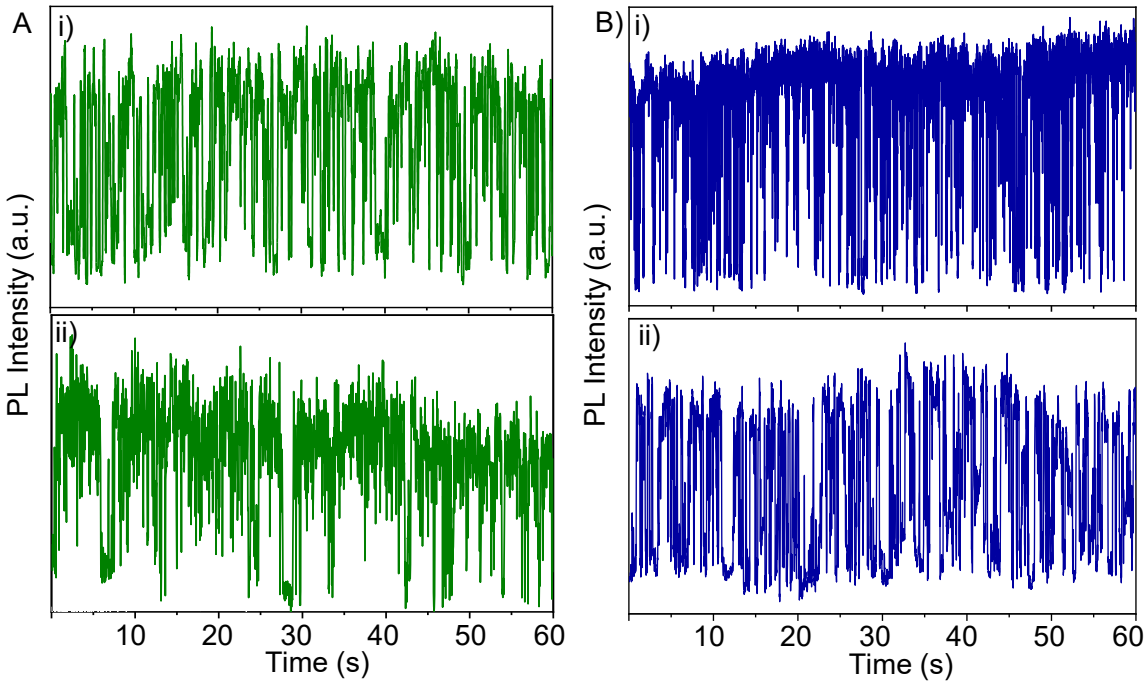

Figure 4.12. (A, B) PL intensity trajectories of (A; i, ii) C-PNCs and (B; i, ii) W-PNCs. The samples were excited with a 404 nm laser. The temporal resolution of the trajectories is 33 ms.

Real-time electron transfer experiments were performed for single W-PNCs using TCNB/TCNQ as an electron acceptor. At first, I collected the PL intensity trajectory of a pristine W-PNC for 60 s (Figure 4.13A), and a TCNB solution (1 mM in toluene) was

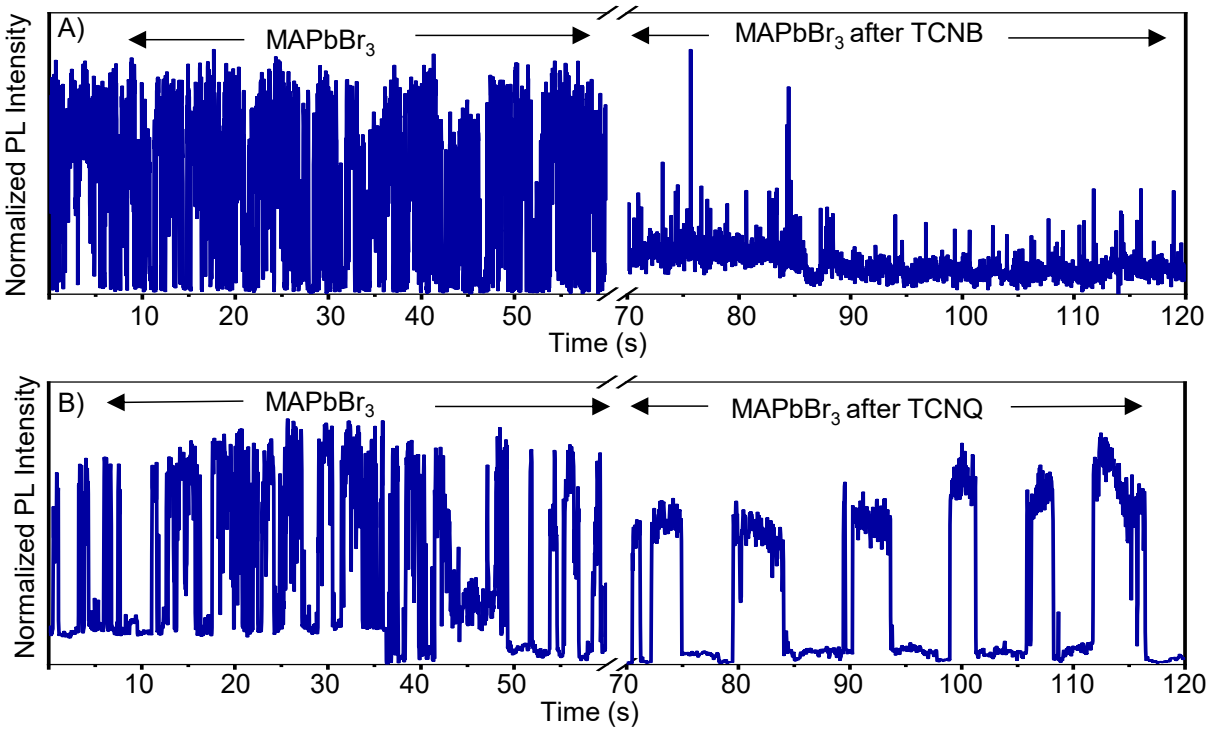

Figure 4.13. (A, B) Real-time PL intensity trajectories of single W-PNC before and after the addition of (A) TCNB (1 mM) or (B) TCNQ (1 mM) solutions. The samples were excited with a 404 nm laser. The temporal resolution of the trajectories is 33 ms.

introduced to the NC at ca 70 s and continued to record the PL intensity trajectory. After the treatment with the TCNB solution, the PL intensity was decreased, and the PL trajectory showed a low-intensity level with intermitted, short-living ON events. Figure 4.13B represents the real-time electron transfer of a W-PNC treated with a TCNQ solution (1 mM in toluene).

In this case, I observed an increase in the ON- and OFF-time. This blinking behavior is completely different before adding the TCNQ solution. The decreased average PL intensities and an increase in the OFF-time (4.13A, B) are attributed to single-particle interfacial electron transfer from PNCs to TCNB or TCNQ. However, such changes in the blinking vary from PNC to PNC. Therefore, to confirm the electron transfer-induced blinking change, I recorded the PL intensity trajectories of >450 single W-PNCs/C-PNCs before and after the treatment with a TCNB solution, and the ON/OFF-time probability distributions were analyzed to understand the blinking behavior when PET is operative. Figures 4.14 and 4.15 show the ON- and OFF-time probability distributions for W-PNCs and C-PNCs without or with TCNB.

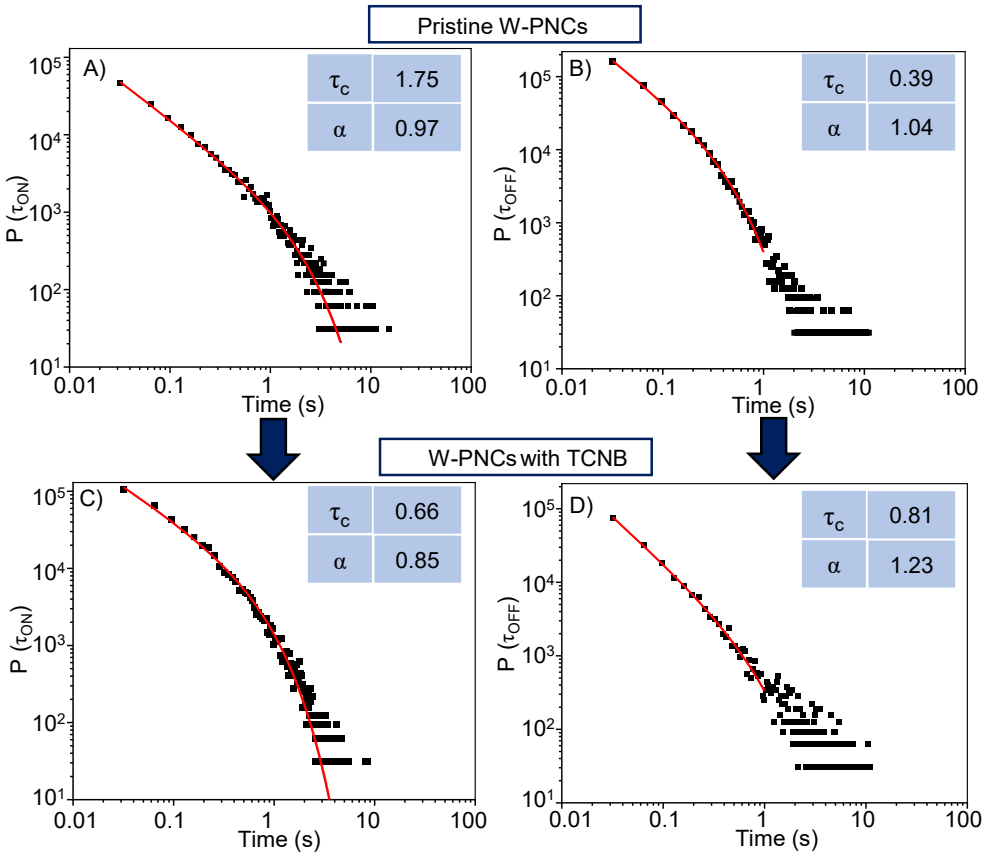

Figure 4.14. (A, C) ON-time and (B, D) OFF-time probability distribution of W-PNCs (A, B) before or (C, D) after the treatment with TCNB.

I analyzed the probability distributions using a truncated power law (equation 5).

$$P(\tau)=A_0\,\tau^{-\alpha}e^{-\tau/\tau c} \quad (5)$$

where τ_c is the truncation time, α is the power-law coefficient, and A_0 is a constant. I calculated the probability distributions using equation 6.

$$P(\tau) = 2N_i/(\tau_{i+1}+\tau_i) - (\tau_i+\tau_{i-1}) \quad (6)$$

where, τ is the time and N_i is the occurrence of the i^{th} time.

Pristine W-PNCs and C-PNCs exhibit photoionization (type A: charging/discharging) in the PL blinking mechanism, which is obvious from the exponential truncation cutoff of the probabilities at short time scales.

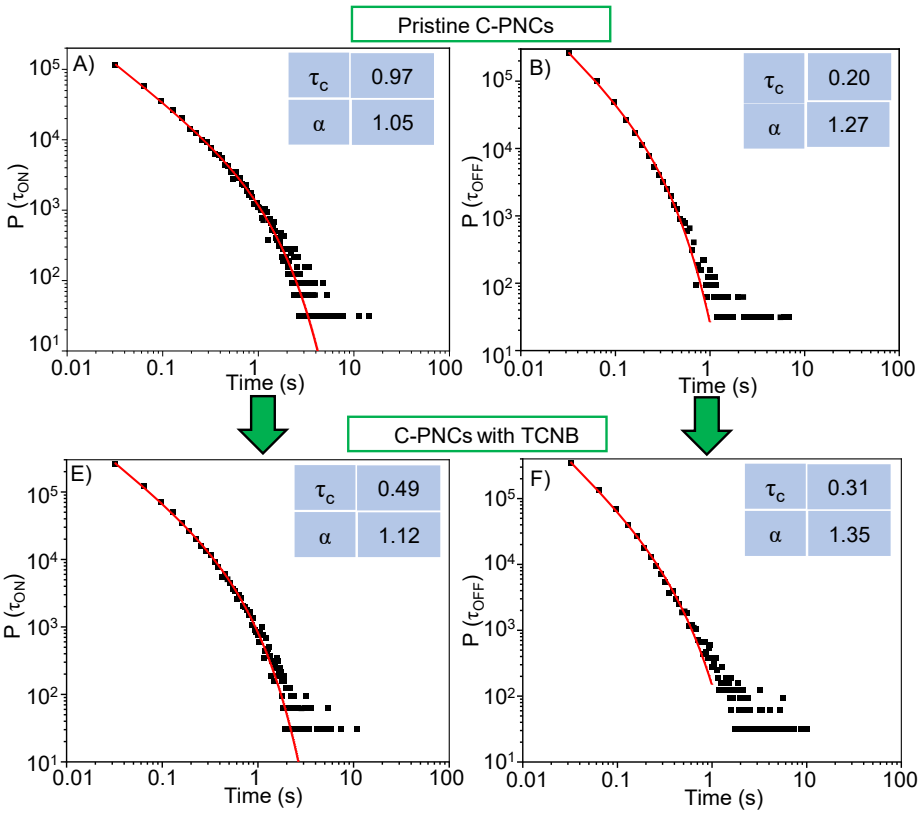

Figure 4.15. (A, C) ON-time and (B, D) OFF-time probability distribution of C-PNCs (A, B) before or (C, D) after the treatment with TCNB.

The truncation times are shown in the inset of Figures 4.14A, B and 4.15A, B. The OFF-events in single-particle PL blinking are mainly attributed to the non-radiative Auger recombination of charged carriers. PL recovers after neutralization of the ionized PNC. Therefore, the charging−discharging process is dominated by the blinking of pristine W/C-PNCs. The decreased truncation times of PNCs treated with TCNB (Figures 4.14C, D and 4.15C, D) suggest increases in the ionization probability, which is attributed to electron transfer to TCNB.

4.3 Conclusions

Lead halide PNCs are emerging into a class of cutting-edge materials for high-efficiency solar cells and light-emitting devices. In this chapter, I revealed the dynamics of photoinduced electron transfer through real-time blinking analysis of single PNCs. The negative value of Gibbs's free energy change helped predict the feasibility of electron transfer. The electron transfer was evident from decreased PL intensity and lifetime of PNCs treated with acceptors. The decreased truncation times of PNCs treated with TCNB suggest increases in the ionization

probability, which is attributed to electron transfer to TCNB. This study highlights the significance of an electron D-A interface at a single NC level.

References

(1) Chouhan, L.; Ghimire, S.; Subrahmanyam, C.; Miyasaka, T.; Biju, V. Synthesis, Optoelectronic Properties and Applications of Halide Perovskites. *Chem. Soc. Rev.* **2020**, *49*, 2869–2885.

(2) Dey, A.; Ye, J.; De, A.; Debroye, E.; Ha, S. K.; Bladt, E.; Kshirsagar, A. S.; Wang, Z.; Yin, J.; Wang, Y.; Quan, L. N.; Yan, F.; Gao, M.; Li, X.; Shamsi, J.; Debnath, T.; Cao, M.; Scheel, M. A.; Kumar, S.; Steele, J. A.; Gerhard, M.; Chouhan, L.; Xu, K.; Wu, X. G.; Li, Y.; Zhang, Y.; Dutta, A.; Han, C.; Vincon, I.; Rogach, A. L.; Nag, A.; Samanta, A.; Korgel, B. A.; Shih, C. J.; Gamelin, D. R.; Son, D. H.; Zeng, H.; Zhong, H.; Sun, H.; Demir, H. V.; Scheblykin, I. G.; Mora-Seró, I.; Stolarczyk, J. K.; Zhang, J. Z.; Feldmann, J.; Hofkens, J.; Luther, J. M.; Pérez-Prieto, J.; Li, L.; Manna, L.; Bodnarchuk, M. I.; Kovalenko, M. V.; Roeffaers, M. B. J.; Pradhan, N.; Mohammed, O. F.; Bakr, O. M.; Yang, P.; Müller-Buschbaum, P.; Kamat, P. V.; Bao, Q.; Zhang, Q.; Krahne, R.; Galian, R. E.; Stranks, S. D.; Bals, S.; Biju, V.; Tisdale, W. A.; Yan, Y.; Hoye, R. L. Z.; Polavarapu, L. State of the Art and Prospects for Halide Perovskite Nanocrystals. *ACS Nano* **2021**, *15*, 10775–10981.

(3) Nedelcu, G.; Protesescu, L.; Yakunin, S.; Bodnarchuk, M. I.; Grotevent, M. J.; Kovalenko, M. V. Fast Anion-Exchange in Highly Luminescent Nanocrystals of Cesium Lead Halide Perovskites ($CsPbX_3$, X = Cl, Br, I). *Nano Lett.* **2015**, *15*, 5635–5640.

(4) Protesescu, L.; Yakunin, S.; Bodnarchuk, M. I.; Krieg, F.; Caputo, R.; Hendon, C. H.; Yang, R. X.; Walsh, A.; Kovalenko, M. V. Nanocrystals of Cesium Lead Halide Perovskites ($CsPbX_3$, X = Cl, Br, and I): Novel Optoelectronic Materials Showing Bright Emission with Wide Color Gamut. *Nano Lett.* **2015**, *15*, 3692–3696.

(5) Shamsi, J.; Urban, A. S.; Imran, M.; De Trizio, L.; Manna, L. Metal Halide Perovskite Nanocrystals: Synthesis, Post-Synthesis Modifications, and Their Optical Properties. *Chem. Rev.* **2019**, *119*, 3296–3348.

(6) Zhang, Z.; Ghimire, S.; Okamoto, T.; Sachith, B. M.; Sobhanan, J.; Subrahmanyam, C.; Biju, V. Mechano-Optical Modulation of Excitons and Carrier Recombination in Self-Assembled Halide Perovskite Quantum Dots. *ACS Nano* **2022**, *16*, 160–168.

(7) Liu, M.; Johnston, M. B.; Snaith, H. J. Efficient Planar Heterojunction Perovskite Solar Cells by Vapour Deposition. *Nature* **2013**, *501*, 395–398.

(8) He, H.; Mei, S.; Chen, Z.; Liu, S.; Wen, Z.; Cui, Z.; Yang, D.; Zhang, W.; Xie, F.; Yang, B.; Guo, R.; Xing, G. Thioacetamide-Ligand-Mediated Synthesis of $CsPbBr_3$-$CsPbBr_3$ homostructured Nanocrystals with Enhanced Stability. *J. Mater. Chem. C* **2021**, *9* (34), 11349–11357.

(9) Sachith, B. M.; Okamoto, T.; Ghimire, S.; Umeyama, T.; Takano, Y.; Imahori, H.; Biju, V. Long-Range Interfacial Charge Carrier Trapping in Halide Perovskite-C_{60} and

Halide Perovskite-TiO_2 Donor-Acceptor Films. *J. Phys. Chem. Lett.* **2021**, *12*, 8644–8651.

(10) Ghimire, S.; Chouhan, L.; Takano, Y.; Takahashi, K.; Nakamura, T.; Yuyama, K. I.; Biju, V. Amplified and Multicolor Emission from Films and Interfacial Layers of Lead Halide Perovskite Nanocrystals. *ACS Energy Lett.* **2019**, *4*, 133–141.

(11) Levchuk, I.; Osvet, A.; Tang, X.; Brandl, M.; Perea, J. D.; Hoegl, F.; Matt, G. J.; Hock, R.; Batentschuk, M.; Brabec, C. J. Brightly Luminescent and Color-Tunable Formamidinium Lead Halide Perovskite $FAPbX_3$ (X = Cl, Br, I) Colloidal Nanocrystals. *Nano Lett.* **2017**, *17*, 2765–2770.

(12) Pushkarev, A. P.; Korolev, V. I.; Markina, D. I.; Komissarenko, F. E.; Naujokaitis, A.; Drabavičius, A.; Pakštas, V.; Franckevičius, M.; Khubezhov, S. A.; Sannikov, D. A.; Zasedatelev, A. V.; Lagoudakis, P. G.; Zakhidov, A. A.; Makarov, S. V. A Few-Minute Synthesis of $CsPbBr_3$ Nanolasers with a High-Quality Factor by Spraying at Ambient Conditions. *ACS Appl. Mater. Interfaces* **2019**, *11*, 1040–1048.

(13) Nair, V. C.; Muthu, C.; Rogach, A. L.; Kohara, R.; Biju, V. Channeling Exciton Migration into Electron Transfer in Formamidinium Lead Bromide Perovskite Nanocrystal/Fullerene Composites. *Angew. Chem. Int. Ed.* **2017**, *56*, 1214–1218.

(14) Rhee, S.; An, K.; Kang, K. T. Recent Advances and Challenges in Halide Perovskite Crystals in Optoelectronic Devices from Solar Cells to Other Applications. *Crystals* **2021**, *11*, 1–28.

(15) Que, M.; Zhu, L.; Guo, Y.; Que, W.; Yun, S. Toward Perovskite Nanocrystalline Solar Cells: Progress and Potential. *J. Mater. Chem. C* **2020**, *8*, 5321–5334.

(16) Wu, K.; Liang, G.; Shang, Q.; Ren, Y.; Kong, D.; Lian, T. Ultrafast Interfacial Electron and Hole Transfer from $CsPbBr_3$ Perovskite Quantum Dots. *J. Am. Chem. Soc.* **2015**, *137* (40), 12792–12795.

(17) Jiménez-López, J.; Puscher, B. M. D.; Guldi, D. M.; Palomares, E. Improved Carrier Collection and Hot Electron Extraction across Perovskite, C_{60}, and TiO_2 Interfaces. *J. Am. Chem. Soc.* **2020**, *142*, 1236–1246.

(18) Zhou, S.; Zhou, G.; Li, Y.; Xu, X.; Hsu, Y. J.; Xu, J.; Zhao, N.; Lu, X. Understanding Charge Transport in All-Inorganic Halide Perovskite Nanocrystal Thin-Film Field Effect Transistors. *ACS Energy Lett.* **2020**, *5*, 2614–2623.

(19) Jeon, I.; Ueno, H.; Seo, S.; Aitola, K.; Nishikubo, R.; Saeki, A.; Okada, H.; Boschloo, G.; Maruyama, S.; Matsuo, Y. Lithium-Ion Endohedral Fullerene ($Li^+@C_{60}$) Dopants in Stable Perovskite Solar Cells Induce Instant Doping and Anti-Oxidation. *Angew. Chem. Int. Ed.* **2018**, *57*, 4607–4611.

(20) Schulz, P. Interface Design for Metal Halide Perovskite Solar Cells. *ACS Energy Lett.* **2018**, *3*, 1287–1293.

(21) Wang, H.; Rahaq, Y.; Kumar, V. A Composite Light-Harvesting Layer from Photoactive Polymer and Halide Perovskite for Planar Heterojunction Solar Cells. *Sci. Rep.* **2016**, *6*, 29567.

(22) Sherkar, T. S.; Momblona, C.; Gil-Escrig, L.; Ávila, J.; Sessolo, M.; Bolink, H. J.; Koster, L. J. A. Recombination in Perovskite Solar Cells: Significance of Grain Boundaries, Interface Traps, and Defect Ions. *ACS Energy Lett.* **2017**, *2*, 1214–1222.

(23) Wu, S. H.; Lin, M. Y.; Chang, S. H.; Tu, W. C.; Chu, C. W.; Chang, Y. C. A Design Based on a Charge-Transfer Bilayer as an Electron Transport Layer for Improving the Performance and Stability in Planar Perovskite Solar Cells. *J. Phys. Chem. C* **2018**, *122*, 236–244.

(24) Credgington, D.; Jamieson, F. C.; Walker, B.; Nguyen, T. Q.; Durrant, J. R. Quantification of Geminate and Non-Geminate Recombination Losses within a Solution-Processed Small-Molecule Bulk Heterojunction Solar Cell. *Adv. Mater.* **2012**, *24*, 2135–2141.

(25) Passarelli, J. V.; Mauck, C. M.; Winslow, S. W.; Perkinson, C. F.; Bard, J. C.; Sai, H.; Williams, K. W.; Narayanan, A.; Fairfield, D. J.; Hendricks, M. P.; Tisdale, W. A.; Stupp, S. I. Tunable Exciton Binding Energy in 2D Hybrid Layered Perovskites through Donor–Acceptor Interactions within the Organic Layer. *Nat. Chem.* **2020**, *12*, 672–682.

(26) Ma, L.; Hu, P.; Jiang, H.; Kloc, C.; Sun, H.; Soci, C.; Voityuk, A. A.; Michel-Beyerle, M. E.; Gurzadyan, G. G. Single Photon Triggered Dianion Formation in TCNQ and F $_4$ TCNQ Crystals. *Sci. Rep.* **2016**, *6*, 1–7.

(27) Van Gompel, W. T. M.; Herckens, R.; Van Hecke, K.; Ruttens, B.; D'Haen, J.; Lutsen, L.; Vanderzande, D. Towards 2D Layered Hybrid Perovskites with Enhanced Functionality: Introducing Charge-Transfer Complexes: Via Self-Assembly. *Chem. Commun.* **2019**, *55*, 2481–2484.

(28) Jeong, H. W.; Zsigmond, T. S.; Samu, G. F.; Janáky, C. Sacrificial Agent Gone Rogue: Electron-Acceptor-Induced Degradation of CsPbBr3 Photocathodes. *ACS Energy Lett.* **2022**, *7*, 417–424.

(29) Hsu, C. L.; Lin, C. Te; Huang, J. H.; Chu, C. W.; Wei, K. H.; Li, L. J. Layer-by-Layer Graphene/TCNQ Stacked Films as Conducting Anodes for Organic Solar Cells. *ACS Nano* **2012**, *6*, 5031–5039.

(30) Nonoguchi, Y.; Nakashima, T.; Kawai, T. Low-Temperature Observation of Photoinduced Electron Transfer from CdTe Nanocrystals. *J. Phys. Chem. C* **2009**, *113*, 11464–11468.

(31) Liu, X.; Zhao, H.; Wei, L.; Ren, X.; Zhang, X.; Li, F.; Zeng, P.; Liu, M. Ligand-Modulated Electron Transfer Rates from $CsPbBr_3$ Nanocrystals to Titanium Dioxide. *Nanophotonics* **2021**, *10*, 1967–1975.

(32) Chouhan, L.; Ito, S.; Thomas, E. M.; Takano, Y.; Ghimire, S.; Miyasaka, H.; Biju, V. Real-Time Blinking Suppression of Perovskite Quantum Dots by Halide Vacancy Filling. *ACS Nano* **2021**, *15*, 2831–2838.

(33) Yuan, G.; Gómez, D. E.; Kirkwood, N.; Boldt, K.; Mulvaney, P. Two Mechanisms Determine Quantum Dot Blinking. *ACS Nano* **2018**, *12*, 3397–3405.

(34) Trinh, C. T.; Minh, D. N.; Ahn, K. J.; Kang, Y.; Lee, K. G. Organic-Inorganic $FAPbBr_3$ Perovskite Quantum Dots as a Quantum Light Source: Single-Photon Emission and Blinking Behaviors. *ACS Photonics* **2018**, *5* (12), 4937–4943.

(35) Trinh, C. T.; Minh, D. N.; Ahn, K. J.; Kang, Y.; Lee, K. G. Verification of Type-A and Type-B-HC Blinking Mechanisms of Organic–Inorganic Formamidinium Lead Halide Perovskite Quantum Dots by FLID Measurements. *Sci. Rep.* **2020**, *10*, 1–8.

(36) Hamada, M.; Nakanishi, S.; Itoh, T.; Ishikawa, M.; Biju, V. Blinking Suppression in CdSe / ZnS Single. *ACS Nano* **2010**, *4*, 4445–4454.

(37) Brennan, M. C.; Forde, A.; Zhukovskyi, M.; Baublis, A. J.; Morozov, Y. V.; Zhang, S.; Zhang, Z.; Kilin, D. S.; Kuno, M. Universal Size-Dependent Stokes Shifts in Lead Halide Perovskite Nanocrystals. *J. Phys. Chem. Lett.* **2020**, *11*, 4937–4944.

(38) Kumar, K.; Kurnikov, I. V.; Beratan, D. N.; Waldeck, D. H.; Zimmt, M. B. Use of Modern Electron Transfer Theories to Determine Electronic Coupling Matrix Elements in Intramolecular Systems. *J. Phys. Chem. A* **1998**, *102* (28), 5529–5541.

(39) Ma, L.; Hu, P.; Kloc, C.; Sun, H.; Michel-Beyerle, M. E.; Gurzadyan, G. G. Ultrafast Spectroscopic Characterization of 7,7,8,8- Tetracyanoquinodimethane (TCNQ) and Its Radical Anion (TCNQ-). *Chem. Phys. Lett.* **2014**, *609*, 11–14.

(40) Panja, S.; Kadhane, U.; Andersen, J. U.; Holm, A. I. S.; Hvelplund, P.; Kirketerp, M. B. S.; Nielsen, S. B.; Støchkel, K.; Compton, R. N.; Forster, J. S.; Kilså, K.; Nielsen, M. B. Dianions of 7,7,8,8-Tetracyano- p -Quinodimethane and Perfluorinated Tetracyanoquinodimethane: Information on Excited States from Lifetime Measurements in an Electrostatic Storage Ring and Optical Absorption Spectroscopy. *J. Chem. Phys.* **2007**, *127*, 124301.

Chapter 5

Plasmon-coupled exciton dynamics in perovskite nanocrystals

Abstract

Localized surface plasmon resonance of metal nanoparticles significantly improves the optical properties of halide perovskite nanocrystals. However, plasmon-induced photoluminescence enhancement is still underutilized because of not fully understand the origin of plasmon-induced photoluminescence enhancement. In this chapter, I report the dynamics of plasmon-induced photoluminescence enhancement and quenching for perovskite nanocrystals with ligand discrimination between the active and inactive chemical coupling of Au-Br bonding. The interaction significantly changes the optical properties of methylammonium lead bromide perovskite nanocrystals with adjacent localized surface plasmon resonance of Au nanoparticles. The dynamics of photoluminescence enhancement and quenching are examined at the single-particle level. A decrease in the photoluminescence lifetime accompanies a significant increase in OFF intervals. The direct synthesis of $MAPbBr_3$ perovskite nanocrystals on Au-nanoparticles increases the total radiative decay rate by the resonance caused by chemical coupling between Au-Br and the surface plasmon resonance. This change in the radiative rate increases single particles' photoluminescence intensity and OFF times.

5.1 Introduction

Over the past decade, halide perovskites have been attracting tremendous attention because of their excellent photophysical and optoelectronic properties.[1-10] High photoluminescence (PL) quantum yields,[3] high photostabilities,[4] large optical gain,[5] versatile solution processability, and the halide ion-based bandgap tuning[6] make these perovskites ideal for various optoelectronic devices, such as lasers,[1,7] light-emitting diodes,[3,8,9] solar cells,[1,3,4,6,8] and photodetectors.[1,8,10] Recently, heterostructures comprising halide perovskite nanocrystals (PNCs) and metal nanostructures are also explored for plasmonic-electronic devices.[11-15] Interactions between excitons and photons[16] help enhance the fluorescence quantum efficiency[17,18] and manipulate the photophysical dynamics[19] of perovskites. The performance of perovskite devices is improved by combining metal nanoparticles (NPs) with perovskite nanocrystals.[20]

The perovskites-metal composites can generate strong light-matter coupled states due to the coupling of the excitons of perovskites and the localized surface plasmon resonance (LSPR) of the metal NPs. Therefore, understanding the mechanism of PNCs coupled with the LSPR at the single-particle level can provide further insights into the fundamental process of the exciton-plasmon interactions. To date, this plasmon coupled PL fluctuations (blinking), and the origins of enhancement and quenching in PNC-Au nanostructures remain largely unknown.

LSPR-induced optical properties improvement has been reported not only for perovskites but also for organic dye molecules and conventional chalcogenide semiconductor quantum dots (QDs). In the early investigations of dye molecules' plasmon-induced PL enhancement, Knoll et al.[21] reported PL enhancement of cadmium arachidate monolayer coated on a silver grating. Kinkhabwala et al.[22] reported the enhancement of single-molecule fluorescence up to 1,340 times by using an Au nanoantenna. For conventional semiconductor QDs, Ma et al.[23] reported the PL intensity enhancement for single CdSe multi-shell nanocrystal on the Au NP film up to 3 times. Fu et al.[24] reported blinking suppression and PL intensity enhancement for streptavidin functionalized CdSe/ZnS QDs linked to biotin-coated Ag NPs.

These plasmon-induced PL intensity enhancements are based on energy transfer from LSPR to fluorophores or Purcell effects, an increase of the spontaneous emission rate caused by the plasmon-induced strong near field (hot spots). The PL intensity enhancement by energy transfer and PL quenching by energy or charge transfer depend on the distance between a fluorophore and the plasmonic substrate. In this study, I prepared the heterostructures of PNCs on Au NPs, analyzed the exciton-plasmon interaction, and validated the photophysical properties of PNCs. The PNCs on an Au NP film show a strong PL intensity enhancement up

to 12-fold at the single-particle level. I also study the dynamics of PL intensity enhancement or quenching of single PNCs with ligand discrimination between the active and inactive chemical coupling of Au-Br. First, I synthesized two different $MAPbBr_3$ PNCs and prepared the hetero-nanostructure films with Au NPs and PNCs. I confirm the LSPR coupling with excitons at a single particle level by PL blinking, PL intensity, and PL lifetime studies. By considering the dot-by-dot variations of the ON- and OFF-time distributions, I perform the statistical evaluation of the ON/OFF-time probability distributions for more than 450 PNCs on an Au or a glass substrate to understand the differences in the blinking behavior.

5.2 Results and discussion

5.2.1 Preparation of perovskite nanocrystals and Au nanoparticles

The synthesis of colloidal $MAPbBr_3$ PNCs (L-PNCs) was carried out by the LARP method, and a modified spray technique was employed to prepare the $MAPbBr_3$ PNCs without ligand (W-PNCs). The detailed synthesis procedures are given in section 2.2.1. The pristine PNCs were characterized using STEM, UV-vis absorption spectroscopy, and fluorescence spectroscopy. The STEM images of both L-PNCs and W-PNCs are shown in Figures 5.1A and B, respectively. The STEM images reveal the uniform size distribution of PNCs. I analyzed the STEM images using imageJ software and estimated the size distribution at 10.2 nm for L-PNCs and 6.3 nm for W-PNCs. I also estimated the average size of Au NPs sputtered (7 s) on a STEM grid at 8 ± 2.23 nm (Figure 5.1C).

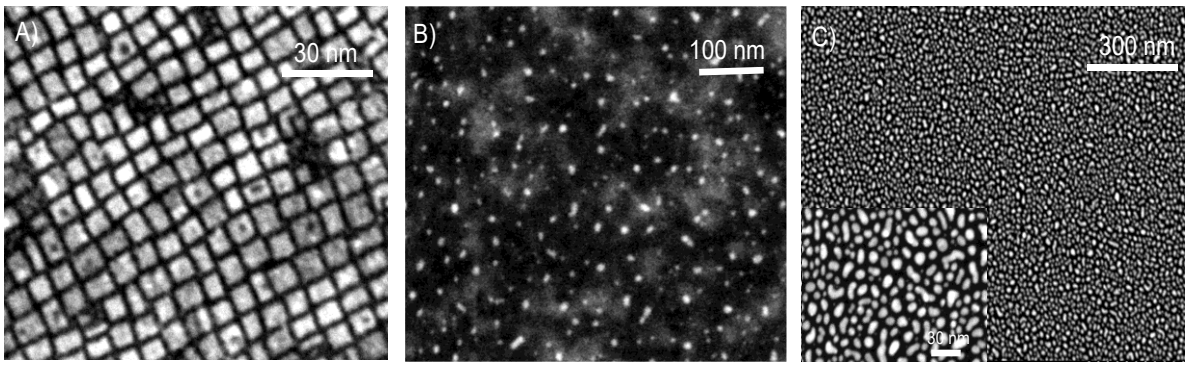

Figure 5.1. Structural characteristics of nanoparticles. STEM images of (A) L-PNCs, (B) W-PNCs and (C) Au NPs.

The photophysical properties of the PNCs are studied using UV-vis absorption spectroscopy and PL spectroscopy. Here, the L-PNCs were dispersed in toluene and diluted further to record the spectra. Figure 5.2A represents the UV-vis absorption and PL spectra of

L-PNCs recorded in toluene. The inset shows the PNCs dispersed in toluene and taken under UV light. Figure 5.2B shows the absorption and PL spectra of W-PNCs sprayed on glass/Au, and the insets represent the microscopic image of a single W-PNC sprayed on glass or an Au plasmon substrate. The L-PNCs in toluene exhibit the PL spectrum ca. 520 nm, whereas the W-PNCs show it at ca. 532 and ca. 535 nm when sprayed on glass and an Au plasmon substrate, respectively. Perhaps, a more interesting feature is the ~ 3 nm red shift for W-PNC on the Au substrate than on the glass substrate. As reported by Abhijit and co-workers,[26] such a redshift PL spectrum is attributed to the charge transfer process between W-PNC and Au NPs. Figures 5.2C and 5.2D represent the EMCCD and hand-held CCD camera images of W-PNCs.

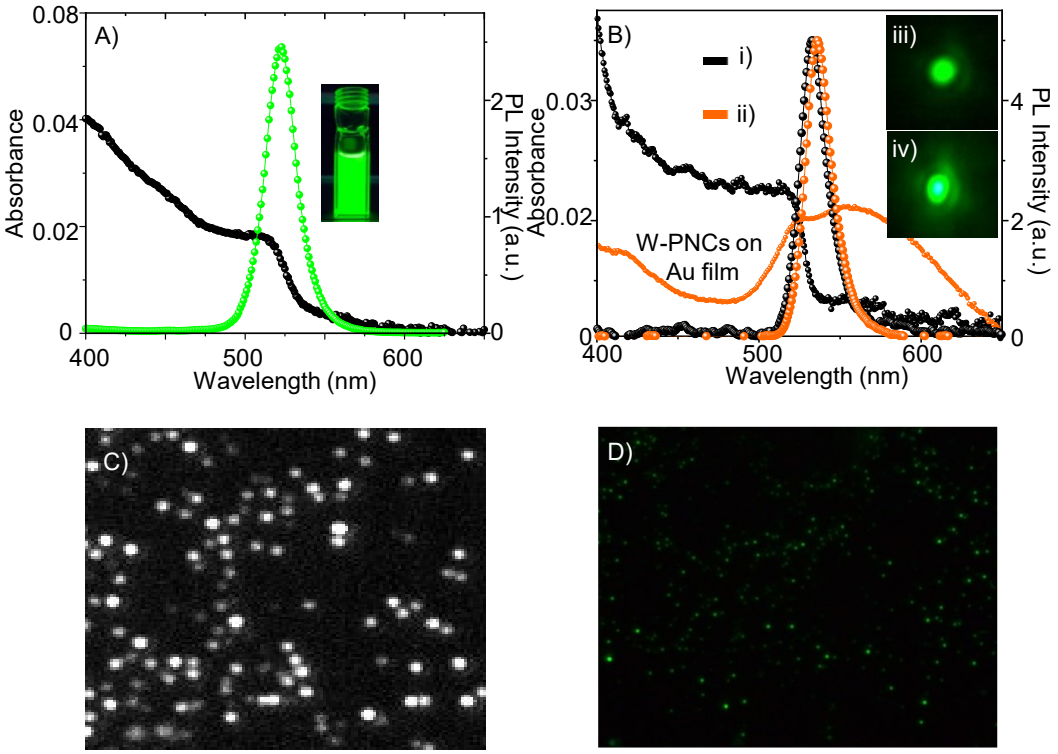

Figure 5.2. (A, B) Absorption and PL spectra of (A) L-PNCs and (B) W-PNCs. The broad absorption spectrum represents the Au NP film. The traces (i) and (ii) are for single W-PNCs on (i) a glass substrate and (ii) an Au NP film. The inset in A shows the photograph of an L-PNC solution in toluene and under UV light. The insets in B show the PL images of W-PNCs on (iii) a glass and (iv) an Au NP substrate. (C, D) PL images of W-PNCs sprayed on a glass substrate and detected using (C) an EMCCD camera and (D) a hand-held CCD camera. The scales are (C) 50 x 50 μm^2 and (D) 100 x 100 μm^2.

5.2.2 Exciton dynamics in nanocrystals

The PL blinking behavior of PNCs was investigated using a single-particle fluorescence microscope. At first, the L-PNCs samples were prepared on a glass substrate by a drop and drag method. In the case of W-PNCs, I spray cast the precursor mixture on a glass substrate. This method provided the density of single W-PNCs at 120-160 particles per 100-100 μm^2 area (Figure 5.2C). I focus on the blinking of single PNCs, to understand the general blinking behavior of both pristine L-PNCs and W-PNCs. Representative PL blinking trajectories of the as-synthesized L-PNCs and W-PNCs on glass substrates are shown in Figures 5.3 A (i, ii, L-PNCs), B (i, ii, W-PNCs). An interesting feature in the blinking of W-PNCs is an excellent signal-to-noise (S/N) ratio without any photobleaching. The PL blinking varies from particle to particle in the ON- and OFF-time distributions. It changes from rapid ON-and OFF-events to long-lived ON/OFF-events. As reported in the literature, the main origin of pristine $MAPbBr_3$ PNC blinking is based on the charging−discharging processes. Here, the dielectric factor plays an important role in exciton confinement. Noticeably, the smaller size W-PNCs (6.3 nm), compared to the 10.2 nm edge size of L-PNCs, leads to prominent quantum confinement. This stronger confinement and enhanced Coulomb interactions in W-PNCs probably increase the probability of ionization and non-radiative Auger processes.

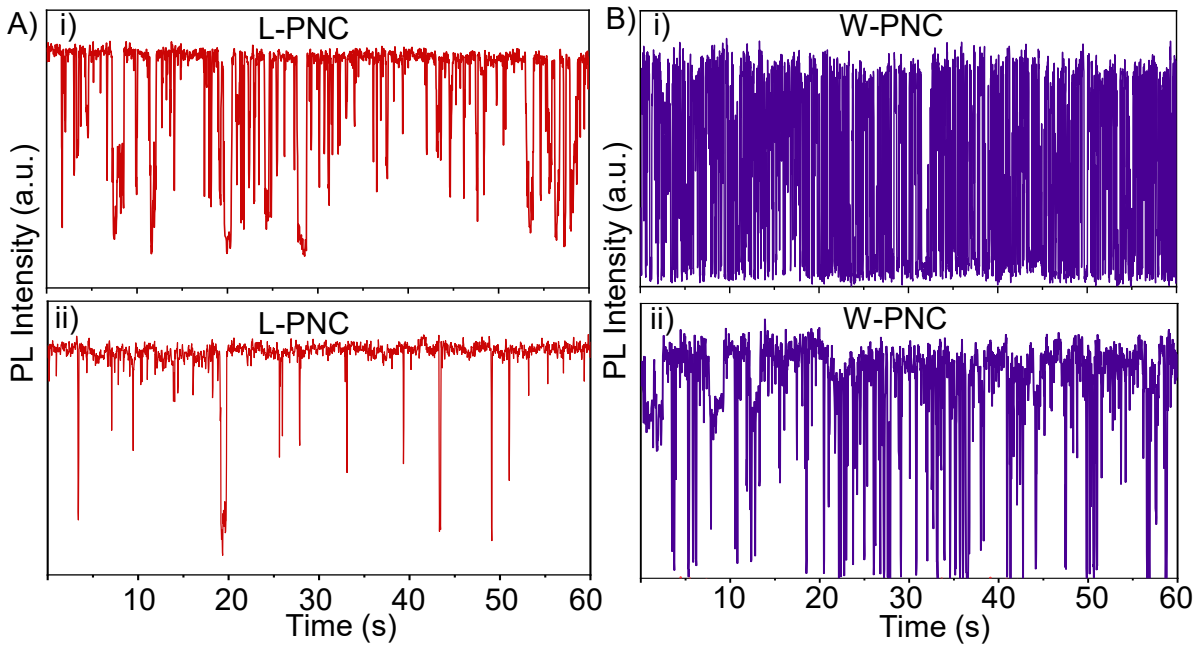

Figure 5.3. The PL blinking behavior of PNCs on a glass substrate and excited at 404 nm. (A, B) PL intensity trajectories of $MAPbBr_3$ PNCs: [A (i, ii)] L-PNCs and [B (i, ii)] W-PNCs.

On the other hand, every single W/L-PNC show different PL blinking behavior with changes in ON- and OFF-time distributions. Thus, to understand the general blinking behavior of both L-PNCs and W-PNCs, I performed statistical analyses for a large number of single W/LPNCs. I analyzed the ON-time and OFF-time probability distributions of >250 pristine L-PNCs and W-PNCs with a truncated power law (eq 1, Figures 5.4A-D).

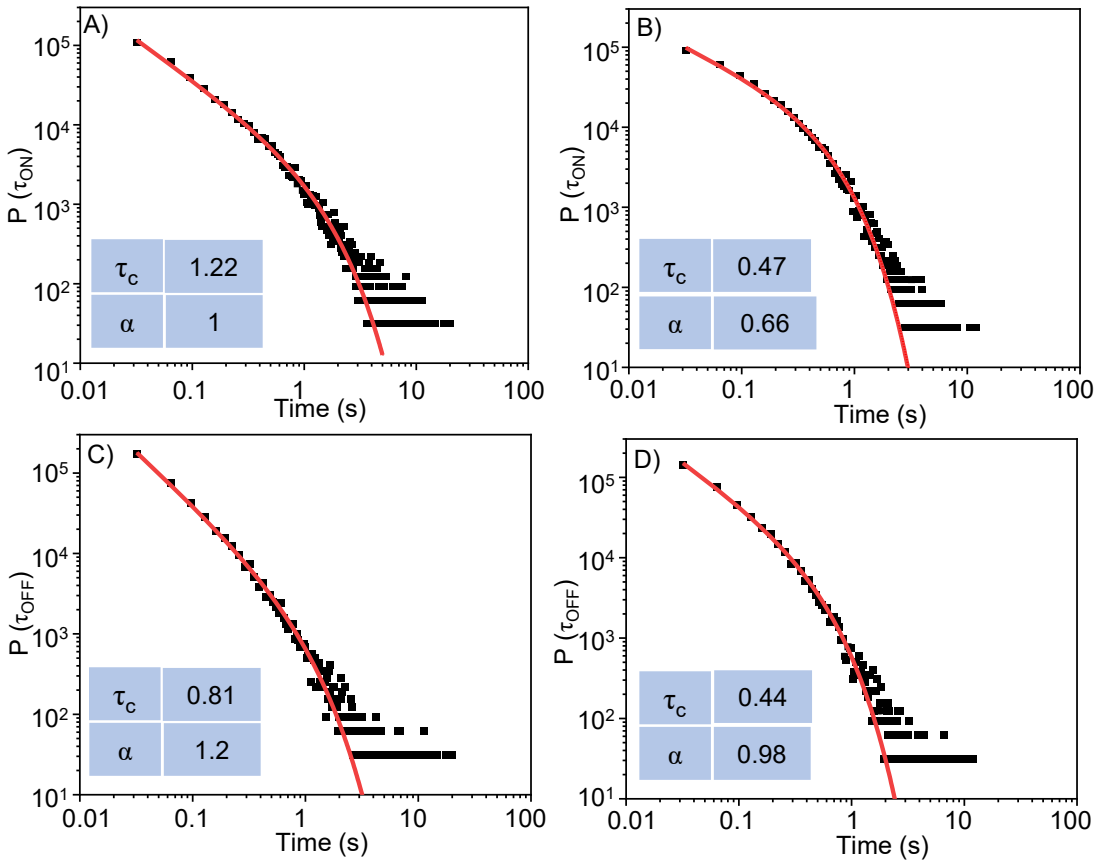

Figure 5.4. The PL blinking characteristics of PNCs. Log-log distributions of (A, B) ON-time and (B, D) OFF-time probabilities of (A, C) L-PNCs and (B, D) W-PNCs.

$$P(\tau) = A_0\, \tau^{-\alpha} e^{-\tau/\tau_c} \quad (1)$$

Here, A_0 is constant, α is the power-law coefficient, τ_c is the truncation time, and the probability distribution is calculated using eq 2.

$$P(\tau) = 2N_i/(\tau_{i+1} + \tau_i) - (\tau_i + \tau_{i-1}) \quad (2)$$

Here, N_i is the occurrence of i^{th} time, and τ refers to the time.

The PL blinking of PNCs has been widely investigated. The charging-discharging model (type-A)[27-30] and activation-deactivation of nonradiative recombination centers (type-B)[31,32] are well-known mechanisms to explain the ON-OFF events. In my experimental data, pristine W-PNCs and L-PNCs exhibit photoionization (type A: charging-discharging) in the PL blinking. This charging-discharging mechanism was obvious from the exponential ON-time truncation cutoff in the power-law relation (Figure 5.4A and B). The ON- and OFF truncation times of both the L-PNCs (ON = 1.22, and OFF = 0.81) and W-PNCs (ON = 0.47, and OFF = 0.44) are shown in the insets of Figures 5.4A-D.

5.2.3 Plasmon-induced exciton dynamics

To understand the dynamics of exciton-plasmon and metal-halogen interactions, I placed both L-PNCs and W-PNCs on separate Au NP films. I used a drop-drag and a spray method to control the density of single PNCs in the samples. I observed PL intensity quenching for most L-PNCs on an Au NP film.[33] Also, there was no change in the PL blinking behavior for bright PNCs compared to pristine L-PNCs. Representative PL intensity trajectories of L-PNCs on Au films are shown in Figures 5.5A and B.

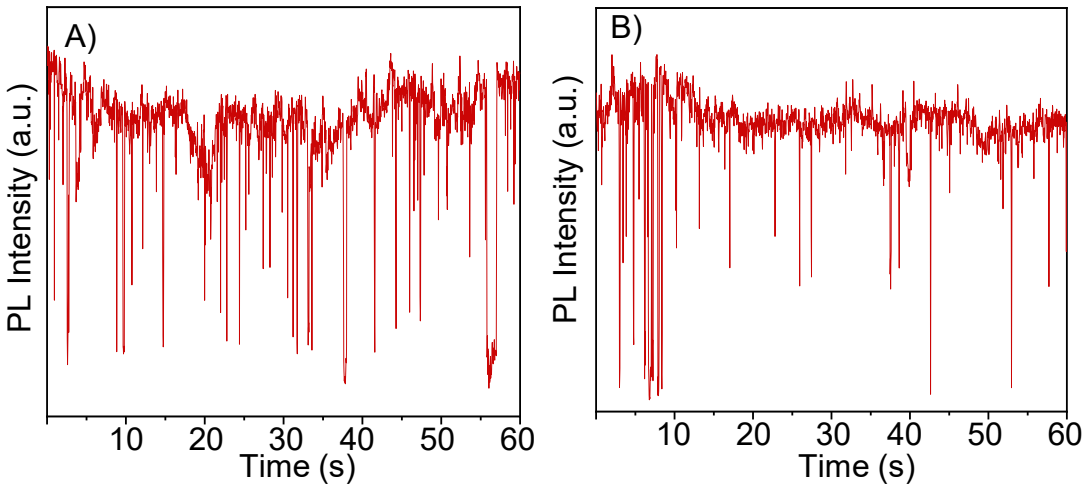

Figure 5.5. (A, B) PL intensity trajectories of L-PNCs tethered on Au NP films.

On the other hand, W-PNCs showed a huge PL intensity enhancement on an Au NP film. Surprisingly, most W-PNCs showed excellent signal-to-noise ratios and short ON and OFF durations (Figure 5.6), reflecting exciton-plasmon coupling and energy transfer from Au NPs to PNCs. To understand this PL blinking behavior and rule out dot-by-dot variations in the ON- and OFF-time distributions, I analyzed ON-time and OFF-time probability distributions of

>110 W-PNCs on a glass or on an Au NP substrate with a truncated power law (Figures 5.7A, B). I found a short (τ_c-ON = 0.2 s) truncation time for the ON probability (Figure 5.7A) and a significant increase (τ_c-OFF = 2.5 s) in the truncation time of the OFF-time probability (Figure 5.7B) compared to the W-PNCs on glass substrates (τ_c-ON = 0.47 s, and τ_c-OFF = 0.44 s). The

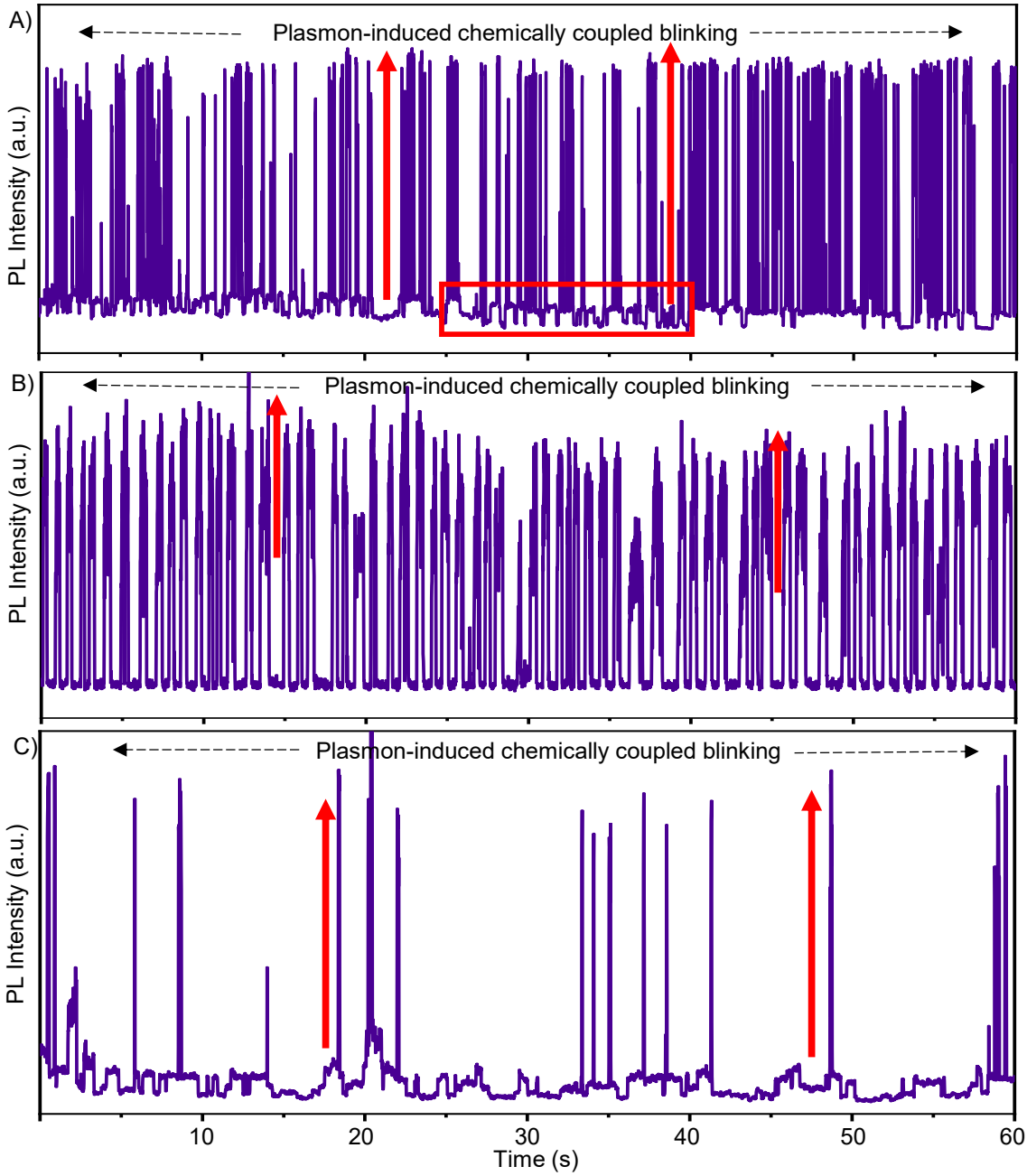

Figure 5.6. Plasmon-induced, chemically-coupled PL blinking. (A, B, C) PL intensity trajectories of W-PNCs on an Au NPs film. Samples were excited at 404 nm. The marked position in A is enlarged and shown in Figure 5.8.

truncated power-law fitting of the ON- and OFF-time distributions of W-PNCs on Au films are the signature of the type-A blinking, but the changes in the τ_c are noticeable. The PL intensity enhancement, excellent signal-to-noise ratio, and decreased ON time truncation suggest an exciton-plasmon-coupling-induced energy transfer from Au NPs to PNCs.

An efficient coupling of Au LSPR with PNCs resulted in fast radiative decay of W-PNCs, which probably decreased the ON time. One of the main differences in the exciton-plasmon coupling between $MAPbBr_3$ L-PNCs and W-PNCs is that the direct attachment of W-PNCs on Au NPs increases the radiative recombination rate, probably due to the formation of an Au-Br resonance that enables a chemical enhancement of energy transfer from the LSPR to the PNCs. Conversely, the ligands on L-PNCs prevent such a chemical effect. This hypothesis of Au-Br-based, chemically enhanced energy transfer is considered based on the formation of metal-halogen bonds (MX: M = Au, Ag, Pt, Cu, and X= I, Br, Cl) by Au-complexes interacting with halogen-donors.[34] The ligand-free surface of W-PNCs supports a direct interaction between the Au surface and Br in the $PbBr_6$ octahedron. Also, it is known that the d^2_z lone pair orbital of Au donates some charge density to the empty σ* orbital (Br-Br) of Br_2.[35-38]

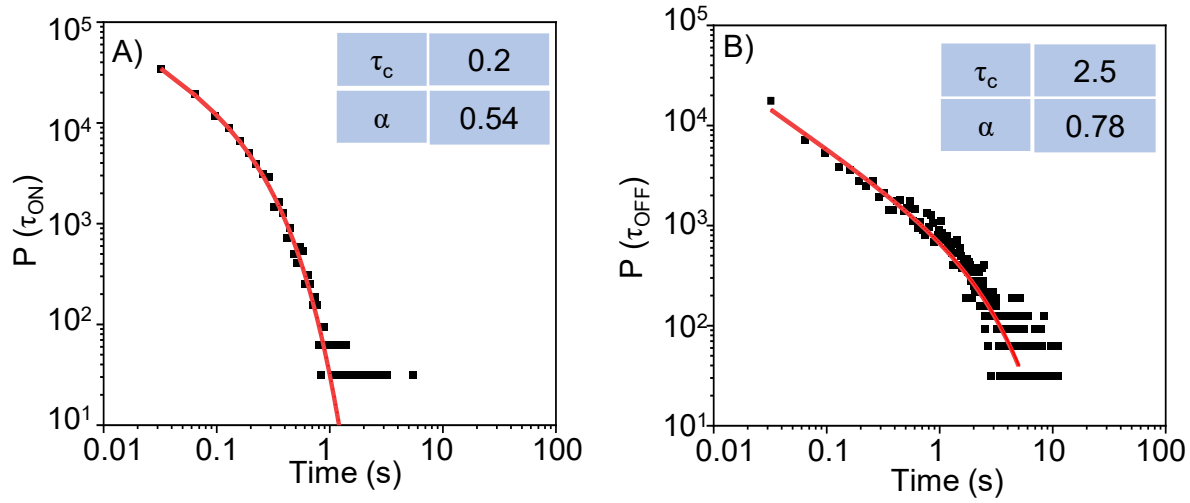

Figure 5.7. Log-log distributions of (A) ON-time and (B) OFF-time probabilities of W-PNC single particles on Au NP films.

Figure 5.8A represents the zoomed-in part of Figure 5.6A, showing intermittent PL intensity enhancement due to exciton-plasmon coupling for a W-PNC. The blinking characteristics of this W-PNC enable me to propose four hypotheses about the coupling that may have important implications for LSPR-assisted PL intensity enhancement in halide perovskites: i) The neutral state of a PNC enters into the energy transfer state by coupling with

the LSPR to enhance the PL intensity, and the high-intensity state decouples from the enhancement and form the neutral state of the PNC [Figure 5.8B(i)]. (ii) The Auger ionized state couples with the LSPR, and the intensity enhancement takes place from the dark state, which is followed by decoupling of the exciton-plasmon state by ionization to form the dark state [Figure 5.8B(ii)]. (iii) The PL intensity enhanced state in (ii) is quenched by decoupling to form the neutral state (ON) [Figure 5.8B(iii)]. (iv) The PL intensity enhanced state in (i) is quenched by decoupling from the ionized state (OFF) [Figure 5.8B(iv)].

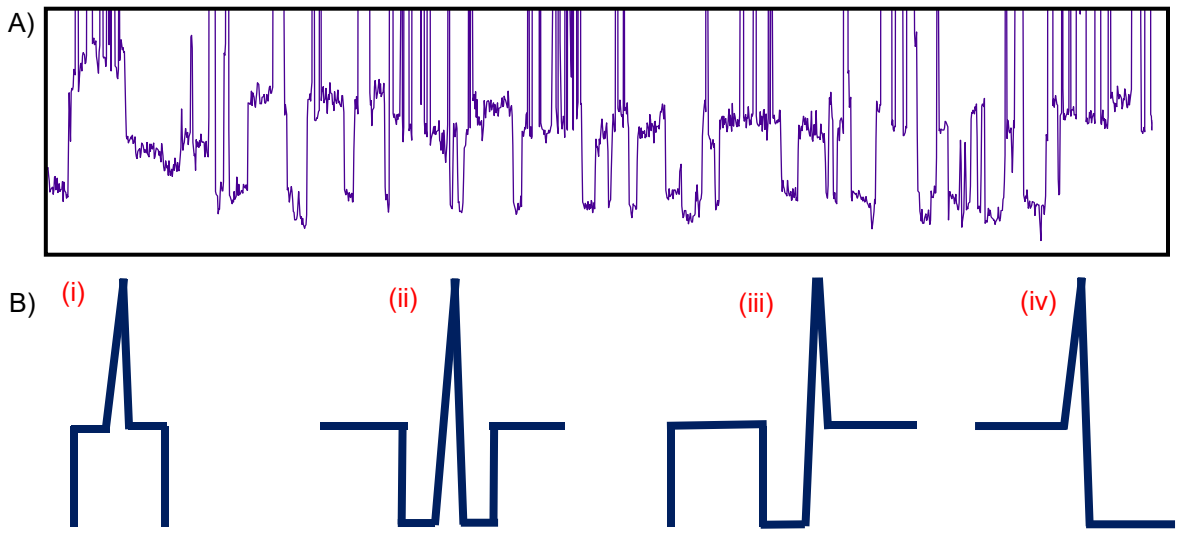

Figure 5.8. Plasmon-induced chemically-coupled PL blinking of PNCs. (A) A zoomed-in PL intensity trajectory portion from Figure 5.6A showing the coupling-decoupling events. (B) A schematic representation of plasmon-induced PL intensity enhancement from the neutral (ON) state or ionized (OFF) states followed by decoupling of the exciton-plasmon coupled energy transfer state to form the neutral (ON) or ionized (OFF) states.

5.2.4 Exciton dynamics in perovskite nanocrystals on Au films

To understand the above-proposed hypotheses, I evaluated the PL lifetimes (Table 5.1) and PL photocounts of single L/W-PNCs on glass or Au NP substrates. The PL decay profiles of a single W-PNC or L-PNC on glass or an Au NP substrate are shown in Figures 5.9A and B, respectively. The corresponding PL lifetime components are given in table 5.1, and streak camera images are shown in Figure 5.10.

The PL decay profiles were fitted using the third exponential equation (3):

$$\gamma(t) = \alpha_0 + \alpha_1 e^{(-t/\tau 1)} + \alpha_2 e^{(-t/\tau 2)} + \alpha_3 e^{(-t/\tau 3)} \quad (3)$$

where α_0 is a constant, α_1, α_2, and α_3 are the amplitudes, and τ_1, τ_2, and τ_3 are the lifetime components. Generally, the initial component arises from radiative recombination and the other two from non-radiative recombinations. I calculated the average PL lifetimes of the samples using equation (4):

$$\Sigma \alpha_n \tau_n / \Sigma \alpha_n \quad (4)$$

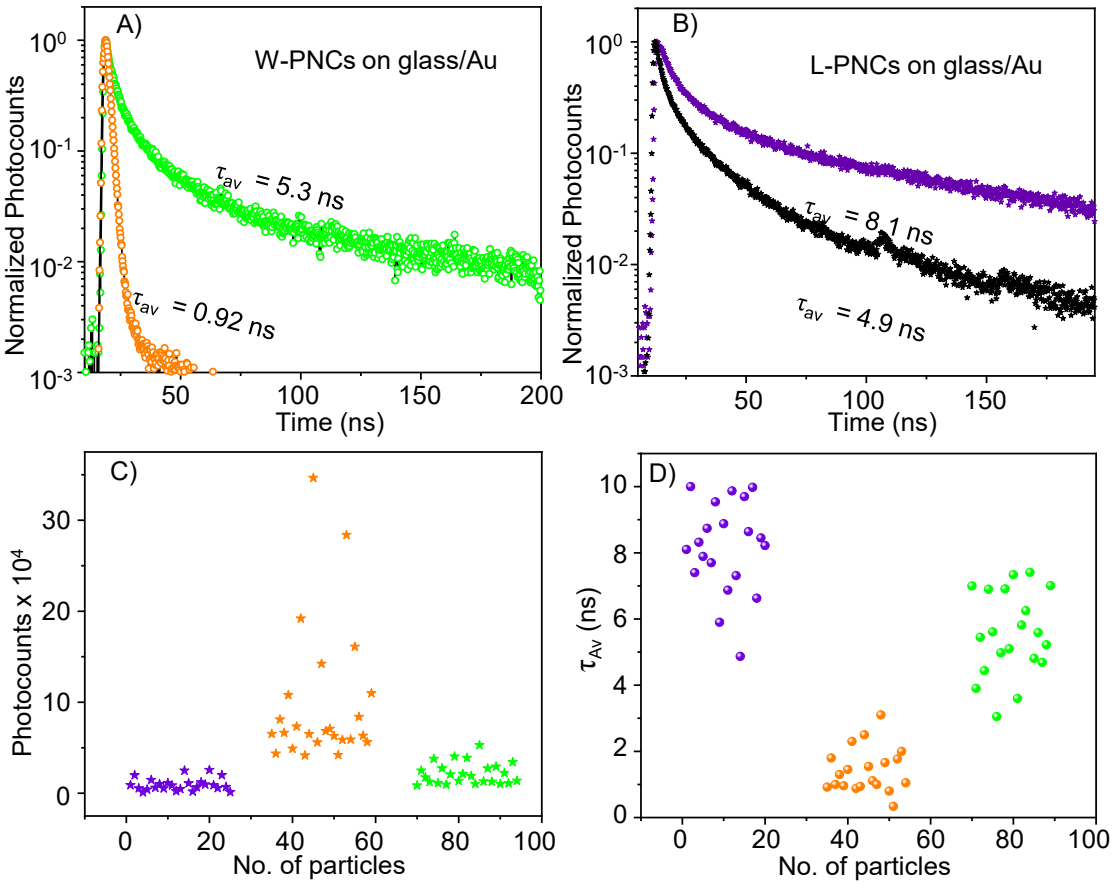

Figure 5.9. Exciton dynamics of PNCs on Au NP films. (A, B) PL decay profiles of W/L-PNCs on (green, purple) a glass substrate or (orange, black) on Au NP films. (C, D) The plots of (C) the PL photocounts or (D) the PL lifetimes against the number of particles (purple: L-PNCs on a glass substrate, orange: W-PNCs on an Au NP film, green: W-PNCs on a glass substrate).

I found the PL lifetime of a W-PNC on an Au NP film much smaller (0.92 ns) than on a glass substrate (5.3 ns). Interestingly, this short lifetime was accompanied by 12-fold increase in the PL photocounts. In contrast, single L-PNCs on an Au NP film showed only 50% decrease in the PL lifetime compared to an L-PNC on a glass substrate. The PL lifetimes and the number

Table 5.1: Triexponentially fitted PL decay components of L/W-PNCs.

Sample	τ_1 (ns)	τ_2 (ns)	τ_3 (ns)	% of τ_1	% of τ_2	% of τ_3
L-PNC/glass	5.39	16.5	30	74	24.2	1.8
L-PNC/Au	3.9	11.1	42	80	18.1	1.1
W-PNC/glass	2.57	12	42.74	73.8	25.1	1.1
W-PNC/Au	0.89	1.1	1	98	2	0

of emitted photons can vary from PNC-to-PNC, depending on the degree of exciton-plasmon coupling and the local environment. Hence, I record the PL lifetimes and photocounts for >100 single PNCs on glass and Au substrates. The average PL lifetime values for W-PNCs on Au NPs and glass substrates are 1.2 ns and 5.8 ns, respectively (Figure 5.9C). Consistently, the PL photocounts were higher for W-PNCs on Au NPs than glass substrates. The PL lifetimes and photocounts suggest LSPR-assisted fast radiative decay for W-PNCs on Au NPs.

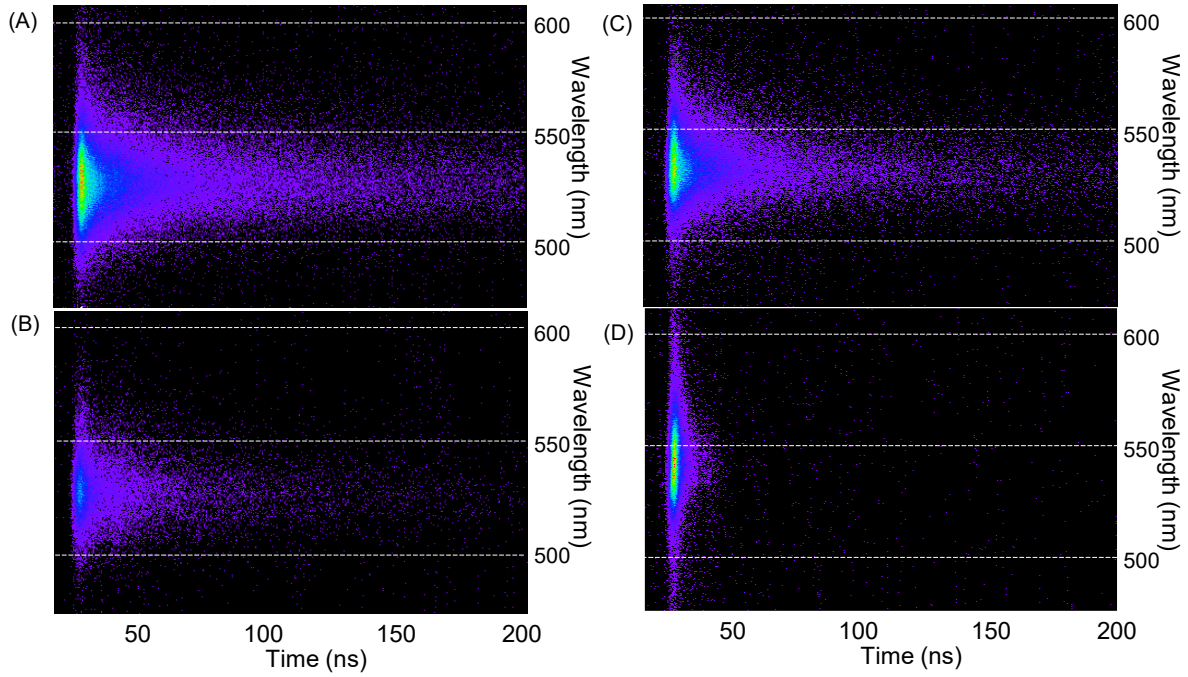

Figure 5.10. Temporally- and spectrally-resolved photocount maps of $MAPbBr_3$ PNCs: (A, B) L-PNC on (A) a glass substrate and (B) an Au NP film. (C, D) W-PNCs on (C) a glass substrate and (D) an Au NP film.

Based on the above results, I provide a tentative picture of PL enhancement in the W-PNC-Au system on the LSPR-coupled energy transfer framework (Figure 5.11). The PL quantum efficiency (ϕ_1) of a PNC on a glass substrate is given by equation 5:

$$\phi_1 = k_{r1} / (k_{r1} + k_{nr1}) \quad (5)$$

where, k_{r1} and k_{nr1} are the radiative and non-radiative decay rates. For W-PNC on an Au NP substrate, the enhanced PL intensity and short PL lifetime are attributed to Au-Br-coupled Forster energy transfer from Au NPs to a W-PNC. Accordingly, the PL quantum yield on an Au NP substrate (ϕ_2) is given by equation 6:

$$\phi_2 = k_{r2} / (k_{r2} + k_{nr1}) \quad (6)$$

where, k_{r2} is the radiative decay rate of the W-PNC-AU system. From the PL lifetime and photocount data $k_{r2} >> k_{r1}$, and $k_{r2} >> k_{nr1}$. Here, I assume that the coupling (Au-Br and LSPR-exciton) enables the energy transfer, which is observed at the single-particle level.

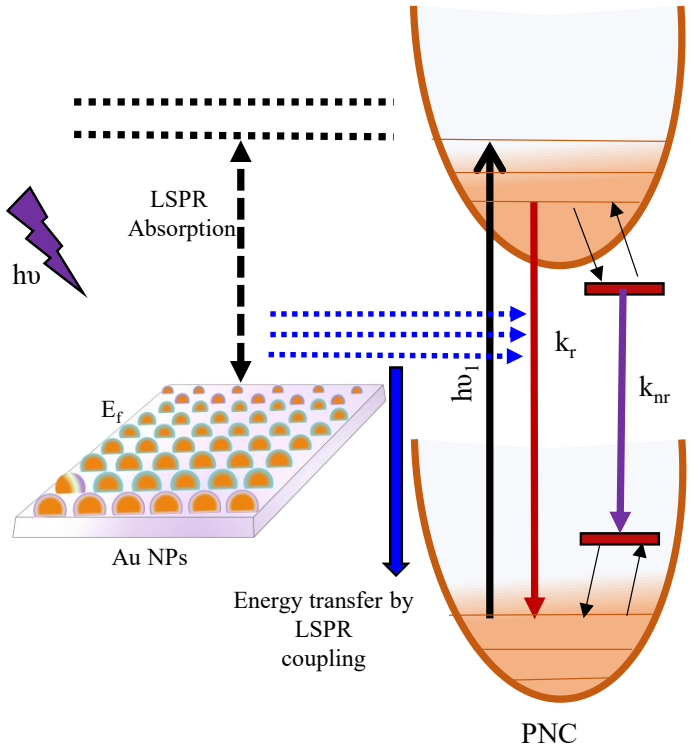

Figure 5.11. A hypothetical scheme of PL enhancement and quenching for W-PNCs and L-PNCs on Au NP substrates.

5.3 Conclusions

In summary, I developed plasmon-coupled PNC heterostructures and detected an increased radiative recombination rate and photoluminescence photocounts for PNCs without ligands on

an Au NP substrate. The PL intensity enhancement up to 12-fold at the single-particle was accompanied by a sudden decrease in PL lifetime. The PL enhancement is attributed to Au-Br-assisted, LSPR-mediated energy transfer from Au to PNCs. Fluctuations in the PL intensity are attributed to transient decoupling of the Au-Br interactions.

References

1. Dey, A.; Ye, J.; De, A.; Debroye, E.; Ha, S. K.; Bladt, E.; Kshirsagar, A. S.; Wang, Z.; Yin, J.; Wang, Y.; Quan, L. N.; Yan, F.; Gao, M.; Li, X.; Shamsi, J.; Debnath, T.; Cao, M.; Scheel, M. A.; Kumar, S.; Steele, J. A.; Gerhard, M.; Chouhan, L.; Xu, K.; Wu, X. G.; Li, Y.; Zhang, Y.; Dutta, A.; Han, C.; Vincon, I.; Rogach, A. L.; Nag, A.; Samanta, A.; Korgel, B. A.; Shih, C. J.; Gamelin, D. R.; Son, D. H.; Zeng, H.; Zhong, H.; Sun, H.; Demir, H. V.; Scheblykin, I. G.; Mora-Seró, I.; Stolarczyk, J. K.; Zhang, J. Z.; Feldmann, J.; Hofkens, J.; Luther, J. M.; Pérez-Prieto, J.; Li, L.; Manna, L.; Bodnarchuk, M. I.; Kovalenko, M. V.; Roeffaers, M. B. J.; Pradhan, N.; Mohammed, O. F.; Bakr, O. M.; Yang, P.; Müller-Buschbaum, P.; Kamat, P. V.; Bao, Q.; Zhang, Q.; Krahne, R.; Galian, R. E.; Stranks, S. D.; Bals, S.; Biju, V.; Tisdale, W. A.; Yan, Y.; Hoye, R. L. Z.; Polavarapu, L. State of the Art and Prospects for Halide Perovskite Nanocrystals. *ACS Nano* **2021**, *15*, 10775–10981.

2. Shi, D.; Adinolfi, V.; Comin, R.; Yuan, M.; Alarousu, E.; Buin, A.; Chen, Y.; Hoogland, S.; Rothenberger, A.; Katsiev, K.; Losovyj, Y.; Zhang, X.; Dowben, P. A.; Mohammed, O. F.; Sargent, E. H.; Bakr, O. M. Low Trap-State Density and Long Carrier Diffusion in Organolead Trihalide Perovskite Single Crystals. *Science.* **2015**, *347*, 519–522.

3. Chouhan, L.; Ghimire, S.; Subrahmanyam, C.; Miyasaka, T.; Biju, V. Synthesis, Optoelectronic Properties and Applications of Halide Perovskites. *Chem. Soc. Rev.* **2020**, *49*, 2869–2885.

4. Sachith, B. M.; Okamoto, T.; Ghimire, S.; Umeyama, T.; Takano, Y.; Imahori, H.; Biju, V. Long-Range Interfacial Charge Carrier Trapping in Halide Perovskite-C_{60} and Halide Perovskite-TiO_2 Donor-Acceptor Films. *J. Phys. Chem. Lett.* **2021**, *12*, 8644–8651.

5. Huang, X.; Li, H.; Zhang, C.; Tan, S.; Chen, Z.; Chen, L.; Lu, Z.; Wang, X.; Xiao, M. Efficient Plasmon-Hot Electron Conversion in Ag–$CsPbBr_3$ Hybrid Nanocrystals. *Nat. Commun.* **2019**, *10*, 1–8.

6. Jeong, J.; Kim, M.; Seo, J.; Lu, H.; Ahlawat, P.; Mishra, A.; Yang, Y.; Hope, M. A.; Eickemeyer, F. T.; Kim, M.; Yoon, Y. J.; Choi, I. W.; Darwich, B. P.; Choi, S. J.; Jo, Y.; Lee, J. H.; Walker, B.; Zakeeruddin, S. M.; Emsley, L.; Rothlisberger, U.; Hagfeldt, A.; Kim, D. S.; Grätzel, M.; Kim, J. Y. Pseudo-Halide Anion Engineering for α-$FAPbI_3$ Perovskite Solar Cells. *Nature* **2021**, *592*, 381–385.

7. Schlaus, A. P.; Spencer, M. S.; Miyata, K.; Liu, F.; Wang, X.; Datta, I.; Lipson, M.; Pan, A.; Zhu, X. Y. How Lasing Happens in $CsPbBr_3$ Perovskite Nanowires. *Nat. Commun.* **2019**, *10*, 1–8.

8. Shamsi, J.; Urban, A. S.; Imran, M.; De Trizio, L.; Manna, L. Metal Halide Perovskite Nanocrystals: Synthesis, Post-Synthesis Modifications, and Their Optical Properties. *Chem. Rev.* **2019**, *119*, 3296–3348.

9. Chakraborty, S.; Mannar, S.; Viswanatha, R. Local Surface Plasmon-Assisted Metal Oxide Perovskite Heterostructure for Small Light Emitters. *J. Phys. Chem. C* **2021**, *125*, 10565–10571.

10. Ji, L.; Hsu, H. Y.; Lee, J. C.; Bard, A. J.; Yu, E. T. High-Performance Photodetectors Based on Solution-Processed Epitaxial Grown Hybrid Halide Perovskites. *Nano Lett.* **2018**, *18*, 994–1000.

11. Lee, D. S.; Kim, W.; Cha, B. G.; Kwon, J.; Kim, S. J.; Kim, M.; Kim, J.; Wang, D. H.; Park, J. H. Self-Position of Au NPs in Perovskite Solar Cells: Optical and Electrical Contribution. *ACS Appl. Mater. Interfaces* **2016**, *8*, 449–454.

12. Fu, N.; Bao, Z. Y.; Zhang, Y. L.; Zhang, G.; Ke, S.; Lin, P.; Dai, J.; Huang, H.; Lei, D. Y. Panchromatic Thin Perovskite Solar Cells with Broadband Plasmonic Absorption Enhancement and Efficient Light Scattering Management by Au@Ag Core-Shell Nanocuboids. *Nano Energy* **2017**, *41*, 654–664.

13. Mohamed Saheed, M. S.; Mohamed, N. M.; Mahinder Singh, B. S.; Jose, R. Surface Plasmon Assisted Electron-Hole Migration for High Photocurrent Density Generation in a Perovskite Solar Cell. *ACS Appl. Energy Mater.* **2019**, *2*, 8707–8714.

14. Park, J.; Kim, K.; Jo, E. J.; Kim, W.; Kim, H.; Lee, R.; Lee, J. Y.; Jo, J. Y.; Kim, M. G.; Jung, G. Y. Plasmon Enhanced Up-Conversion Nanoparticles in Perovskite Solar Cells for Effective Utilization of near Infrared Light. *Nanoscale* **2019**, *11*, 22813–22819.

15. Chen, L. C.; Tien, C. H.; Lee, K. L.; Kao, Y. T. Efficiency Improvement of MAPBI3 Perovskite Solar Cells Based on a $CsPbBr_3$ Quantum Dot/Au Nanoparticle Composite Plasmonic Light-Harvesting Layer. *Energies* **2020**, *13*.

16. Liu, J., Chen, Y. G., Gan, L., Xiao, T. H. & Li, Z. Y. Realization of Plasmonic Microcavity with Full Transverse and Longitudinal Mode Selection. *Sci. Rep.* **2016***, 6*, 1–9.

17. Liu, B.; Gutha, R. R.; Kattel, B.; Alamri, M.; Gong, M.; Sadeghi, S. M.; Chan, W. L.; Wu, J. Z. Using Silver Nanoparticles-Embedded Silica Metafilms as Substrates to Enhance the Performance of Perovskite Photodetectors. *ACS Appl. Mater. Interfaces* **2019**, *11*, 32301–32309.

18. Hsu, H. L.; Juang, T. Y.; Chen, C. P.; Hsieh, C. M.; Yang, C. C.; Huang, C. L.; Jeng, R. J. Enhanced Efficiency of Organic and Perovskite Photovoltaics from Shape-Dependent Broadband Plasmonic Effects of Silver Nanoplates. *Sol. Energy Mater. Sol. Cells* **2015**, *140*, 224–231.

19. Brus, L. Noble Metal Nanocrystals: Plasmon Electron Transfer Photochemistry and Single-Molecule Raman Spectroscopy. *Acc. Chem. Res.* **2008**, *41*, 1742–1749.

20. Cui, J.; Chen, C.; Han, J.; Cao, K.; Zhang, W.; Shen, Y.; Wang, M. Surface Plasmon Resonance Effect in Inverted Perovskite Solar Cells. *Adv. Sci.* **2016**, *3*, 1–8.

21. Knoll, W.; Philpott, M. R.; Swalen, J. D.; Girlando. A. Emission of light from Ag metal gratings coated with dye monolayer assemblies. *J. Chem. Phys.* **1981**, *75*, 4795–4799.

22. Kinkhabwala, A. *et al.* Large single-molecule fluorescence enhancements produced by a bowtie nanoantenna. *Nat. Photonics* **2009**, *3*, 654–657.

23. Ma, X.; Tan, H.; Kipp, T.; Mews, A. Fluorescence Enhancement, Blinking Suppression, and Gray States of Individual Semiconductor Nanocrystals Close to Gold Nanoparticles. *Nano Lett.* **2010**, *10*, 4166–4174.

24. Fu, Y.; Zhang, J.; Lakowicz, J. R. Silver-Enhanced Fluorescence Emission of Single Quantum Dot Nanocomposites. *Chem. Commun.* **2009**, 3, 313–315.

25. Lal, S.; Grady, N. K.; Kundu, J.; Levin, C. S.; Lassiter, J. B.; Halas, N. J. Tailoring Plasmonic Substrates for Surface Enhanced Spectroscopies. *Chem. Soc. Rev.* **2008**, *37*, 898–911.

26. Biswas, A.; Swarnkar, A.; Pandey, P.; Kour, P.; Parmar, S.; Ogale, S.; Ogale, S. Dynamics of Photo-Generated Carriers across the Interface between $CsPbBr_3$ Nanocrystals and Au-Ag Nanostructured Film, and Its Control via Ultrathin MgO Interface Layer. *ACS Omega* **2020**, *5*, 11915–11922.

27. Lee, J.; Hernandez, P.; Lee, J.; Govorov, A. O.; Kotov, N. A. Exciton-Plasmon Interactions in Molecular Spring Assemblies of Nanowires and Wavelength-Based Protein Detection. *Nat. Mater.* **2007**, *6*, 291–295.

28. Akimov, A. V.; Mukherjee, A.; Yu, C. L.; Chang, D. E.; Zibrov, A. S.; Hemmer, P. R.; Park, H.; Lukin, M. D. Generation of Single Optical Plasmons in Metallic Nanowires Coupled to Quantum Dots. *Nature* **2007**, *450*, 402–406.

29. Ming, T.; Chen, H.; Jiang, R.; Li, Q.; Wang, J. Plasmon-Controlled Fluorescence: Beyond the Intensity Enhancement. *J. Phys. Chem. Lett.* **2012**, *3*, 191–202.

30. Zhang, D.; Peng, L.; Shang, X.; Zheng, W.; You, H.; Xu, T.; Ma, B.; Ren, B.; Fang, J. Buoyant Particulate Strategy for Few-to-Single Particle-Based Plasmonic Enhanced Nanosensors. *Nat. Commun.* **2020**, *11*, 1–7.

31. Tong, F.; Liang, X.; Wang, Z.; Liu, Y.; Wang, P.; Cheng, H.; Dai, Y.; Zheng, Z.; Huang, B. Probing the Mechanism of Plasmon-Enhanced Ammonia Borane Methanolysis on a CuAg Alloy at a Single-Particle Level. *ACS Catal.* **2021**, *11*, 10814–10823.

32. Balakrishnan, S. K.; Kamat, P. V. Au-$CsPbBr_3$ Hybrid Architecture: Anchoring Gold Nanoparticles on Cubic Perovskite Nanocrystals. *ACS Energy Lett.* **2017**, *2*, 88–93.

33. Ghimire, S.; Chouhan, L.; Takano, Y.; Takahashi, K.; Nakamura, T.; Yuyama, K. I.; Biju, V. Amplified and Multicolor Emission from Films and Interfacial Layers of Lead Halide Perovskite Nanocrystals. *ACS Energy Lett.* **2019**, *4*, 133–141.

34. Zhang, Y.; Meng, Q. S.; Zhang, L.; Luo, Y.; Yu, Y. J.; Yang, B.; Zhang, Y.; Esteban,

R.; Aizpurua, J.; Luo, Y.; Yang, J. L.; Dong, Z. C.; Hou, J. G. Sub-Nanometer Control of the Coherent Interaction between a Single-Molecule and a Plasmonic Nanocavity. *Nat. Commun.* **2017**, *8*, 1–7.

35. Jain, P. K.; Huang, X.; El-Sayed, I. H.; El-Sayed, M. A. Noble Metals on the Nanoscale: Optical and Photothermal Properties and Some Applications in Imaging, Sensing, Biology, and Medicine. *Acc. Chem. Res.* **2008**, *41*, 1578–1586.

36. Lim, D. K.; Jeon, K. S.; Kim, H. M.; Nam, J. M.; Suh, Y. D. Nanogap-Engineerable Raman-Active Nanodumbbells for Single-Molecule Detection. *Nat. Mater.* **2010**, *9*, 60–67.

37. Neumann, B. T.; Johansson, M.; Kambhampati, D.; Knoll, W. Surface ± Plasmon Fluorescence Spectroscopy. **2002**, *31658*, 575–586.

38. Kulakovich, O.; Strekal, N.; Yaroshevich, A.; Maskevich, S.; Gaponenko, S.; Nabiev, I.; Woggon, U.; Artemyev, M. Enhanced Luminescence of CdSe Quantum Dots on Gold Colloids. *Nano Lett.* **2002**, *2*, 1449–1452.

General conclusions

In this thesis, I studied the exciton, charge carrier, interfacial electron-transfer, and surface plasmon-coupled exciton recombination dynamics in perovskite nanocrystals in films or plasmonic Au NP substrates. The extent of carrier diffusion and the degree of radiative losses were realized in closely packed nanocrystal films, which weakens the quantum confinement due to increased dielectric screening and enables the dissociation of early excitons into free carriers and their migration. The weak confinement and long-range carrier migration increased the PL lifetime of films and enabled me to design donor-acceptor interfaces and capture photogenerated electrons at long distances. Also, the direct synthesis of ligand-free nanocrystals on Au NP films enabled me to realize exciton-plasmon coupled PL intensity enhancement through Au-Br interactions for $MAPbBr_3$ nanocrystals. This research emphasizes the significance of interfacial electron transfer and plasmon-assisted emission intensity enhancement in perovskite nanocrystals-based heterostructures to next-generation photovoltaic and photonic devices.

To study the carrier migration and interfacial electron transfer in films, I synthesized $CsPbBr_3$ and $FAPbBr_3$ perovskite nanocrystals by the hot-injection and LARP methods, respectively, and their thin films were prepared by ligand-assisted assembly formation. Long-range carrier migration and photoinduced electron transfer were confirmed from PL lifetime and transient absorption studies. I prepared interfacial electron donor-acceptor samples using perovskite nanocrystals and C_{60} or TiO_2. I understood the diffusion of photogenerated charge carriers from distance-dependent time-resolved PL experiments. In a donor-acceptor solution ($FAPbBr_3$-C_{60} or $CsPbBr_3$-C_{60}), the PL intensity, but not the PL lifetime of the perovskite donors, was quenched, revealing static electron transfer. Conversely, the distance-dependent electron transfer in films changed from dynamic to static from the perovskite-rich region to the donor-acceptor interface.

For understanding photoinduced electron transfer from perovskite nanocrystals at the single-particle level, I used $CsPbBr_3$ or $MAPbBr_3$ as the donor and TCNB or TCNQ as the acceptor. The feasibility of PET was predicted from the negative values of Gibbs's free energy change. The electron transfer rates were determined from time-resolved PL measurements. The acceptors quenched the PL intensity of the nanocrystals, accompanied by a decrease in the PL lifetimes in a solution, revealing a dynamic electron transfer. I demonstrated the heterogeneity of interfacial electron transfer from single-particle studies of the nanocrystals treated with TCNQ or TCNB, followed by analyzing the ON-time and OFF-time probability distributions.

Single-particle electron transfer was characterized by a decrease in the ON-time and an increase in the OFF-time.

To improve the radiative recombination rate of perovskite nanocrystals, I synthesized $MAPbBr_3$ nanocrystals with or without ligands on glass or an Au NP film. The perovskite nanocrystals without any ligand synthesized directly on Au NPs showed an enormous photoluminescence intensity enhancement. On the other hand, the PL intensities of nanocrystals with ligands were decreased. The difference, enhancement, or quenching of the intensity is discriminated based on LSPR-active chemical coupling of ligand-free $MAPbBr_3$ nanocrystals through the Au-Br interactions.

List of achievements

Publications

1. Long-Range Interfacial Charge Carrier Trapping in Halide Perovskite-C_{60} and Halide Perovskite-TiO_2 Donor-Acceptor Films
   Sachith, B. M.; Okamoto, T.; Ghimire, S.; Umeyama, T.; Takano, Y.; Imahori, H.; Biju, V.
   J. Phys. Chem. Lett. **2021**, *12*, 8644–8651. **(Featured on the cover)**

2. Mechano-optical Modulation of Excitons and Carrier Recombination in Self-Assembled Halide Perovskite Quantum Dots
   Zhang, Z.; Ghimire, S.; Okamoto, T.; **Sachith, B.M.**; Sobhanan, J.; Subrahmanyam, C.; Biju, V.
   ACS Nano, **2022,** *16*, 160-168. **(Featured on the cover)**

3. Simple Sonochemical Synthesis of $SrCuO_2$ Assisted GCN Nanocomposite for the Sensitive Electrochemical Detection of 4-AAP
   Sachith, B. M.; Sandeep, S.; Nandini, S.; Nalini, S.; Karthik, C. S.; Kumara Swamy, N.; Mallu, P.; Manjunath, J. G.
   Surfaces and Interfaces **2020**, *20*, 100603.

Patent

Mechano-optical modulation of exciton and charge carrier recombination in self-assembled halide perovskite quantum dots.
Japanese Patent Application Number P2021-125

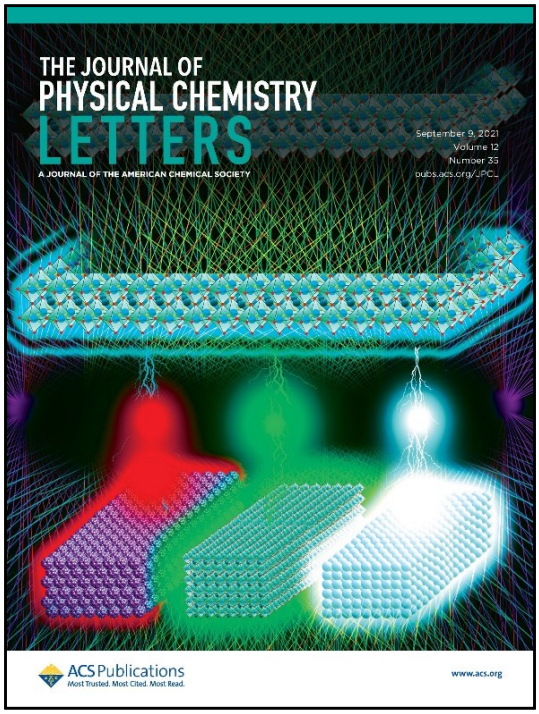

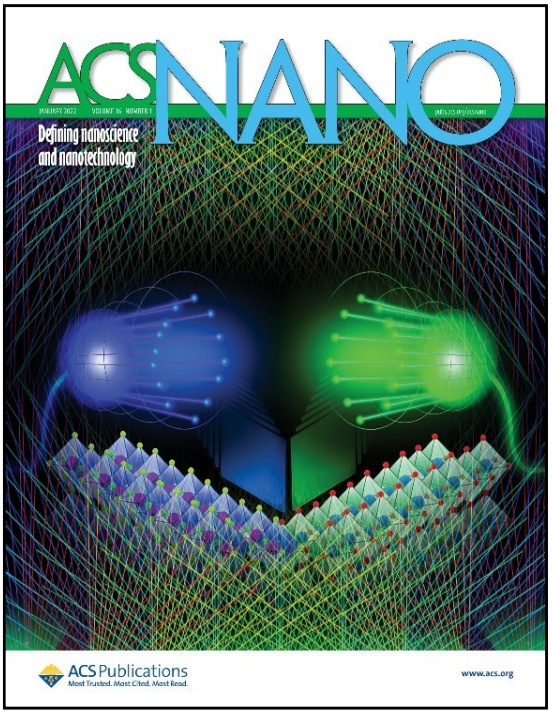

Oral Presentations

1. Transporting and Transferring Electrons Across Perovskite-Acceptor Interfaces
   Sachith, B.M.; Okamoto, T.; Ghimire, S.; Umeyama, T.; Takano, Y.; Imahori, H.; Biju, V.
   Annual Meeting of the Chemical Society of Japan, Online, Mar 24, 2022. (**Student presentation award**)

2. Long-Range Trapping of Photogenerated Electrons in Halide Perovskite Films
   Sachith, B.M.; Okamoto, T.; Ghimire, S.; Umeyama, T.; Takano, Y; Imahori, H.; Biju, V
   Annual Meeting of the Japanese Photochemistry Association, Online, Sep 14-16, 2021.

3. Interfacial Charge Carrier Trapping in Halide Perovskite- C_{60}/TiO_2 Donor-Acceptor Films
   Sachith, B.M.; Takano, Y; Biju, V.
   The 11th Asian photochemistry conference, South Korea, Online, from Nov 1-4, 2021.

4. Photoinduced Electron Transfer from Perovskite Films to Fullerene
   Sachith, B.M.; Takano, Y; Biju, V.
   The Chemical Society of Japan Hokkaido Branch 2021 Summer Research Presentation, Online, July 17, 2021.

5. Trapping Photogenerated Charge Carriers in Perovskite Nanocrystal Films by Doping with Electron Scavengers
   Sachith, B.M.; Takano, Y; Biju, V.
   Annual Meeting of the Chemical Society of Japan, Online, Mar 21, 2021.

6. Simple Sonochemical Synthesis of $SrCuO_2$ Assisted GCN Nanocomposite for the Sensitive Electrochemical Detection of 4-AAP
   Sachith, B.M.; Sandeep, S.
   The second National Conference on "Advanced Materials for Health, Energy, and Environment" (AMHEE), India, Sep 6-7, 2019. (**Best presentation award**)

Poster Presentations

7. Distance-Dependent Trapping of Photogenerated Charge Carriers in Perovskite Nanocrystal Films
   Sachith, B. M.; Takano, Y; Biju, V.
   The Chemical Society of Japan Hokkaido Branch 2021 Winter Research Presentation, Online, Jan 26, 2021.

8. Long-Range Trapping of Photogenerated Charge Carriers in Perovskite Nanocrystal Films
   Sachith, B. M.; Biju, V.
   The 22nd RIES-Hokudai International Symposium, Hokkaido university, Dec 6-7, 2021.

9. Electron Transfer from Perovskite Films Controlled by Controlling the Diffusion of Photogenerated Charge Carriers
   Sachith, B. M.; Ghimire, S.; Takano, Y; Biju, V.
   The 21st RIES- Hokudai International Symposium, Hokkaido University, Dec 10, 2020.

10. Long-Range Diffusion and Precise Confinement of Charge Carriers in Lead Halide Perovskite Nanocrystal Films
    Sachith, B. M.; Ghimire, S.; Biju, V.
    The 6th Hokkaido University Inter-Departmental Symposium, Hokkaido University, Oct 19, 2020.

11. Doping-Induced Carrier Dynamics in Lead Halide Perovskite Films
    Sachith, B. M.; Chouhan, L.; Biju, V.
    Annual Meeting of the Japanese Photochemistry Association, Online, Sep 9, 2020.

12. Novel Synthesis of Strontium Iron Oxide Nanoparticles and Its Application for the Detection of an Anti-Inflammatory Drug
    Sachith, B. M.; Sandeep, S.
    The International Workshop on Advanced Materials (IWAM), Ras Al Khaimah, United Arab Emirates, Feb 24-26, 2019.

13. Evaluation of the Coupling between Perovskite Exciton and Gold Plasmon in Films and Cavities.
    Sachith, B. M.; Biju, V.
    RIES-NCTU Joint International Symposium, Hokkaido university, Dec 2-3, 2019.